Summer 8-15-2019

Quantitatively Studying Tissue Damage in Multiple Sclerosis Using Gradient Recalled Echo MRI Sequences

Biao Xiang
Washington University in St. Louis

Recommended Citation

WASHINGTON UNIVERSITY IN ST. LOUIS

Department of Chemistry

Dissertation Examination Committee:
Joseph Ackerman, Chair
Dmitriy Yablonskiy, Co-Chair
Sophia Hayes
Dewey Holten
Alexander Sukstansky

Quantitatively Studying Tissue Damage in Multiple Sclerosis Using Gradient Recalled Echo MRI Sequences

by

Biao Xiang

A dissertation presented to
The Graduate School
of Washington University in
partial fulfillment of the
requirements for the degree
of Doctor of Philosophy

August 2019
St. Louis, Missouri

Table of Contents

List of Figures

List of Tables

Acknowledgement

First and foremost I want to thank my advisors Dr. Dmitriy Yablonskiy and Dr. Joseph Ackerman. Over the past several years, Dr. Yablonskiy patiently taught me how MRI works and guided me through numerous setbacks in the research projects. All the work presented in this thesis was under his support and encouragement. I really appreciate his help, time, ideas, and funding which make my PhD experience productive and stimulating. I'm also very grateful to Dr. Ackerman for introducing me to BMRL and providing generous support in my academic career.

I would also like to thank my thesis committee members, Dr. Dewey Holten, Dr. Sophia Hayes and Dr. Alexander Sukstansky for their helpful suggestions and insightful comments.

Special thanks to Dr. Anne Cross, for leading me to the field of Multiple Sclerosis (MS). Her expertise in MS was essential for the success of my study. She taught me to how to think from a clinician's perspective. I really appreciate her time, advice, encouragement and patience in the past several years. It was a really rewarding experience to work with her, and she is a role model for me in many ways.

Thank you to Dr. Jie Wen, whom I learned a lot from since I joined the lab. Whenever I encountered problems in research, you always helped me out patiently. Thank you to Dr. Yue Zhao, who is great labmate and roommate. He provided me generous help in research and life for more than four years.

Many people have helped and taught me immensely at BMRL. I give my heartfelt thanks to Dr. Tsen-Hsuan Lin, Dr. James Quirk, Dr. Larry Bretthorst, Dr. Victor Song, Dr. Peng Sun, Dr. Satya Kothapalli, who provided generous help and advice during my years in BMRL. Also thanks to Mr.

Abstract

Multiple Sclerosis (MS) is an unpredictable, often disabling disease of the central nervous system (CNS) that disrupts the flow of information within the brain, and between the brain the body. MS is the most common progressive neurologic disease of young adults, affecting approximately 2.3 million people worldwide. It is estimated that more than 700,000 individuals are affected by MS in United States. While MS has been studied for decades, the cause of it is still not definite and a fully effective treatment for MS is not yet available.

Magnetic resonance imaging (MRI) has been used extensively in MS diagnosis and for monitoring disease. Clinical T1W, T2W and Fluid Attenuated Inversion Recovery (FLAIR) images are able to detect focal WM lesions with high accuracy and are used in MS diagnosis. However, standard clinical MRI lacks specificity to MS pathology and correlates only modestly with MS disability. Many studies have been devoted to the development and experimental validation of quantitative methods sensitive to myelin damage (hallmark of MS), primarily by means of multiexponential *T2* imaging of water trapped between myelin layers, magnetization transfer (MT) and diffusion tensor imaging. These techniques have not gained traction in clinical practice, prompting searches for novel, more pathologically specific and efficient approaches. In this thesis, two novel MRI techniques developed in our lab, quantitative Gradient Recalled Echo (qGRE) and Multi-Angular-Relaxometry of Tissue (SMART), were used to quantitatively study MS tissue damage.

Our qGRE technique (which is an advanced version of GEPCI – gradient echo plural contrast imaging) is based on quantitative measurements of the transverse relaxation properties of the Gradient Recalled Echo (GRE) MRI signal. This quantitative qGRE approach allows estimation of tissue damage in MS lesions and normal appearing WM and GM. An innovative qGRE method of data analysis allows separation of tissue-cellular-specific ($R2t^*$ relaxation rate constant) from

Blood Oxygen Level Dependent (BOLD) contributions to the total GRE MRI signal decay rate constant ($R2^*$). Since BOLD effect causes variations in MRI signal that occur with physiological state-dependent changes in blood flow and/or oxygen consumption, the $R2t^*$ values more specifically reflect the tissue-cellular component of $R2^*$. The tissue-cellular-specific ($R2t^*$) MRI relaxation parameter depends on the environment of water molecules (the main source of MRI signal): higher concentrations of proteins, lipids, and other constituents of biological tissue and cellular constituents (sources of MRI signal relaxation) leading to higher relaxation rate constants. Our results showed that $R2t^*$ can sensitively detect MS-related pathology in cortical NAGM, subcortical NAWM and WM lesions. The method demonstrated tissue damage patterns in the CNS of the MS cohort. Our data shed light on the interrelationships of damage throughout the brain and cervical spinal cord, while supporting the idea of MS as a global CNS disease. In addition, our data demonstrated that while spinal cord CSA is a reliable marker for changes in motor functions, the reduction in the $R2t^*$ of GM and WM is a reliable indicator of cognitive dysfunction.

The SMART technique is also based on a GRE MRI sequence (but with multiple flip angles) and a model of GRE signal that accounts for cross-relaxation effects between "free" and "bound" water proton pools. Importantly, no MT pulses are used in SMART approach, thus overcoming high RF energy deposition associated with existing qMT approaches for evaluation of tissue macromolecular content. From a single protocol this technique can generate quantitative macromolecular proton fraction (MPF) images along with naturally co-registered quantitative images of longitudinal ($R1=1/T1$) and transverse ($R2^*=1/T2^*$) signal relaxation rate constants, and spin density. The SMART technique allows quantitative assessments of central nervous system (CNS) simultaneously using several tissue contrasts. Our results showed that the SMART metrics can distinguish progressive MS from relapsing-remitting MS (RRMS) and correlate with clinical

assessments. Without applying either MT or 180° radiofrequency pulses, SMART MRI generates high resolution quantitative images with various contrasts, and is safe for high-field MRI, making it a useful outcome measure in clinical trials.

Chapter 1: Introduction

1.1 Nuclear Magnetic Resonance Imaging

Nuclear magnetic resonance imaging, or magnetic resonance imaging (MRI), is a noninvasive medical imaging modality widely used to form images of the anatomy, pathology and physiological process of the body. MRI relies on the spinning motion of magnetic resonance active nuclei. Given the large magnetic moment of ^{1}H nuclei and its abundance inside the body, clinical MRI techniques focus on the hydrogen nucleus. Classical MRI textbooks have a more comprehensive description of this section [1, 2].

1.1.1 Nuclear spins

In quantum mechanics, spin is an intrinsic property of atomic and subatomic particles. In nuclei that have an even mass number (with equal numbers of neutrons and protons), such as ^{12}C and ^{16}O, half spin is in one direction and half in the opposite direction, resulting in no net spins. For nuclei with odd mass numbers, such as ^{1}H and ^{13}C, spin in each directions are not cancelling out, resulting in net spin or angular momentum. These nuclei are referred as magnetic resonance active nuclei.

The angular momentum S of any atomic or subatomic system is determined by spin quantum number s.

$$S = \frac{h}{4\pi} \sqrt{s(s+1)}\,, \tag{1.1}$$

where h represents the Planck's constant.

The angular momentum of S along any direction is defined as:

$$S_i = \frac{h}{2\pi} s_i, s_i \in \{-s, -s+1, ..., s-1, s\}\,, \tag{1.2}$$

Thus, a given particle has 2s+1 individual spin states in different directions.

Magnetic moment describes how a small magnetic dipole interacts with an external magnetic field:

$$E = -\vec{\mu} \bullet \vec{B_0}, \tag{1.3}$$

where E is the magnetic energy of a particle, and B_0 is external magnetic field. μ is the intrinsic magnetic moment, which is defined as the product of the gyromagnetic ratio γ the spin angular momentum S.

The spin quantum number of a proton is 1/2. This means a proton has two possible spin states: 1/2 (spin up) and -1/2 (spin down). In the absence of an external magnetic field, the magnetic moments of protons are randomly orientated. When placed in a static external magnetic field, there are only two spin states: parallel to the field and anti-parallel. The distribution of protons in these two states is determined by Boltzmann statistics as shown below:

$$\frac{Population(anti-parallel)}{Population(parallel)} = \exp(-\frac{\Delta E}{kT}) = \exp(-\frac{h\gamma B_0}{2\pi kT}), \tag{1.4}$$

where k is the Boltzmann constant and T is the absolute temperature. Note the population ratio is nearly 1, at physiologic temperature and a magnetic field of 3T. Only a small excess on the order of 1 in a million spins can be expected to be found in the lower energy state. Fortunately, the concentration of protons in the biological tissue is high (approximately 55 mol/L), providing a sufficient magnetic resonance signal.

For the convenience of describing signal generation process in MRI, nuclear spins are typically treated as the analogue of spins in classical physics. Notice that even the two energy states are

2

called parallel or anti-parallel, the magnetic moment of spins precesses around B_0 instead of completely aligning with B_0. The frequency of the precession is known as Larmor frequency:

$$\omega_0 = \gamma B_0.$$

(1.5)

B_0 is the strength of the magnetic field, and γ is the gyromagnetic ratio.
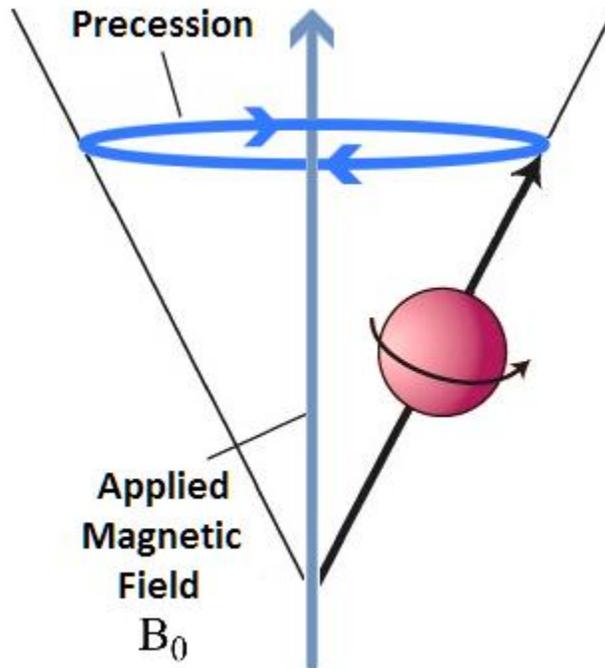
Figure 1.1 Illustration Of Spin Precession. Digital Image. *MyMS.org,*
(https://myms.org/mri_physics.htm)

1.1.2 Free induction decay

Under external magnetic field B_0, nuclear spins are polarized, resulting a net magnetization along

the B_0 (z direction). Upon applying an radio frequency (RF) pulse of energy at the Larmor

frequency of hydrogen, the net magnetization vector (NMV) moves out of alignment away from

B_0 and precesses in the transverse plane (x,y plane). According to Faraday's laws of induction, a

voltage will be induced in a conductive loop if the magnetic flux through the loop varies in time.

In MRI scanner, a receiver coil in the transverse plane is used to collect the current induced by the precessing magnetization. The current will be amplified and processed to generate magnetic resonance (MR) signal.

NMW will realign with B_0 by losing energy after the RF pulse is switched off. The process by which hydrogen nuclei lose energy gained from RF pulse is called relaxation.

Relaxation causes two independent process: recovery of magnetization in the longitudinal direction (*T1* recovery) and decay of magnetization in the transverse plane (*T2** decay). *T1* recovery is also termed as spin lattice relaxation since it is caused by hydrogen nuclei lose its absorbed energy from RF pulse to the surrounding environment or lattice. After the RF pulse is switched off, the NMW in longitudinal direction (M_z) changes as a function of time *(t)* in accord with the following equation:

$$M_z = M_0 \cdot (1 - \exp(-t/T_1)).$$ (1.6)

Meanwhile, the nuclear spins in the transverse plane will dephase due to magnetic field inhomogeneities, which is termed as *T2** relaxation. The magnetic field inhomogeneities can be divided into macroscopic (including imperfect B_0 and field distortion due to air/tissue interfaces), causing reversible (with respect to 180˚ RF pulse) part of transverse signal decay, and microscopic (molecular level) causing irreversible part of transverse relaxation which is characterized by a *T2* relaxation time constant. *T2* relaxation is also termed as spin-spin relaxation as it is caused by nuclei exchange energy with neighboring nuclei, precessing at slightly different frequencies due to microscopic inhomogeneous local magnetic field created by electron magnetic moment,

electron orbital current and nuclei themselves. After RF pulse is switched off, the NMW in

transverse plane (M_{xy}) decays as a function of time *(t)* in accord with the following equation:

$$M_{xy} = M_0 \cdot \exp(-t/T_2^*) \cdot \cos(\omega_0 \cdot t + \varphi_0). \qquad (1.7)$$

Where ω_0 is the Larmor frequency and φ_0 is the initial phase. The magnitude of induced

voltage/current in the receiver coil decreases as the magnitude of transverse magnetization

decreases. This induction of reduced MR signal is called free induction decay (FID) signal.
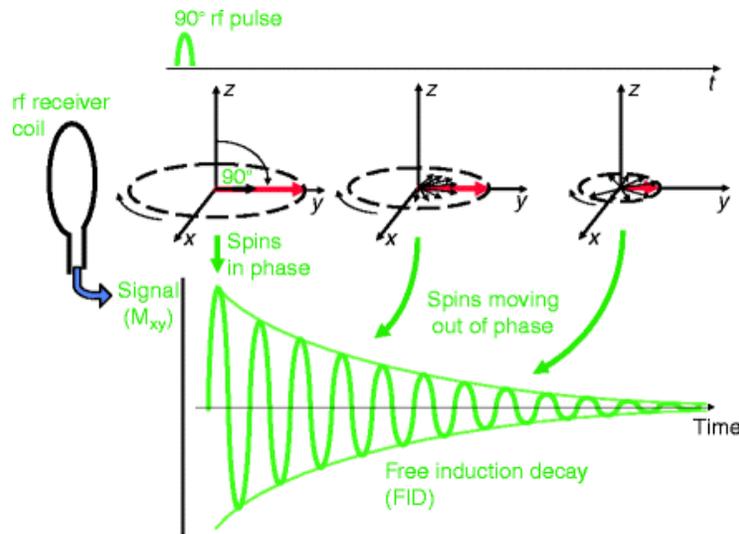
Figure 1.2 Illustration of Free Induction Decay, Digital image. *Generating a Signal: RF Pulses and Echoes*, 22 October 2010, https://link.springer.com/chapter/10.1007%2F978-1-84996-362-6_4.

1.1.3 Imaging Basics - Gradients and K-space

The FID signal measures the whole object without distinguishing spins at different locations,

which means FID signal could not be used to generate an image. To overcome this problem, a field

gradient was applied to create a magnetic field that depends linearly on location. For instance,

applying a gradient G_x in the x-direction in addition to a uniform magnetic field B_0 (also in x-direction), creates a spatially dependent field:

$$B = B_0 + G_x \cdot x. \tag{1.8}$$

Accordingly, the Larmor frequency also depends on the location:

$$\omega = \gamma B = \omega_0 + \gamma \cdot G_x \cdot x. \tag{1.9}$$

In this case, spins of the imaging object will have different resonance frequencies at different locations, which is often termed as frequency encoding. Frequency encoding provides the one-dimensional projection of the imaging object's spin density along the field gradient.
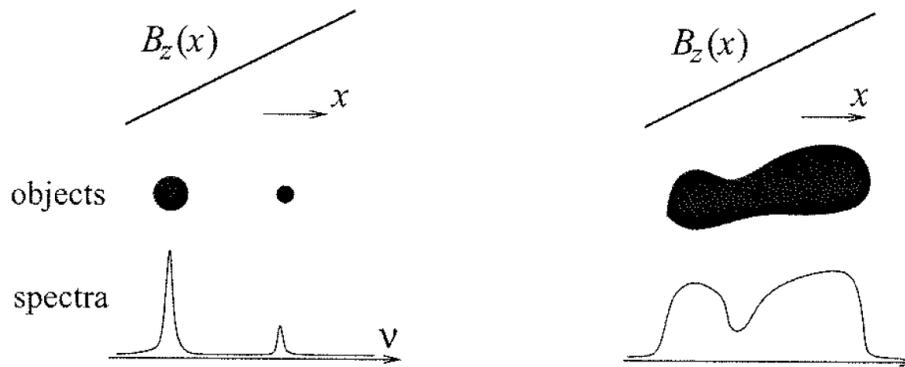
Figure 1.3 Illustration of frequency encoding.

For two-dimensional imaging, a phase encoding gradient G_y is applied in the orthogonal direction to the frequency encoding gradient. Phase encoding gradient is applied after the RF pulse and before the frequency encoding gradient for a short period (typically on the order of milliseconds). During this time period, spins will accumulate certain amount of phase, depending on the location

in the Y direction. To obtain images of a three-dimensional object, an additional phase encoding

gradient along Z direction is applied. The locations in the X direction are encoded by precession

frequencies. The locations in the Y, Z directions are encoded by the accumulated phase.

1.1.4 Gradient Recalled Echo (GRE) Sequence

Since most imaging techniques in my projects are based on gradient echo sequence, more details

are provided about this pulse sequence in this section. The following diagram shows a two-

dimensional version of gradient echo sequence.
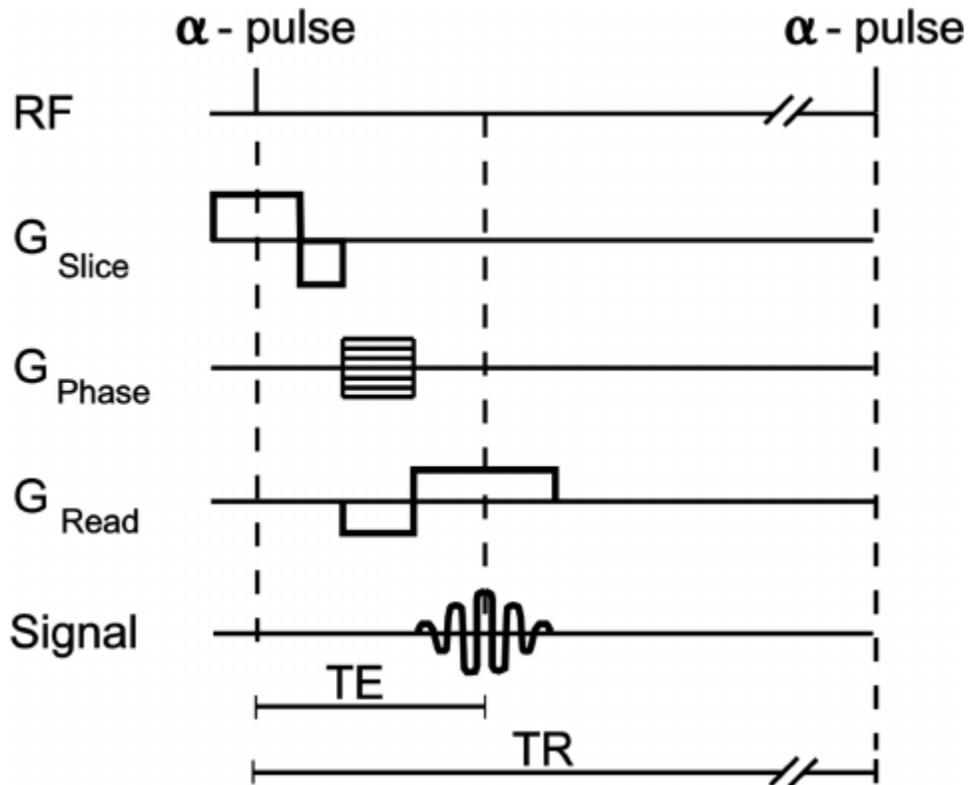
Figure 1.4 Pulse diagram of a gradient echo sequence. Digital image. *How We Perform Myocardial*

Perfusion WithCardiovascular Magnetic Resonance, May 2006,

https://www.researchgate.net/figure/Pulse-diagram-of-a-gradient-echo sequence_fig1_6442524

During gradient echo experiment, a frequency selective RF pulse is applied along with a slice selective gradient, exciting spins in a targeting slice. In order to refocus the dephasing of spins caused by the slice-select gradient, a rewinding gradient will be applied in the slice direction. Next, a single step of phase encoding gradient is applied over certain time duration, so that spins along phase encode direction will accumulate spatially dependent phase. A pre-rewind gradient will then be applied over exactly half of the read-out duration in the frequency encoding direction. The readout gradient will then be turned on to refocus the spins in readout direction at the time of echo (TE), which is time difference between Signal receivers will be turned on to collect data during the readout gradient. The data points collected during on readout gradient will fill a single k-space line.

The whole process will be repeated again with a different phase encoding gradient to fill another k-space line. The time delay between two excitation RF pulses is call time of repetition (TR). During one TR, one k-space line will be filled.

Images of the object can be generated by inverse Fourier Transform. The relationship between k-space, frequency domain, real space and time domain are showed in the following figure.
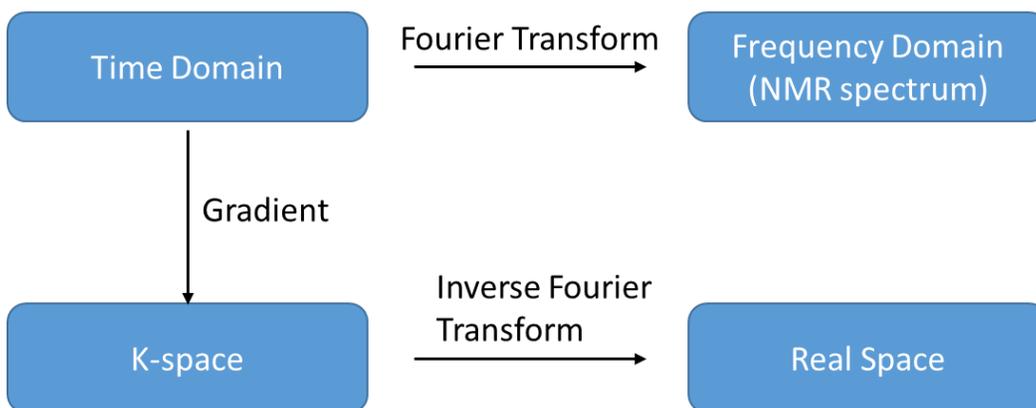
Figure 1.5 Relations between the time domain, frequency domain, k-space and real space.

1.2 Multiple Sclerosis

Multiple Sclerosis (MS) is an unpredictable, often disabling disease of the central nervous system (CNS) that disrupts the flow of information within the brain, and between the brain the body. MS is the most common progressive neurologic disease of young adults, affecting approximately 2.3 million people worldwide [3]. It is estimated that more than 700,000 individuals are affected by MS in United States [4]. While MS has been studied for decades, the cause of it is still not definite and a fully effective treatment for MS is yet available.

International Advisory Committee on Clinical Trials of MS in 2013 has defined four basic MS disease courses: clinically isolated syndrome, primary progressive, secondary progressive and relapsing remitting. Clinically isolated syndrome (CIS) is a first episode of neurologic symptoms caused by demyelination and inflammation in the CNS. By definition, the episode must last for at least 24 hours. In addition, the episode should be characteristic of MS but not yet meet the diagnostic criteria of MS. People who experience CIS may or may not eventually develop MS. Relapsing-remitting MS (RRMS), the most common disease course (85-90%), is defined as patients have relapses of MS and periods of stability in between relapses. Secondary progressive MS (SPMS) disease course starts with relapsing-remitting course and followed by a progressive worsening of neurologic function over time. SPMS evolves from over 50% of RRMS cases. Primary progressive MS (PPMS) is characterized as continues worsening of neurologic function from the onset of the MS symptoms. PPMS occurs in about 10% of MS patients.

The exact cause for MS has not been identified. MS is likely caused by a combination of genetic, environmental, infectious factors and vascular problems [5, 6]. MS presents a rather complex pathology. Currently, it is thought to be autoimmune [7]. Inflammatory cells from the bloodstream cross the blood-brain barrier to enter the CNS [7], leading to damage to myelin and axons, which results in symptoms and signs. People with MS (pwMS) present a wide spectrum of symptoms, including fatigue, difficulty moving, problems in speech or swallowing, visual problems, and bladder and bowel dysfunctions. MS can also cause cognitive impairment such as depression and unstable mood.

Multiple Sclerosis Functional Composite (MSFC) is a standardized, quantitative assessment instrument to measure MS symptom severity [8]. MSFC includes the Expanded Disability Status Scale (EDSS) standardized neurological examination, 25-foot timed walk (25FTW) assessment of gait, nine-hole peg test (9HPT) assessments of bilateral upper extremity function, paced auditory serial addition test (PASAT) and symbol digit modalities test (SDMT) assessments of cognitive function.

Lacking a clinical, laboratory, or imaging biomarker that reliably differentiate MS from other neurological conditions, conditions such as migraine, fibromyalgia and functional neurologic disorders are often misdiagnosed as MS [9-11]. Misdiagnosis of MS bears serious implications: the MS disease-modifying therapies may impose high risks on patients, treating physicians may face medicolegal claims and litigation and health care system will carry the financial burden from the unnecessary disease-modifying therapy [9]. To avoid the negative misdiagnosis outcomes, scientific researchers and clinicians must continue to search for new robust biomarkers for MS diagnosis.

1.3 Magnetic Resonance Imaging in MS

Magnetic resonance imaging (MRI) has been used extensively in MS diagnosis and for monitoring disease. Clinical T1W, T2W and Fluid Attenuated Inversion Recovery (FLAIR) images are able to detect focal WM lesions with high accuracy and are used in MS diagnosis [12, 13].
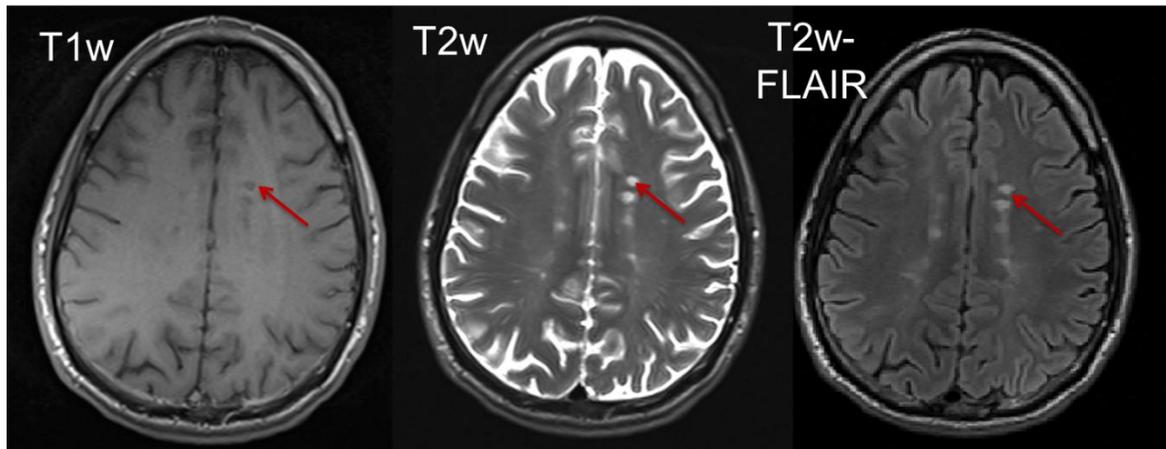
Figure 1.6 Examples of T1-weighted image, T2-weighted image and FLAIR image of a MS patient. MS lesion showed hypointense signals on the T1w image and hyperintense signals on the T2-weighted and FLAIR images.

In T1W images, cerebral spinal fluid (CSF) appears dark, white matter (WM) appears bright, and grey matter (GM) in between them. MS lesions have hypointense signals on T1W images and are often called "black holes." T2W images, WM appears dark, CSF appears bright, and GM in between them. MS lesions are always brighter than WM. In T2W images, both MS lesions and CSF are bright, making lesion detect more difficult. To solve this problem, CSF signals are suppressed in FLAIR images, making MS lesions readily detectable. FLAIR is frequently used to scan MS patients in clinical practice.

With the gadolinium (Gd) based contrasting agent, T1W images are also used to detect "active lesions." Since the contrasting agent will decrease T1 relaxation constant, the post-contrast T1W images will have hyperintense signal in blood vessels. In the area where blood-brain barrier (BBB) breaks down, Gd will diffuse into nearby tissue, generating hyperintense signals. The Gd-enhanced lesions are considered as "active lesions" since BBB breakdown allows immune cells to infiltrate the brain tissue, causing myelin and axon damage.

Lacking specificity to MS pathology [14], these widely used "conventional" MRI measurements, correlate only modestly with MS disability [15, 16]. Since myelin plays an important role in the pathologies of MS, many magnetic resonance studies aimed to measure myelin content in vivo. There are generally four main approaches for MR scientists to assess alterations in myelin content.

The first approach is to investigate myelin structures directly. The targets of this approach are the nonaqueous protons in the myelin lipids, such as the methylene group, or phosphorous atoms in the myelin structure itself. However, measuring the nonaqueous protons in myelin directly is challenging, since the MR signal from these protons decays in the order of a few tens of microseconds. In addition, signals from water will contaminate signals from nonaqueous protons in myelin. Nevertheless, several studies have succeeded in quantifying the signals from myelin. Using ultrashort echo time imaging, a few studies [17] were able to measure the ultrashort T2 component in neuro tissues. In particular, one study pointed out that the methylene group in myelin lipid is the sources for the ultrashort T2 signal [18]. In addition, ^{31}P spectroscopy was able to show information that can be derived about phospholipids in bilayer phospholipids, allowing us to assess the myelin integrity. The major shortcoming of this technique is the difficulty to quantify the signal from phosphatidylcholine head groups.

The other three approaches are to assess myelin content indirectly. The target of the second approach is the fraction of protons from water trapped between myelin layers (so called "myelin water"). Using multi-exponential T2 analysis of 32-echo spin-echo MRI data, MacKay et al. [19] quantified myelin water fraction (MWF) in MS patients in vivo. Subsequent histopathological studies showed that MWF correlated with myelin content [20, 21]. These studies have helped validate MWF as a biomarker to assess myelin content in neuronal tissues. The most often cited drawbacks of MWF imaging using spin-echo sequences are the single-slice imaging capability and long acquisition time [22]. To address these drawbacks, several other MRI techniques, such as gradient and spin-echo (GRASE) [23], T2 preparation [24], multigradient echo (MGRE) [25], multicomponent driven-equilibrium single-pulse observation of T1 and T2 (mcDESPOT) [26] and linear combination of myelin imaging [27], have been developed to study MWF. All of these newer techniques are able to acquire MRI data with multislice or whole brain coverage that are sensitive to MWF, within 30 minutes. Except for the mcDESPOT technique, most of the newer techniques to measure myelin water do not take the exchange of magnetization between water in different microanatomical compartments into consideration. This could undermine the claim that MWF is a quantitative measurement of myelin content. Detail review of Myelin Water Imaging is provided in a recent paper by Alonso-Ortiz et al [22].

The target of the third approach are the protons that are bound to macromolecules. Given the T2 of the bound protons is on the order of microseconds, the bound proton signal is not typically measured directly. Magnetization transfer (MT) imaging [28, 29] has been widely used to assess the bound protons. The majority of MT studies were based on the MT ratio (MTR) which measures the relative signal intensity decrease due to off-resonance radiofrequency saturation of protons bound to macromolecules. In MTR measurements, a two-pool model (free water and bound water)

has been commonly used. Since both relaxation within each proton pool and cross-relaxation between free water and bound water contribute to MTR, this technique still lacks pathologic specificity and does not have a large dynamic range of disease-related changes [30]. Unlike MTR, quantitative MT (qMT) experiments measure myelin bound pool fraction (BPF) [30-33], which offered improved specificity toward MS pathology. Several studies have shown that BPF correlates with myelin content [34, 35]. The limitations of qMT experiments generally include long acquisition time and high energy deposition (especially at magnetic fields 3T and higher). The need of quantitatively measuring MT effects safely and with high resolution prompts searching for novel MRI techniques.

The fourth approach to study myelin integrity is diffusion tensor imaging (DTI) [36]. DTI measures the rate and direction of movement of water molecules within tissues. In white matter, axonal tracts and myelin sheathes serve as physical barriers that impose directionality or anisotropy on water diffusion [37]. The fractional anisotropy (FA) and apparent diffusion coefficient (ADC) can be used to extract general information regarding organization of fiber tracts, but are unable to differentiate axon and myelin damage [37]. In a mouse model of retinal ischemia, Sun *et al.* [38] demonstrated that a decrease in axial diffusivity corresponding to axonal degeneration, which created barriers to longitudinal movement of water molecules. In addition, an increase in radial diffusivity corresponded to myelin loss, which facilitated water diffusion perpendicular to axons. Both interpretations were confirmed by histology [38]. In human studies, radial diffusivity was also shown as a promising biomarker of myelin status [39, 40]. Axial diffusivity seems to correlate with axonal degeneration in early stages of MS. With longer disease duration, increased axial diffusivity was observed [41]. In summary, radial and axial diffusivities are able to characterize pathological changes in axons and myelin structures, particularly in early and acute phase of MS.

Future work should improve axial diffusivity's capability to unravel the complex mechanism of axonal damage and repair.

Our laboratory developed two quantitative MRI techniques: Gradient Echo Plural Contrast Imaging (GEPCI) and Simultaneous Multi-Angular-Relaxometry of Tissue (SMART). These two MRI techniques, based on gradient recalled echo (GRE) sequences, allow quantitatively assess tissue damage in both normal-appearing tissues and MS lesions. The following chapters will explain these two MRI techniques in detail and evaluate their candidacy as biomarkers for MS.

1.4 Effects of Macromolecules on the Relaxation Times and Magnetization Transfer (MT)

The central nervous system has two types of tissue: white matter (WM) and grey matter (GM). GM contains the cell bodies, dendrites and axon terminals. WM is made of myelinated axon bundles, serving the function of transmitting signals. The T1 and T2 relaxation time constants are shorter in WM than in GM. In addition, WM has stronger macromolecular proton MT effect, compared with GM [42]. Macromolecular such as lipids and proteins are contributing factors to these differences. For instance, the lipid content in WM and GM are about 49-66% and 36-40%, respectively [43]. The higher lipid content level as well as higher concentration of certain lipids make the T1 and T2 relaxation in WM faster than in GM, and contribute to more pronounced MT effect in WM. The following two sections will discuss the relaxivity of protons in lipid, protein and carbohydrate solutions.

1.4.1 Relaxivity and MT of lipids

Using the multilamellar vesicle (MLV) suspensions model, Kucharczyk et al. systematically studied the effects of different major lipid components of white matter on relaxation times and MT [42]. In all cases, increased concentration of MLV caused a decrease in relaxation times and an increase in MT effect. Among phosphatidylcholine, galactocerebroside, cholesterol and sphingomyelin, galactocerebroside showed the strongest effect on relaxivity and MT. These effects are likely due to the large number of hydroxyl groups and the unique conformation of the hydrophilic head groups in galactocerebroside. Additionally, a decrease in pH caused an increase in MT an enhanced relaxation, suggesting that MT does not occur exclusively through spin exchange mechanism. Chemical exchange of labile protons also contributes to relaxivity and MT.

1.4.2 Relaxivity of protein and carbohydrate solutions

Like lipids, proteins can also contribute to MR signal relaxation. Using spin echo sequence, we measured the transverse signal decay rate constant R2 of aqueous bovine serum albumin (BSA) solution. In figure 1.7, R2 showed a strong linear dependence on the concentration of aqueous BSA solutions. The increased R2 at high protein concentration can be explained by intermolecular dipolar interaction between proteins and the water oriented on the protein surface, as well as intramolecular dipolar interaction between water trapped on the protein surface. Hills et al. demonstrated that transverse proton relaxation in BSA solutions can be explained by the fast chemical exchange between water and labile protein protons such as hydroxyl and amine protons[44]. The paper also claimed that the chemical exchange is the predominant mechanism for proton relaxation in BSA solutions.
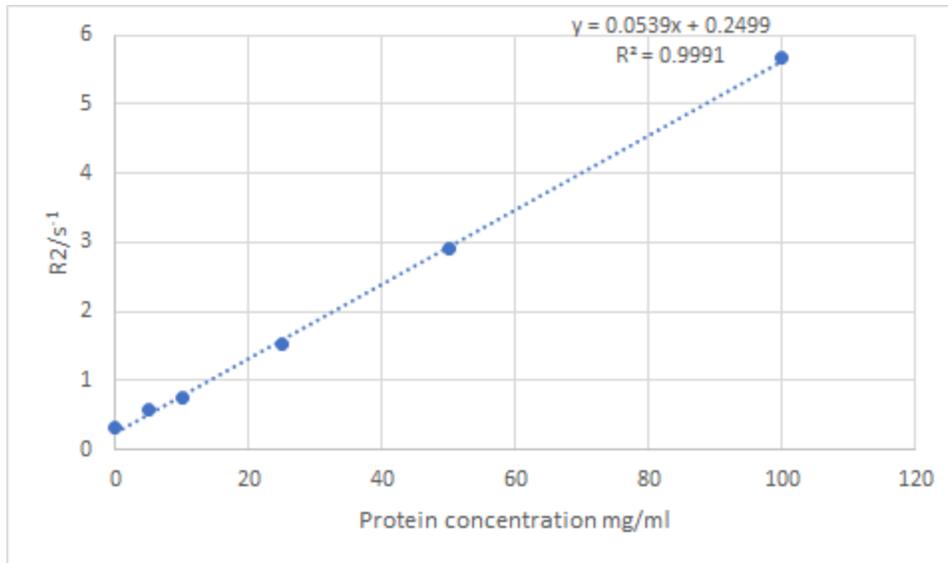
Figure 1.7. The transverse signal decay rate constant R2 at different protein concentrations. Data was collected on a Varian 500 MHz NMR instrument.

Similar to protein solutions, another study showed that transverse water proton relaxation is dominated by chemical exchange between water and hydroxyl groups of carbohydrate [45]. In addition to chemical exchange, diffusion coefficients, local magnetic field gradients and particle morphology all contribute to proton transverse relaxation behavior.

Chapter 2: Introduction to Gradient Echo Plural Contrast Imaging and Simultaneous Multi-Angular-Relaxometry of Tissue

2.1 Gradient Echo Plural Contrast Imaging (GEPCI)

The GEPCI technique is based on a 3-dimentional GRE sequence and a set of post-processing algorithms [46-51]. The output of GEPCI includes naturally co-registered images and quantitative maps with various contrasts reflecting biological tissue anatomic and microstructural properties.

2.1.1 Data acquisition

All the GEPCI data were acquired at a 3T Trio MRI scanner (Siemens, Erlangen, Germany). A 3-dimentional GRE sequence and a 32-channel phased-array head coil were used to obtain the data. Sequence parameters were: resolution $1\times1\times2$ mm^3 (readout, phase encoding, slab), FOV 256 mm$\times$192 mm, repetition time $TR = 50$ms, flip angle 30°, 10 gradient echoes started at $TE_1 = 4$ ms, echo spacing $\Delta TE = 4$ms. In order to correct the artifacts caused by physiological fluctuations [49], additional phase stabilization echo was collected for each line in k-space. The total acquisition time of the GEPCI protocol was 11 mins 30s.

2.1.2 Image construction by combining multi-channel data

The multi-channel GEPCI data was first transformed into the image domain using fast Fourier transform, and then combined using a previously developed algorithm [47]:

$$S_{comb}(TE_n) = \frac{1}{M} \cdot \sum_{m=1}^{M} \lambda_m \cdot \bar{S}_m(TE_1) \cdot S_m(TE_n);$$
(2.1)

where index n enumerates gradient echoes, M enumerates the total number of RF channels, m enumerates RF channels, $S_{comb}(TE_n)$ is a combined signal corresponding to echo time TE_n, $S_m(TE_n)$ represents signals from each individual channel corresponding to echo time TE_n. Parameter λ_m is defined as:

$$\lambda_m = \frac{\frac{1}{M} \sum_{m=1}^{M} \sigma_m^2}{\sigma_m^2}, \tag{2.2}$$

where σ_m represents the amplitude of noise in channel m, estimated by averaging the magnitude of 10X10 pixel area at the corner of images from each channel. Since the noise levels between different echo times are similar, they are averaged to obtain σ_m for each channel.

Since the GEPCI technique collects complex data, the following generalized algorithm is used for data combination:

$$S_{comb}(TE_n) = \frac{1}{M} \cdot \sum_{m=1}^{M} \lambda_m \cdot \bar{S}_m(TE_1) \cdot S_m(TE_n), \tag{2.3}$$

where $\bar{S}_m(TE_1)$ is the complex conjugate of the complex signal from channel m at TE_1. Since the signal phases of different channels have different initial values but the same frequency, this algorithm for combing signals from different channels allows for the optimal estimation of quantitative parameters [47, 52], and also removes the initial phase incoherence among the channels [47].

2.1.3 Correcting macroscopic magnetic field inhomogeneity with Voxel Spread Function (VSF)

One of the major advantages of gradient echo sequences is its efficiency. However, images generated from gradient echo sequences can be affected by macroscopic magnetic-field inhomogeneities. In order to overcome this problem, a voxel spread function has been developed [48].

A 1-dimension gradient echo experiment is used to explain how the VSF works. In the presence of a macroscopic magnetic-field inhomogeneity, the MRI signal can be described in the following equation:

$$\tilde{S}(k_x; TE) = \int \rho(x; TE) \cdot \exp[-2\pi i k_x x + i\gamma b(x)(TE + t) + i\varphi_0(x)] \cdot dx$$
$$2\pi k_x = \gamma G_x t_x \tag{2.4}$$

where $\rho(x;TE)$ is the "ideal" signal at the continuous location x in the absence of magnetic field inhomogeneities, TE represents echo time, x is the location of a voxel in the image domain, k_x is a voxel in k-space domain, G_x represents the read-out gradients, t_x is the duration of the read-out gradient and $\varphi_0(x)$ is the phase shift of the signal at time zero (mainly caused by RF field inhomogeneities). Notice here, the time is represented as $TE+t$, where t is the time during gradient echo acquisition ($t=0$ corresponds to the center of the gradient echo).

The previous equation has to be converted to a discrete equation to describe the signal in each voxel. Since the size of a voxel is way smaller than scale of the macroscopic magnetic field inhomogeneity, the distribution of $b(x)$ and $\varphi_0(x)$ in the mth voxel can be described in the following linear equations:

$$b_m(x) = b_m + g_{mx}x \quad ,$$
$$\varphi_0(x) = \varphi_{0,m} + \varphi_{mx}x \tag{2.5}$$

where b_m and $\varphi_{0,m}$ are constants within the mth voxel but vary over voxels, g_{mx} and φ_{mx} are the background gradient within the mth voxel. The "ideal" signal in the mth voxel $\sigma_m(TE)$ can be represented as a sum of $\rho(x;TE)$ across the volume (V) of the voxel.

$$\sigma_m(TE) = V \cdot < \rho(x;TE) >_m, \tag{2.6}$$

where $< \rho(x;TE) >_m$ is the averaged signal in the mth voxel. The signal is first integrated across x in a single voxel and then the integral is plugged into Equation (2.4):

$$\tilde{S}(k_x;TE) = \sum_m \sigma_m(TE) \cdot \exp(-2\pi i k_x x) \cdot \exp(+i\gamma b_m \cdot TE + i\varphi_{0,m}) \cdot \text{sinc}[(k_x - k_{mx})a_x]$$
$$2\pi k_{mx} = \gamma g_{mx} TE + \varphi_{mx} \tag{2.7}$$

Inverse Fourier transform is used to transform the data from k-space to the image domain. The expression for the signal at any voxel n with macroscopic magnetic field inhomogeneity

corrected is:

$$S_n(TE) = \frac{1}{N}\sum_m \{\sigma_m(TE)\cdot\exp(+i\gamma b_m TE + i\varphi_{0,m})\cdot\sum_j \mathrm{sinc}(k_{x,j}a_x - k_{mx}a_x)\cdot\exp[2\pi i k_{x,j}a_x(n-m)]\} \quad (2.8)$$

The overall signal in the *n*th voxel is related to all voxels in the image domain.

In order to simplify the calculation, we assume that the signals from neighboring voxels have similar behaviors in the absence of magnetic field inhomogeneity:

$$\sigma_m(TE) = \sigma_n(TE)\frac{|S_m(TE=0)|}{|S_n(TE=0)|}. \quad (2.9)$$

Equation (2.8) can then be reduced to:

$$S_n(TE) = \sigma_n(TE)\cdot F_n(TE)$$

$$F_n(TE) = \frac{1}{|S_n(0)|}\cdot\sum_m |S_m(0)|\cdot\exp(+i\gamma b_m TE + i\varphi_{0,m})\cdot\sum_j \mathrm{sinc}(k_{x,j}a_x - k_{mx}a_x)\cdot\exp[2\pi i k_{x,j}a_x(n-m)]$$

$$,(2.10)$$

where $F_n(TE)$ represents the VSF that accounts for the influence of magnetic field inhomogeneities. The one-dimensional VSF can also be applied into 2-dimensional and 3-dimensional situations.

The following figure demonstrates that the VSF approach can significantly reduce the artifacts on *R2** maps especially at the air/water interface.
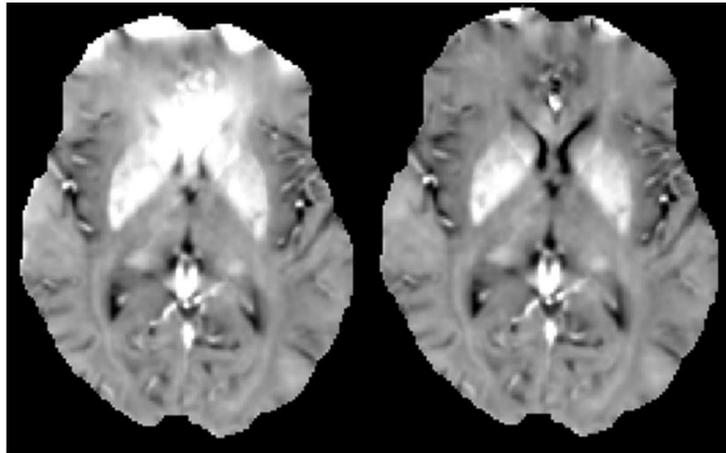
Figure 2.1. *R2** map without VSF correction (left) and with VSF correction (right) from a healthy subject (obtained in our laboratory). At air/water interface (nasal area), magnetic field

inhomogeneity contributed to bright artifacts that covered the underlying structures. After applying the VSF, the artifact at the nasal area was successfully corrected.

2.1.4 Basic GEPCI images

The major outputs of GEPCI technique are *R2* (1/T2*)* map, frequency map and *T1*-weighted images. They are determined by analyzing the combined data voxel-by-voxel using the following model:

$$S(TE) = A_0 \cdot \exp\left(-R2^* \cdot (TE + TE_1) + i \cdot 2\pi \cdot \Delta f \cdot (TE - TE_1)\right) \cdot F(TE), \tag{2.11}$$

where A_0 is the *T1*-weighted image, *TE* is the gradient echo time, Δf is the frequency shift (depends on both tissue structure and macroscopic magnetic field inhomogeneities), *F(TE)* represents the VSF which corrects the influence of macroscopic magnetic field inhomogeneities [48], and *R2** is the transverse signal decay rate constant. Examples of *T1*-weighted and *R2** images are shown in the following figure.
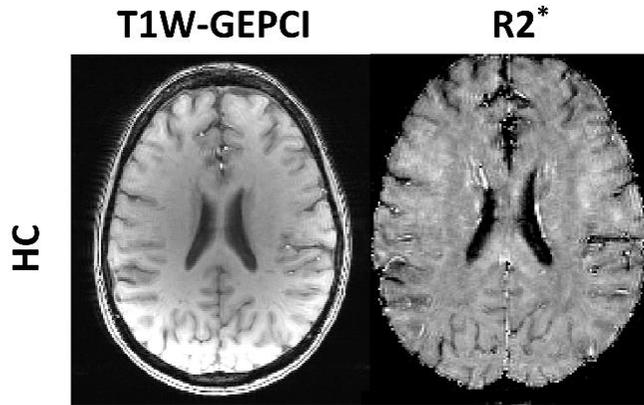
Figure 2.2. Examples of axial GEPCI T1-weighted and *R2** maps from a healthy subject.

Derived contrast images such as fluid suppressed *T2** images and susceptibility weighted image (SWI) like images, can also be constructed using the equations listed in [51]. Since these derived contrast images are not used in my studies, they are not discussed in detail here.

2.2 Quantitative Blood-oxygen-level dependent (qBOLD) imaging
2.2.1 Blood-oxygen-level dependent (BOLD) effect

After removing the macroscopic magnetic field inhomogeneity, the $R2^*$ determined from equation [2.11] provides quantitative assessment of tissue microstructural properties. However, this $R2^*$ is still subject to the influences of other susceptibility effects, which might be able to provide information about the tissue on the cellular level. One of the essential susceptibility effects on MRI signals is the blood-oxygen-level dependent (BOLD) discovered by Ogawa [53]. Hemoglobin (Hb or Hgb) is an oxygen-transporting protein containing iron (Fe). When oxygen is bound to hemoglobin, the protein complex is diamagnetic with susceptibility at -9 ppm, similar to the susceptibility of water in tissues. After releasing oxygen to support cellular metabolic processes, the protein complex becomes paramagnetic, which a susceptibility at 0.15 ppm.The difference between magnetic susceptibility of the two states of hemoglobin distorts the local magnetic field, contributing to additional signal decay.

Since BOLD effect causes variations in MRI signal that occur with physiological state-dependent changes in blood flow and/or oxygen consumption, a method that allows separation of tissue-cellular-specific ($R2t^*$ relaxation rate constant) from BOLD contributions to total GRE MRI signal decay rate constant ($R2^*$) is needed. In order to solve this problem, a quantitative MRI-based approach has been developed [54]. This approach was originally used to describe NMR signal behavior with the in magnetically inhomogeneous tissues. This approach suggests that the signal decays exponentially and the relaxation rate depends nonlinearly on echo time when echo time is shorter than a characteristic time t_c. When the echo is longer than t_c, the signal follows a simple exponential decay and the relaxation rate constant does not depend on the echo time. These signal behaviors allow the separation of BOLD effect from total signal decay rate constant $R2^*$.

Several subsequent studies have been published to support this approach by performing phantom studies [55], measuring blood magnetic susceptibility [56], testing in an animal model [57], analyzing systematic errors due to diffusion effects [58] and errors due to noise in the data [59, 60]

2.2.2 qBOLD model for the blood vessel network

Two assumptions have been made to describe the signal behavior in the presence of BOLD effect. The first assumption is that water diffusion can be ignored and the second is that blood vessels are a set of cylinders with infinite length and randomly distributed radiuses.

The GRE signal decay due to the presence of blood vessel network with deoxygenated blood [54] can be described as:

$$F_{BOLD}(TE) = \exp[-\zeta \cdot f_s(\delta\omega \cdot TE)].$$

(2.12)

In practice, we use a recently proposed a new expression [50]:

$$F_{BOLD}(TE) = 1 - \frac{\zeta}{1-\zeta} \cdot f_s(\delta\omega \cdot TE) + \frac{1}{1-\zeta} \cdot f_s(\zeta \cdot \delta\omega \cdot TE),$$

(2.13)

that better accounts for the presence of large vessels in the voxel than the traditional exponential function [54]. ζ represents the deoxygenated cerebral blood volume fraction (dCBV) and $\delta\omega$ is the characteristic frequency determined by the susceptibility difference between deoxygenated blood and surrounding tissue[54]:

$$\delta\omega = \frac{4}{3}\pi \cdot \gamma \cdot B_0 \cdot Hct \cdot \Delta\chi_0 \cdot (1-Y)$$

(2.14)

where Y is the blood oxygenation level (with Y=0 being fully deoxygenated), Hct is the blood hematocrit, γ is the gyromagnetic ratio, $\Delta x_0 = 0.27\,ppm$ [56] which is the susceptibility difference between oxygen saturated and fully deoxygenated blood. Function f_s describes the signal decay caused by the blood vessel network which was defined in [54]. Herein we use a mathematical expression for function f_s in terms of a generalized hypergeometric function $_1F_2$ [61]:

$$f_s(\delta\omega \cdot TE) = {}_1F_2\left(\left[-\frac{1}{2}\right]; \left[\frac{3}{4}, \frac{5}{4}\right]; -\frac{9}{16}(\delta\omega \cdot TE)^2\right) - 1$$

(2.15)

The function is nonlinear when $\delta\omega \cdot TE \leq 1$. However, when $\delta\omega \cdot TE \gg 1$, the function is linear, which is shown in the following figure:
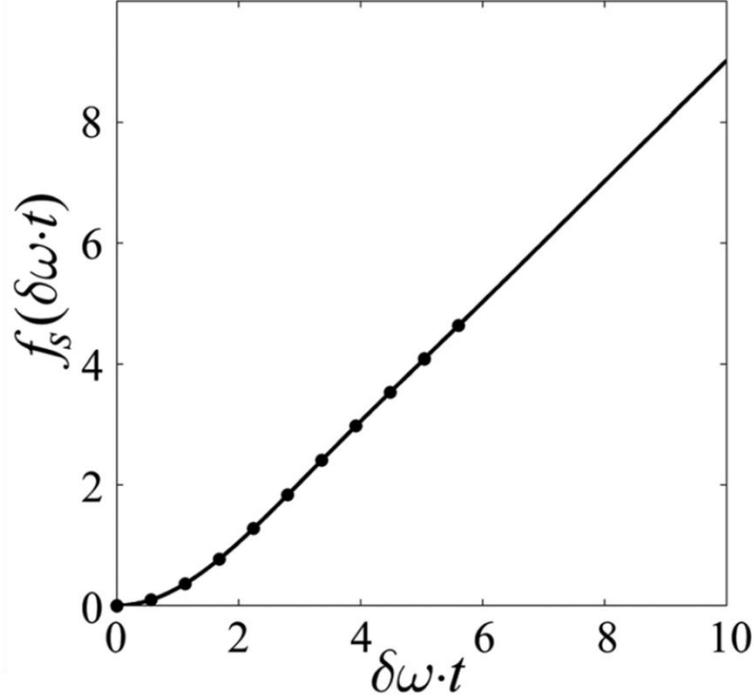
Figure 2.3 Function f_s versus $\delta\omega \cdot TE$. The dots are values at our echoes ($t = TE_n$) assuming Y=60%.

2.2.3 Summary

In summary, the following model was used to describe signal decay in GRE sequence:

$$S(TE) = A_0 \cdot \exp\left[-R2t^* \cdot (TE + TE_1) + i \cdot 2\pi \cdot \Delta f \cdot (TE - TE_1)\right] \cdot F_{BOLD}(TE) \cdot F(TE) \ , \qquad (2.16)$$

where *TE* is the gradient echo time, *R2t** (*1/T2t**) is the tissue-cellular-specific transverse relaxation rate constant (describing GRE signal decay in the absence of BOLD effect), Δf is the frequency shift (depends on tissue structure and macroscopic magnetic field inhomogeneities), $F_{BOLD}(TE)$ describes GRE signal decay due to the presence of blood vessel network with deoxygenated blood (veins and the part of capillaries adjacent to veins), and *F(TE)* represents VSF that describes signal decay due to macroscopic magnetic field inhomogeneities.

By fitting the equation to the real and imaginary parts of the complex signal using nonlinear regression algorithm, we are able to find the six parameters: *A₀*, *R2t** and Δf for each voxel in the brain.

Examples of *T1*-weighted and *R2t** images are shown in the following figure.
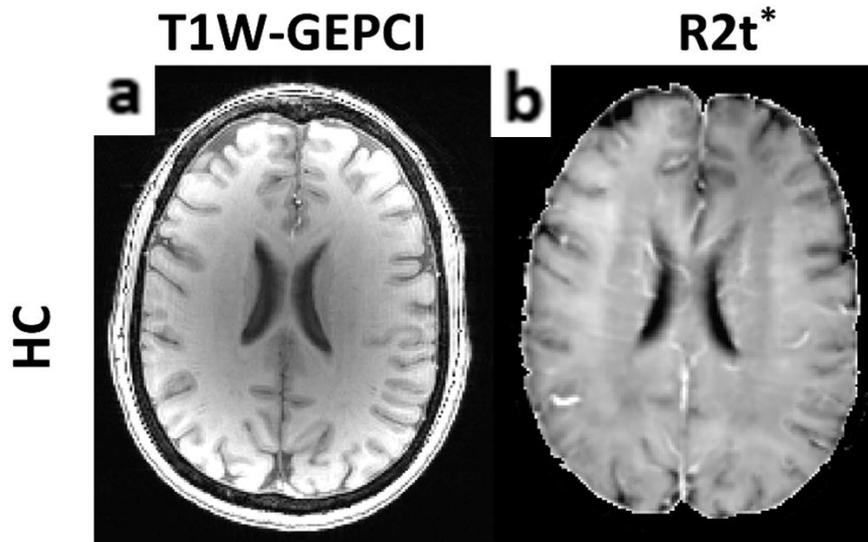
Figure 2.4. Examples of axial GEPCI *T1*-weighted (a) and *R2t** (b) maps from a healthy subject.

2.3 Simultaneous Multi-Angular-Relaxometry of Tissue

Simultaneous Multi-Angular-Relaxometry of Tissue (SMART) is a novel quantitative MRI technique based on a gradient recalled echo MRI sequenc with multiple flip angles and multiple gradient echoes [62]. The theory of SMART technique takes into consideration cross-relaxation between "free" and "bound" protons to macromolecules, generating co-registered macromolecular proton fraction (MPF) map, longitudinal and transverse relaxation rate constant maps and proton density map.

2.3.1 Background

Myelin is the multi-layer protective coating around axons in the central nervous system. Since myelin damage is the pathological hallmark of MS, many MRI techniques have been developed to measure myelin integrity. Due to the multi-layer structure, water in myelin has been divided into several components with different MR signal relaxation constants as showed in the following figure:
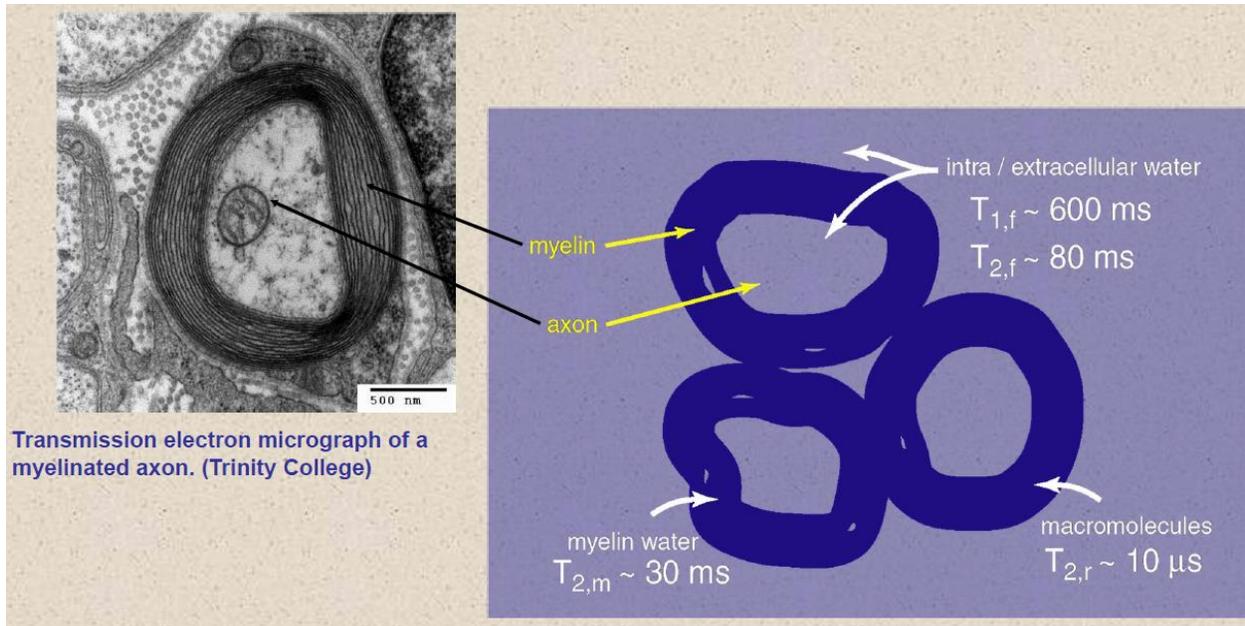
Figure 2.5 Structure of myelin and MR signal relaxation properties of water at different regions of myelin.

Magnetization transfer (MT) has been widely used to assess myelin content. In MT studies, a model of two cross-exchanging pools has been commonly used: a free pool, consisting of highly mobile protons associated with intracellular and extracellular water with long $T2$ (in the range 10 - 100 ms), and a bound pool, consisting of less mobile protons with an ultrashort $T2$ (less than 1ms) associated with macromolecules and membranes in biological tissues. Given its ultrashort $T2$, measuring signals from the bound pool is challenging. However, the exchange between the free pool and the bound pool allows indirect measurement of the bound pool using MT effects. Loss of myelin leads to decreased concentration of macromolecules and a consequent decrease of the bound pool.

Many MT studies have used the MT ratio (MTR) which measures the relative MRI signal intensity decrease in the presence of an off-resonance radiofrequency pulse causing saturation of the longitudinal magnetization of protons bound to macromolecules and consecutive transfer of this reduced magnetization to the free water. MTR depends on MRI pulse sequence parameters and is not quantitative. Unlike MTR, quantitative MT (qMT) experiments is independent of pulse sequence parameters. They measure the fraction of bound protons versus total protons in both free and bound pools. This fraction has been called the Macromolecule Proton Fraction (MPF) [30-33].

Although only protons that can dynamically exchange with protons in free water can participate in the MT process, qMT offers improved specificity for myelin content and several studies have shown that qMT-defined MPF correlates with myelin concentration [34, 35]. However, qMT is limited by long acquisition times, low resolution, and high RF energy deposition (especially at magnetic fields 3T and higher).

The SMART technique has been developed to address these limitations. Within 16 minutes, the SMART technique generates high resolution ($1x1x1$ mm^3) quantitative MPF images along with naturally co-registered quantitative images of longitudinal (*R1=1/T1*) and transverse (*R2*=1/T2**) signal relaxation rate constants images, and spin density image. Importantly, no MT pulse was used in the SMART protocol, making it safe in high-field MRI scanners.

2.3.2. MRI Data Acquisition
MRI data were collected using a 3T Trio MRI scanner (Siemens, Erlangen, Germany) equipped with a 32-channel phased-array head coil. SMART data of voxel size $1x1x1$ mm^3 were acquired using three dimensional multi-gradient-echo sequences with five flip angles α (5°, 10°, 20°, 40°, 60°) and three gradient echoes (echo times 2.3, 6.2, 10.1ms) for each α. GRAPPA algorithm (16) with an acceleration factor of two and 24 auto-calibrating lines in each phase encoding direction was used. The scan time for SMART data was 13 minutes 40 seconds (2 minutes 44 seconds per flip angle).

2.3.3. Phase-Sensitive *B1* Mapping
Measuring *B1* radiofrequency field accurately plays an important role in the SMART technique. Several methods have been proposed to measure *B1*, either based on the magnitude [63, 64] or phase [65, 66] of the MR signal.

In the SMART study, a phase-based *B1* mapping technique accounting for the effects of imperfect RF spoiling and magnetization relaxation was implemented [67]. The technique is based on a multi-gradient-echo sequence with two successive orthogonal RF excitation pulses followed by the train of gradient echoes measurements. More detailed explanation could be found at [67].

2.3.4. SMART Images
The multi-channel MRI data were combined using a previously published algorithm [51]. The combined data were then analyzed voxel-by-voxel using the SMART model, which generalized

the classical Ernst model by taking into account cross-relaxation effects between "free" and
"bound" (attached to macromolecules) water pools [62]:

$$S(\alpha,TR,TE) = S_0 \cdot \frac{1-\exp(-R1\cdot TR)-k_f^{'}\cdot TR\cdot\dfrac{\alpha^2}{\lambda\cdot(v\cdot\tau\cdot TR)+\alpha^2}}{1-\exp(-R1\cdot TR)\cdot\cos\alpha}\cdot\sin\alpha\cdot\exp(-R2^*\cdot TE)\cdot F(TE) \quad (2.17)$$

where

$$R1 = R1_f + k_f^{'}; \quad k_f^{'} = k_f\cdot(1+k_b/R1_b)^{-1}; \quad \lambda = R2_b\cdot(R1_b+k_b) \qquad (2.18)$$

In equations [2.17] and [2.18], S_0 is a spin density of free water; $F(TE)$ represents the part of the

signal decay due to the macroscopic field inhomogeneities (voxel spread function (VSF) approach

[48] used to account for these effects); subscripts "f" and "b" indicate "free" and "bound" water,

$R1$, $R2^*$ and k are longitudinal, transverse and cross-relaxation rate constants respectively; τ is the

RF pulse duration. The factor v depends on the RF pulse shape and is equal to one for rectangular

pulses used herein.

By fitting the theoretical model in Eq. [2.17] to experimental data on a voxel-by-voxel basis, the

five parameters S_0, $R1$, $k_f^{'}$, λ, and $R2^*$ were determined. The fraction of "bound" protons, MPF

[30, 32], was calculated from the equilibrium principle $k_f\cdot(1-MPF) = k_b\cdot MPF$:

$$MPF = k_f/(k_f+k_b) \qquad (2.19)$$

Using Eq. [2.18], MPF can then be expressed in terms of parameters available from [2.17] and

[2.18]:

$$MPF = \frac{k_f^{'}}{k_f^{'} + R1_b\cdot\left(1-(R1_b\cdot R2_b)/\lambda\right)} \qquad (2.20)$$

29

Since the ratio $\left(R1_b \cdot R2_b\right)/\lambda$ is much smaller than 1 [62], we used the following simplified equation for data analysis:

$$MPF = \frac{k_f^{'}}{R1_b + k_f^{'}} \qquad (2.21)$$

In Eq. [2.21] we fixed the parameter $R1_b$ to 1.84 s^{-1} in agreement with previous estimates [68].

2.3.5 Summary

In summary, without applying either MT or 180° radiofrequency pulses, the SMART technique can simultaneously generate high resolution quantitative images of MPF, $R1$ relaxation rate, $R2*$ relaxation rate and spin density and is safe for high-field MRI. SMART MRI would be a useful quantitative outcome measure in clinical trials.

Chapter 3: Single Scan Quantitative Gradient Recalled Echo MRI for Evaluation of Tissue Damage in Lesions and Normal Appearing Gray and White Matter in Multiple Sclerosis

3.1 Introduction:

Multiple sclerosis (MS) is an inflammatory disorder of the central nervous system (CNS) that involves the brain and the spinal cord, often causing neurologic disability. MRI plays an important role in MS diagnosis[69], as an endpoint in clinical trials[70], and as a means to monitor patients[71]. Recent MRI studies have focused on pathological changes in both macroscopic (visible with standard clinical MRI) lesions and normal appearing tissue (invisible with standard clinical MRI).

Conventional MRI techniques can readily detect focal white matter (WM) lesions. MS plaques are typically bright on *T2*-weighted (*T2W*) and FLAIR (fluid attenuated inversion recovery) images and dark on *T1*-weighted (*T1W*) images referred to as "gray" or "black holes" that are believed to represent the loss of underlying tissue, especially axons[72]. New approaches, such as phase-sensitive inversion-recovery (PSIR)[73], target MS lesions in gray matter (GM). A limitation of these images is that although they can be used to detect MS lesions, they cannot be used to quantify the severity of tissue destruction. Indeed if *T2W* or *T1W* images indicate that two MS lesions have identical volumes, this does not mean that the two lesions have the same underlying pathology. In

addition, neither normal-appearing white matter (NAWM), which is often abnormal histologically, nor normal-appearing GM (NAGM) can be identified on *T2W* or *T1W* images of MS subjects[74]. In addition to brain pathology, over 90% of MS patients develop spinal-cord lesions, and these cord lesions can greatly impact neurologic disability[75, 76].

Because of this, new approaches utilizing quantitative maps of *T2* and *T1* relaxation time constants, magnetization transfer ratio (MTR) and diffusion have been proposed[19, 77-80] in addition to standard subjective *T2*W and *T1W* images. However, for reasons such as long imaging times, low resolution and low signal-to-noise ratio (SNR), these are not commonly used for MS in clinical practice. Hence, fast, quantitative noninvasive imaging methods that reflect severity of MS pathology, both in lesions and normal appearing tissue, are needed for prognostication and to monitor patients[70, 81].

Our approach to this problem is based on quantitative measurements of the transverse relaxation properties of the Gradient Recalled Echo (GRE) MRI signal. This quantitative GRE (qGRE) approach[82], an advanced version of previously developed Gradient Echo Plural Contrast Imaging (GEPCI) technique[51], allows estimation of tissue damage in MS lesions and normal appearing WM and GM. An innovative qGRE method of data analysis[82] allows separation of tissue-cellular-specific (*R2t** relaxation rate constant) from Blood Oxygen Level Dependent (BOLD)[53] contributions to the total GRE MRI signal decay rate constant (*R2**). Since BOLD effect causes variations in MRI signal that occur with physiological state-dependent changes in blood flow and/or oxygen consumption, the *R2t** values more specifically reflect the tissue-cellular component of *R2**. The tissue-cellular-specific (*R2t**) MRI relaxation parameter depends on the environment of water molecules (the main source of MRI signal): higher concentrations of proteins,

lipids, and other constituents of biological tissue and cellular constituents (sources of MRI signal relaxation) leading to higher relaxation rate constants.

qGRE method that we use also includes acquisition and post-processing approaches that minimize adverse artifacts related to macroscopic magnetic field inhomogeneities[48] and physiological fluctuations[83]. From these perspectives, the transverse relaxation rate constant $R2t^*$ of the GRE signal is a close relative of the transverse relaxation rate $R2$ of the spin echo signal but qGRE approach allows much faster imaging with higher resolution and SNR. Prior studies in autopsied MS CNS tissue demonstrated statistically significant correlations between $T2$ ($1/R2$) relaxation time constants and MS pathology both for the spinal cord[84] and brain[21, 85]. Due to the similarity between $R2$ and $R2t^*$, we can conclude that $R2t^*$ measurements can serve as a pathological correlate of tissue damage in MS. Besides, measurements in autopsied samples also confirmed correlation with MS-related tissue damage in GM[86].

In this paper, we evaluate the novel MRI biomarker $R2t^*$ for quantitative detection of normal-appearing tissue damage in MS patients. We also investigate correlations between loss of tissue quality in different regions of central nervous system that could suggest the topographic signatures of tissue damage in MS patients.

3.2 Materials and methods:
3.2.1 Subjects
Forty-four MS patients with relapsing remitting (RRMS, n=15), secondary progressive (SPMS, n=16) and primary progressive (PPMS, n=13) MS clinical courses and 19 healthy control (HC) subjects were enrolled, after providing informed consent. HC were recruited to reflect the gender and age distribution of the MS patients. The study was approved by the Institutional Review Board.

3.2.2 Clinical testing

The Expanded Disability Status Scale (EDSS) standardized neurological examination, 25-foot timed walk (25FTW) assessment of gait, nine-hole peg test (9HPT) assessments of bilateral upper extremity function, and paced auditory serial addition test (PASAT) and symbol digit modalities test (SDMT) assessments of cognitive function were performed on the day of the MRI by examiners blinded to imaging results. For analyses, the 25FTW and 9HPT were converted to Z scores according to the following equations from Multiple Sclerosis Functional Composite (MSFC)[8]:

$$Z_{25FTW} = (25FTW - 9.5353)/11.4058 \tag{3.1}$$

$$Z_{9HPT} = (1/9HPT - 0.0439)/0.0101 \tag{3.2}$$

3.2.3 Image acquisition

MRI scans were performed on a 3.0 Tesla (3T) Trio MRI scanner (Siemens, Erlangen, Germany) using a 32-channel phased-array RF head coil. Previously developed GEPCI protocol[51] with navigation echo[83] was used to acquire a three dimensional (3D) multi-gradient-echo data with flip angle of 30°, *TR*=50 ms, voxel size of $1 \times 1 \times 2$ mm^3 and acquisition time of 11 min 30 s. For each phase encoding step, 10 gradient echoes and one navigation echo[83] were collected with first echo time *TE1* = 4 ms and echo spacing *ΔTE* = 4 ms. Standard clinical MPRAGE[87] images with voxel size: $1 \times 1 \times 1$ mm^3 were collected for segmentation purposes and measuring cortical thickness (TH) and spinal cord cross-sectional area (CSA). Fluid-attenuated inversion recovery (FLAIR) sequence with voxel size of $1 \times 1 \times 3$ mm^3 was used for outlining WM lesions.

3.2.4 Image processing and segmentation

The MRI data were analyzed using qGRE approach described in a previous study[82]. Details are presented in the supporting information. In brief, multi-channel data were combined using GEPCI

algorithm[51] and analyzed voxel-wise using the theoretical model of GRE signal relaxation[54, 88], and a set of post-processing algorithms that minimize adverse artifacts related to macroscopic magnetic field inhomogeneities[48] and physiological fluctuations[83]. This approach allows generation of images and quantitative maps with several contrasts reflecting biological tissue anatomic, microstructural and functional properties. In this study we use GEPCI *T1w* images and qGRE *R2t** maps. Importantly, all these images are inherently co-registered.

Brain GM and WM segmentation was performed on MPRAGE images using FreeSurfer 5.3.0 (Martinos Center for Biomedical Imaging, MGH/HST, US) with visual inspection of each segmented region of interest (ROI) for accuracy. It resulted in 68 cortical GM and 68 corresponding subcortical WM ROIs (for each ROI, the *R2t** and TH in left and right hemispheres were averaged). A list of ROIs is provided in the supporting information. MPRAGE images were co-registered with GEPCI-*T1w* images (which are intrinsically co-registered with qGRE *R2t** maps) using FSL 5.0.0 software (Analysis Group, FMRIB, Oxford, UK). This procedure also co-registered ROIs generated by FreeSurfer to GEPCI-T1w images and *R2** maps. To minimize partial volume effects, CSF masks were generated based on the GEPCI *T1w* images using FSL. Applying regional and CSF masks, median values of *R2t** and of cortical GM thickness were calculated for each cortical ROI. 3D MPRAGE data were processed using PropSeg (Spinal Cord Toolbox version 2.0)[89] to measure the spinal cord CSA. Mean CSA values at the four upper cervical levels were calculated.

3.2.5 Tissue Damage in MS Lesions based on *R2t**

For all subjects, MPRAGE and FLAIR images were registered using FSL and used to obtain WM lesion masks using "lesion-TOADS" tool[90] in Medical Image Processing, Analysis and Visualization (MIPAV)[91]. For each subject, tissue damage within WM MS lesions was

35

quantified in terms of tissue damage load (TDL) – parameter calculated based on the difference between R2t* values of voxel within the lesions and R2t* values of NAWM, similar to a previous R2*-based report[92] (details in the supporting information).

3.2.6 Statistical analysis

Statistical analyses and correlations were performed using MATLAB (The MathWorks, Inc.). Median *R2t** values were used to describe each FreeSurfer region in the brain, because *R2t** values in most regions were not normally distributed and also to minimize edge/partial volume effects and spurious values. Age is known to affect *R2t** and reduce cortical thickness[60], therefore, age-dependent *R2t** and cortical thickness values were obtained from the HC cohort of 19 individuals. To account for this effect, the median values of *R2t** in each of Free Surfer cortical or subcortical region (*n*) in the normal HC group were fitted by a linear equation:[60]

$$MedianValue_n = A_n + K_n \cdot (age - <age>)$$ (3.3)

where <age> is mean age of HC group. Introducing it in the equation, assigns to parameters A_n values corresponding to mean age of participants. This procedure allowed calculation of expected reference regional values for any actual patient age. Similar procedure was used for subcortical WM and FreeSurfer-defined cortical thickness. These calculated values were subtracted from the values of individual HC and MS subjects to generate *ΔR2t** and ΔThickness. Spinal cord area was not significantly correlated with age in our data (parameter *K* =0 in Eq. (3.3) and no significant difference of spinal cord area between male and female groups was found. Thus, the mean CSA value of the entire HC cohort was subtracted from each MS subject CSA values to generate ΔCSA. Due to the small number of male patients (Table 1) gender differences were not taken into account. For spinal cord, no significant correlation was found between spinal cord CSA and age, height, brain size and disease duration, so these variables were not considered in subsequent data analyses.

To explore topographic signatures of tissue damage in NAGM, Person's Correlation analysis was performed between $\Delta R2t^*$ of each cortical region (n) and $\Delta R2t^*$ of the mean global cerebral NAGM for all MS patients (without separation on MS sub-groups). Similar analysis was repeated for NAWM and cortical thickness.

To examine correlation between tissue damage in brain and spinal cord, Pearson's correlation analysis was performed between ΔCSA of C1 and $\Delta R2t^*$ of each cortical region, ΔCSA of C1 and $\Delta R2t^*$ of each subcortical WM region, and ΔCSA of C1 and thickness of each cortical region.

To establish relationships between MS-related tissue damage in adjacent subcortical WM and cortical GM regions, we applied linear regression analysis to the 44 MS patients using the following equation for each cortical region defined in FreeSurfer (n):

$$\frac{\Delta SubcorticalR2t_n^*}{\Delta MeanSubcorticalR2t^*} = q_n \cdot \frac{\Delta CorticalR2t_n^*}{\Delta MeanCorticalR2t^*} \tag{3.4}$$

where $MeanR2t^*$ is a mean $R2t^*$ measurement for the entire cortical GM or subcortical WM in each MS patient. Equations (3.4) were applied to establish MS-related tissue damage based on all 44 MS patients without regard to MS subtypes.

Correlations of ΔCSA with EDSS, 25FTW and 9HPT were assessed using Spearman's rank correlation since these data were not of Gaussian distribution. Parametric data were analyzed using Pearson's correlation. False discovery rate (FDR) with Benjamini-Hochberg procedure was used to correct for multiple testing. After correction, $p < 0.05$ was considered significant.

3.3 Results:
3.3.1 Examples of Images and Demographic Data of Participants

Examples of GEPCI *T1w* images, *R2t** maps, and MPRAGE images for one healthy control and

one MS patient are shown in Fig. 3.1.
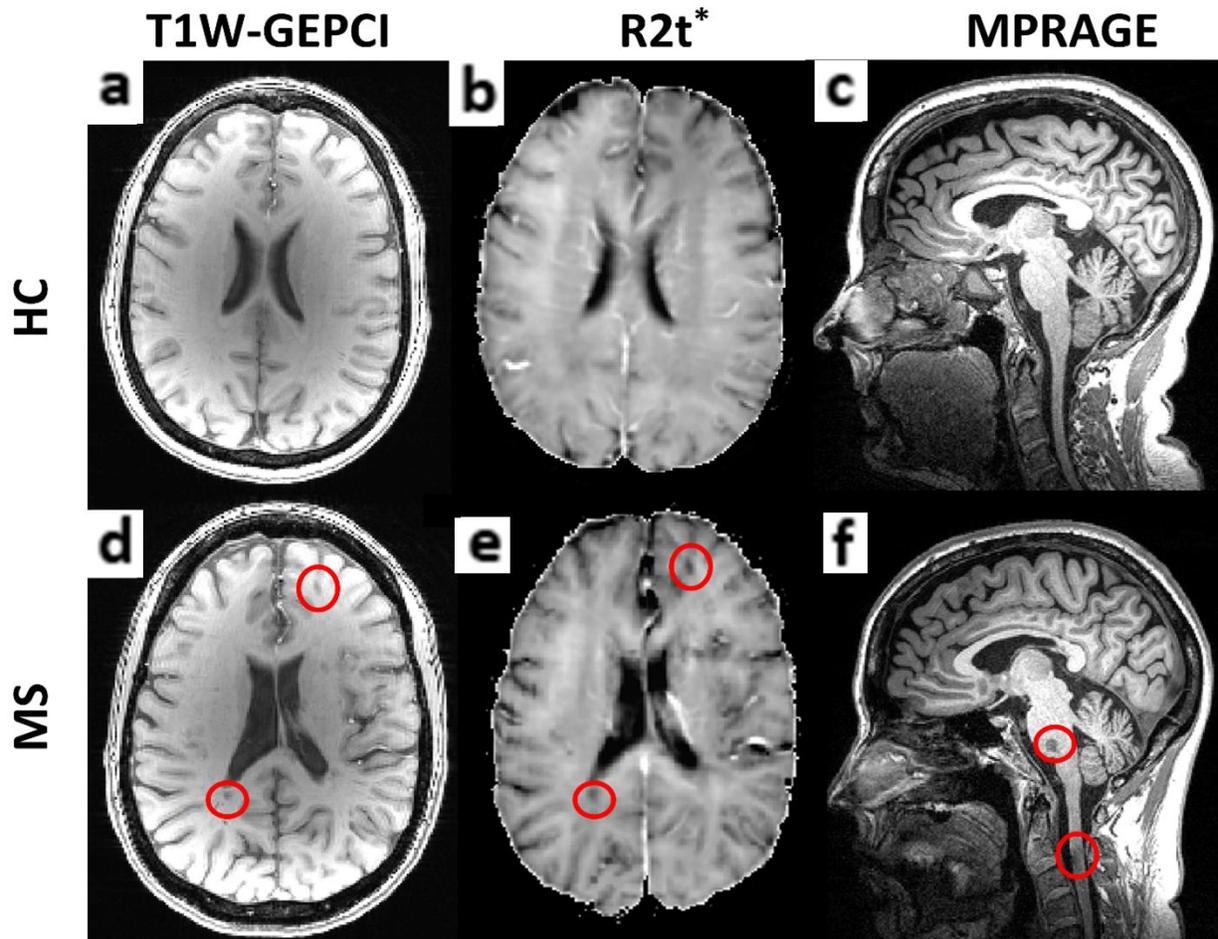
Figure 3.1 Examples of axial GEPCI T1 weighted images and R2t* maps are shown along with

sagittal MPRAGE images of one healthy control (a-c) and one MS patient (d-f). Images shown

come from similarly aged female (58 and 55 years old) HC and MS patient. In the MS patient, two

cerebral lesions, one pontine lesion and one spinal cord lesion at C2-3 level are outlined by red

circles.

The age range and gender ratio was similar for HC and MS patients (demographic and clinical information presented in Table 3.1). As expected, the mean EDSS was less severe for the RRMS patients than the progressive patients (Table 3.1).

Table 3.1 Summary of subject demographic and clinical information

		Healthy Control	MS		
			RRMS	**PPMS**	**SPMS**
Number		19	15	13	16
mean Age ± SD (years)		46.7+13.6 (23-76)	49.4±10.4 (32-60)	55.2±10.2 (37-74)	59.2±9.3 (45-75)
Female/Male		14/5	12/3	8/5	10/6
Disease duration (years)		n/a	15.8±7.7	15.8±9.6	21.1±10.0
EDSS mean ± SD (range)		n/a	2.6±1.3 (1-6)	5.7±1.1 (4.0-6.5)	5.6±1.5 (3.5-8)
25FTW mean ± SD (range)		n/a	5.0±1.9 (2.7-11)	11.8±8.9 (3.9-30)	11.0±4.5 (5.7-17.1)
9HPT mean ± SD (range)	**Dominant**	n/a	22.7±5.6 (15.2-36.7)	28±6.9 (18.3-39.8)	30.2±7.9 (20.3-46.2)
	Non-dominant	n/a	22.6±5.2 (16.3-32.5)	28.9±8.6 (18.6-45.3)	31.8±7.7 (23.7-47.2)
SDMT mean ± SD (range)		n/a	52.7±13.0 (10-65)	52.6±9.6 (39-72)	41.6±13.9 (11-62)
3 sec PASAT mean ± SD (range)		n/a	43.9±10.9 (27-55)	49±10.4 (28-60)	41.6±11.9 (21-58)

EDSS = Expanded Disability Status Scale; 25FTW = 25-foot timed walk (seconds); 9HPT = nine-hole peg test (seconds);

Note: For the 25FTW, four MS patients could not finish the test. One MS patient could not finish the 9HPT (Dominant hand) and three MS patients could not finish the 9HPT (Nondominant hand).

3.3.2 Topographic signatures of CNS tissue injury in Multiple Sclerosis

"Visible" tissue damage (lesions in brain WM and the atrophy of the cortex and the cervical spinal cord) and "invisible" tissue damage (reduced $R2t*$ in cortical NAGM and subcortical NAWM of MS patients) were identified and quantified. Group-wise, $R2t*$ of GM readily distinguished HC from MS patients (Fig. 3.2). Cortical thickness was not significantly different between HC and MS groups although trends for reduced thickness were observed in the progressive MS groups (Fig. 3.2). Decreased (1.96 standard deviations lower than mean value of HC group) $R2t*$ of NAGM was present in 48% of the MS patients compared to decreased cortical thickness in only 9% of the MS patients. Group comparisons based on $R2t*$ of subcortical WM, WM tissue damage load (TDL) and cervical spinal cord CSA (Fig. 3.3) showed significant differences between MS patients and HC. There were no detectable lesions in WM of HC, hence HC TDL = 0. Decreased (1.96 standard deviations lower than mean value of HC group) subcortical WM $R2t*$ was present in 43% of the patients, and decreased CSA was present in 45% of the patients.
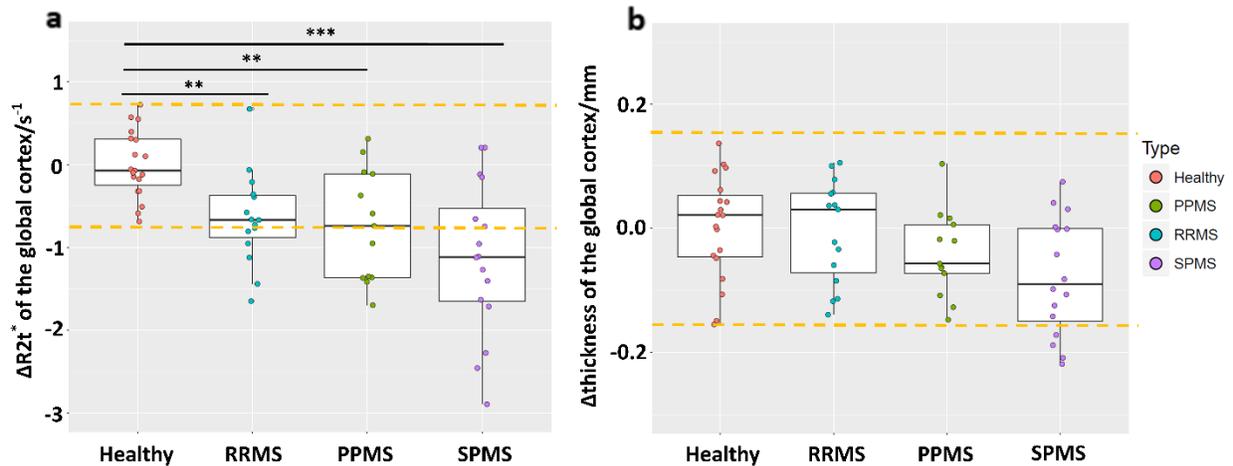
Figure 3.2 Group comparisons based on the mean global cortical R2t* (a) and mean global cortical thickness (b). Cortical *R2t** performs better than thickness in distinguishing MS patients from HC on both group and individual levels. At the individual level, decreased (1.96 standard deviations of HC group lower than mean value of HC group) *R2t** was present in 48% of MS patients compared to decreased cortical thickness in only 9%. Yellow dashed lines indicate 1.96 standard deviations of HC group lower/ higher than mean value of HC group. Boxes represent the interquartile ranges; the horizontal lines within the boxes indicate median values, points are median values of individual patients. p<0.001 ***, p<0.01 **, p<0.05 *. All p values were determined after adjusting for multiple comparisons using false discovery rate.

41
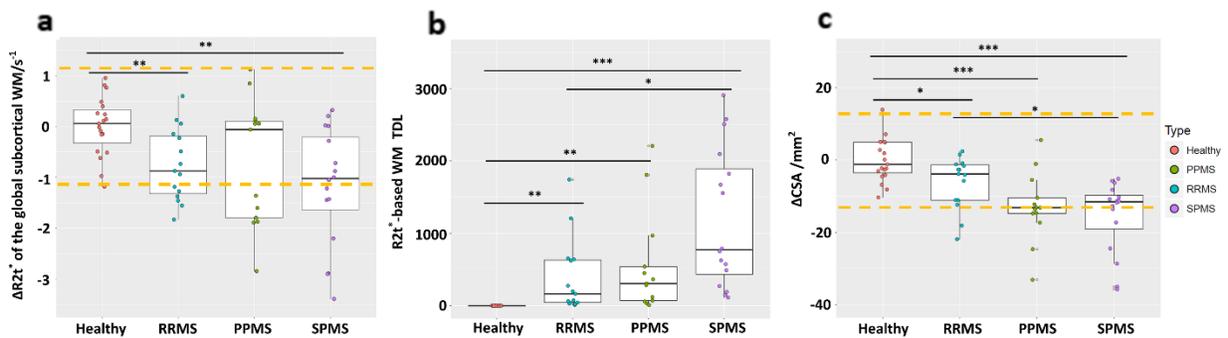
Figure 3.3 Group comparisons based on the mean global subcortical WM R2t* (a), WM TDL (b), and mean CSA (c). Most MS patients showed decreased *R2t** in subcortical NAWM and mean spinal cord CSA (averaged spinal cord cross-sectional area from C1 to C4). Yellow dashed lines indicate 1.96 standard deviations of HC group lower/ higher than mean value of HC group. Boxes represent the interquartile ranges; the horizontal lines within the boxes indicate median values, points are median values of individual patients. $p < 0.001$ ***, $p < 0.01$ **, $p < 0.05$ *. All p values were determined after adjusting for multiple comparisons using false discovery rate.

Since our measurements in cortical GM and subcortical WM did not show significant differences between MS subtypes, all further analyses were performed for MS patients without separation into MS sub-groups. Since there were no significant difference of *R2t** and cortical thickness measurement between left and right hemisphere (see supporting information), the values of *R2t** and TH in the left and right hemispheres were averaged for corresponding ROIs.

The fitting results for *R2t** and Thickness per equation (3.3) are listed in supporting information. Since not all coefficients K_n between of ROIs were statistically significant, for further analysis we use the same coefficients *K* for all ROIs that were determined by fitting global values of *R2t** and Thickness. These coefficients are: 0.0303 (GM *R2t**), 0.0211 (subcortical WM *R2t**) and -0.0052 (GM thickness). These calculated baseline values were subtracted from the values of individual HC and MS subjects to generate *ΔR2t** and ΔThickness. The p-values of the correlations between age and global mean *R2t** in GM and subcortical WM, and mean cortical thickness are 0.0006, 0.046, 0.003, respectively.

Not all regions of GM and WM were affected equally. To establish patterns of tissue damage between different cortical and subcortical ROIs, we first performed Pearson's correlation analysis of $\Delta R2t*$ in each NAGM cortical region ($\Delta R2t_n^*$) versus mean NAGM cortical $\Delta R2t*$ using data for all 44 MS patients. A similar procedure was performed for cortical thickness and $\Delta R2t*$ of subcortical NAWM. Patterns of tissue damage, as determined by r values from correlation analyses are presented on brain surface maps (Fig. 3.4). The patterns of tissue damage were similar for NAGM and subcortical NAWM: tissue damage in parietal and occipital cortices reflected best with mean cortical tissue damage. Cortical thickness showed a different pattern than $R2t*$ measurement; changes in temporal cortices showed the strongest correlation with the mean cortex thickness change.
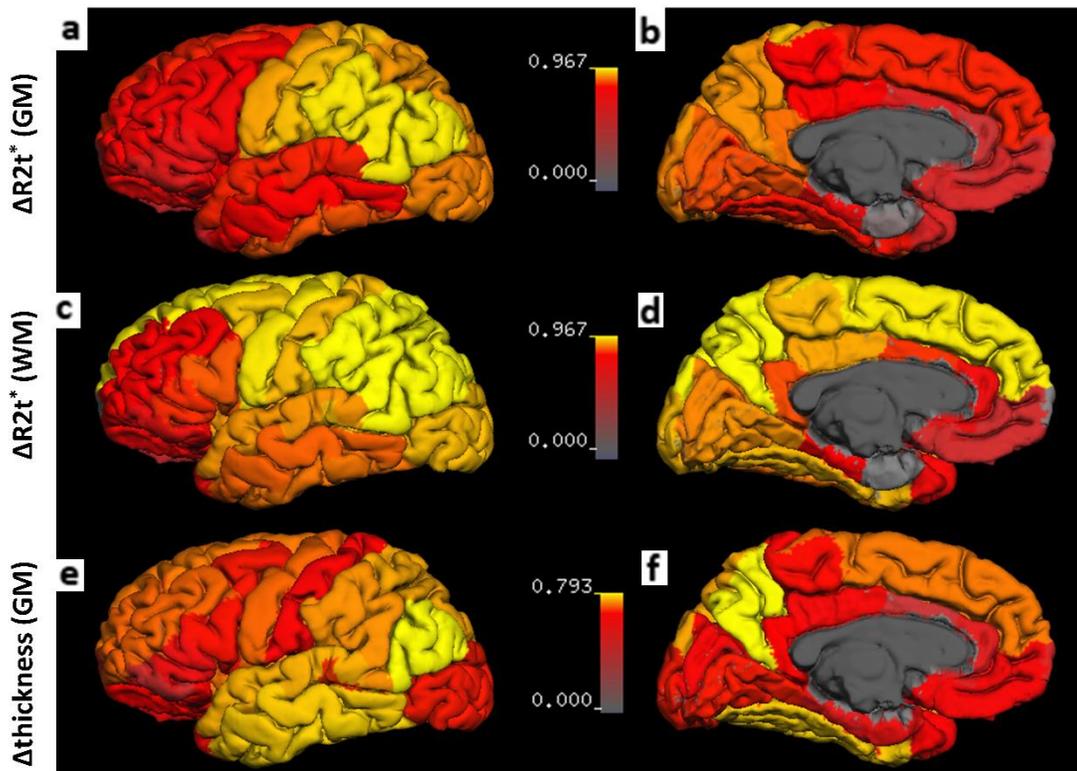
Figure 3.4 Topographic signatures of tissue damage in NAGM and NAWM. (a,b): r value from Pearson's correlation analysis between $\Delta R2t^*$ of each cortical region (n) vs. $\Delta R2t^*$ of the mean global cerebral NAGM for all MS patients (without separation on MS sub-groups) are mapped on the cortical surface. Decrease of $R2t^*$ in the motor and postcentral cortex were most reflective of the mean global cortical decrease of $R2t^*$. (c,d): The same analysis for subcortical NAWM. The pattern of change in $\Delta R2t^*$ of NAWM was similar to NAGM. (e,f): The same analysis for cortical GM ΔThickness. Decrease of thickness in the temporal lobe correlated most with the mean decrease of thickness in global cortex. The surface of the cortex was generated by FreeSurfer. Deep GM structures, WM and ventricles were excluded. Color bars represent r value from Pearson's correlation analysis.

3.3.3 Interrelationships between MS tissue injury in different topographic region

Figures 3.2, 3.3 and 3.4 show the presence of tissue damage in spinal cord, GM, and WM in MS patients. To test the hypothesis that the strength of tissue damage in different parts of CNS could be interrelated, thus forming MS-related topographic signatures, we ran a correlation analysis between all the quantitative parameters defining MS tissue damage in spinal cord, NAGM, NAWM and MS lesions. The sizes of spinal cord at C1, C2, C3 and C4 are highly correlated (Supporting information: Figure 3.7). Since only one focal MS lesion was noted at C1 level, CSA of C1 was used to correlate with tissue damage measurement in brain and clinical scores.

CSA at C1, tissue damage in NAGM and NAWM in the brain, and tissue damage load of lesions in the brain showed multiple interrelationships, irrespective of MS clinical subtype (Table 3.2). Reduced $R2t^*$ values in global NAGM and subcortical NAWM were significantly correlated with

reduced CSA of C1 (Table 3.2). In contrast, no significant correlations between reduced CSA at C1 and reduced $R2t^*$ of GM or subcortical WM was seen for HC (p=0.68 and 0.88 respectively) suggesting that correlations in MS patients are pathology-related. Similarly, MS patients with smaller CSA also had proportionately thinner global cerebral cortices but no significant correlation was found between C1 CSA and thickness of GM for HC (p=0.52).

In addition to the assessments of relationships between characteristics of the spinal cord and the brain globally (Table 3.2), specific cortical regions were also examined (Fig. 3.5). Tissue damage characterized by $\Delta R2t^*$ of middle temporal, inferior temporal and inferior parietal cortical regions of NAGM showed the most significant correlations with the C1 spinal cord size. For subcortical NAWM, the $\Delta R2t^*$ of the middle temporal region demonstrated the greatest correlation with CSA at C1. In contrast and not unexpectedly, among all 34 cortical regions, the thickness of the motor cortex was most correlated with C1 spinal cord size (Fig. 3.5). Thickness of other cortical regions showed either nonsignificant or weak correlations with C1 CSA (Fig. 3.5).

Table 3.2 Summary of correlations between different tissue damage measurements in CNS for 44 MS patients. $p<0.001$ ***, $p<0.01$ **, $p<0.05$ *. All the p values presented after correction for multiple comparison via false discovery rate.

	$\Delta R2t^*$ of global NAGM	$\Delta R2t^*$ of global subcortical NAWM	ΔTh of global NAGM	Brain WM TDL
ΔCSA of C1	* r = 0.39	* r =0.38	** r =0.43	r =-0.25
$\Delta R2t^*$ of global NAGM		*** r =0.80	r =0.079	r =-0.31
$\Delta R2t^*$ of global subcortical NAWM			r =0.18	*** r =-0.55
ΔTh of global NAGM				** r =-0.46
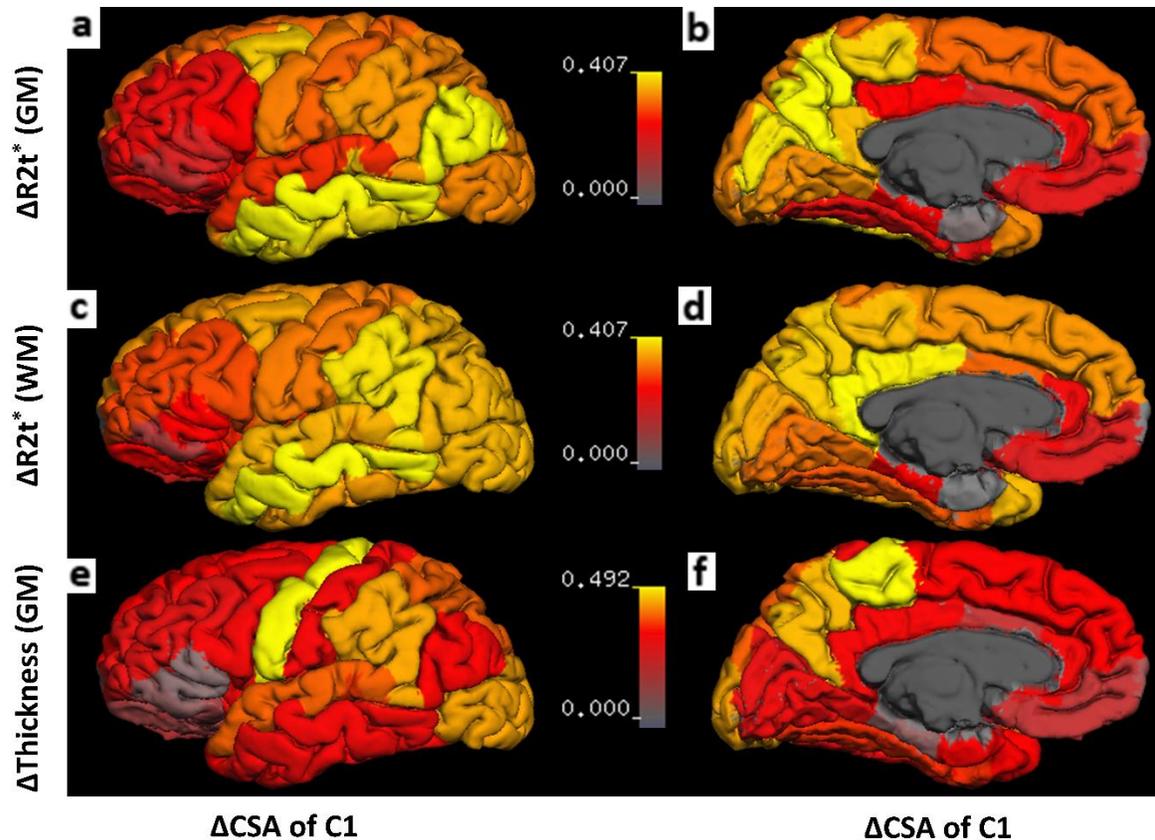
Figure 3.5 Results of the correlation analyses between tissue damage in the brain and the spinal cord based on all 44 MS patients. All images show the r values of the Pearson's correlation coefficient mapped on the cortical surface. (a,b): correlation between ΔCSA of C1 and *ΔR2t** of cortical GM. The primary motor cortex and the somatosensory cortex showed moderate correlations with C1 ΔCSA. (c,d): correlation between ΔCSA of C1 and *ΔR2t** in subcortical WM regions. The middle temporal subcortical WM demonstrated the highest correlations with C1 ΔCSA. (e,f): correlation between ΔCSA of C1 and ΔThickness in cortical regions. The primary motor cortex showed the strongest correlation with C1 ΔCSA, while other regions either showed very weak or no significant correlations. The surface of the cortex was generated by FreeSurfer. Deep GM structures, WM and ventricles were excluded. Color bars represent r values.

Table 3.2 also shows significant correlations between tissue damage measured by mean $R2t^*$ of NAGM and mean $R2t^*$ of the subcortical NAWM. To assess the relative severity of tissue damage in adjacent regions of cortical NAGM and subcortical NAWM, linear regression based on all 44 MS patients was performed between decrease of $R2t^*$ in each subcortical NAWM region versus corresponding cortical NAGM regions (per Eq. (3.4) in Methods). A slope less than 1 indicates that NAGM $R2t^*$ has larger relative reduction than NAWM. With the exception of the inferior temporal cortex, all NAGM regions showed larger relative changes than NAWM (Fig. 3.6).
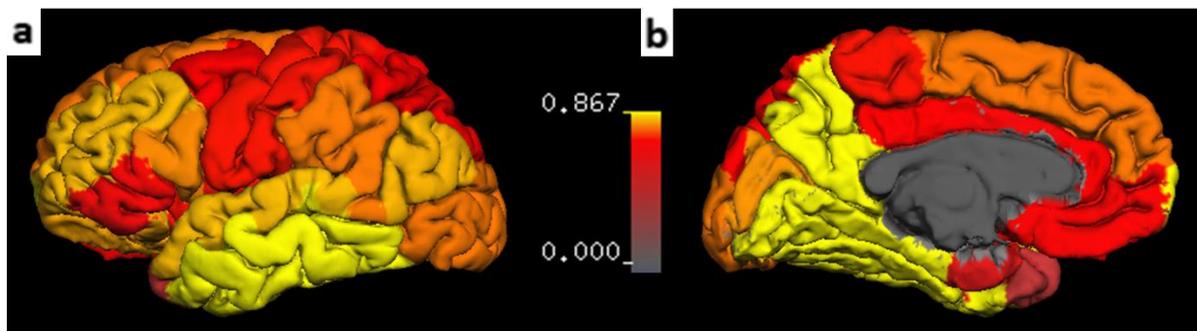
Figure 3.6 Slopes of linear regressions between $\Delta R2t^*$ of adjacent subcortical NAWM vs. $\Delta R2t^*$ of matched cortical NAGM regions (parameter qn in Eq. (3.4)). Data are based on all 44 MS patients. Images represent parameter q_n projected on the cortical surface generated by FreeSurfer. Deep GM structures, WM and ventricles were excluded. Color bar represents q_n values.

3.3.4 Relationship between clinical test performance and tissue damage in brain and spinal cord in MS.

Table 3.3 Summary of clinical test correlations with spinal cord size at C1, mean $R2t^*$ of global cortex, mean $R2t^*$ of subcortical WM, mean thickness of global cortex, and brain

white matter tissue damage load for the 44 MS subjects. *r* is Pearson correlation coefficient, all the p values presented after correction for multiple comparison via false discovery rate. p<0.001 ***, p<0.01 **, p<0.05 *.

	ΔCSA at C1		Mean $\Delta R2t^*$ of cortex		Mean $\Delta R2t^*$ of subcortical wm		Mean ΔTh of cortex		TDL	
	r	p	r	p	r	p	r	p	r	p
EDSS	-0.61	***	-0.12	0.51	-0.080	0.65	-0.46	**	0.36	*
25FTW	-0.62	***	-0.19	0.27	-0.16	0.36	-0.41	*	0.29	0.085
9HPT(Dominant)	0.47	**	0.37	*	0.21	0.22	0.26	0.14	-0.25	0.14
9HPT(NonDominant)	0.34	*	0.53	**	0.42	*	0.21	0.16	-0.32	0.056
PASAT	0.051	0.77	0.45	**	0.46	**	0.016	0.92	-0.39	*
SDMT	0.14	0.42	0.30	0.051	0.39	*	0.26	0.23	-0.44	*

To evaluate the relationships between tissue damage and MS clinical signs, mean *ΔR2t** of NAGM and NAWM , mean cortical ΔTh, spinal cord atrophy (ΔCSA at C1) and tissue damage load (TDL) in brain WM lesions were each assessed for correlations with clinical test results (EDSS, 25FTW, 9HPT, SDMT and PASAT) (Table 3.3). Region-wise results are presented in the supporting information. ΔCSA at C1 had the most significant correlations with motor-related clinical tests EDSS, 25FTW, and 9HPT (dominant and nondominant hands). Similar correlations with clinical tests were found for C2, C3 and C4 (not shown). Mean *ΔR2t** of global cortex showed significant correlation with 9HPT (dominant and nondominant hands) and PASAT. WM Tissue damage load based on *R2t** correlated with EDSS, PASAT and SDMT. In the present 44 patient cohort, gender, age and MS duration did not correlate with physical impairment scores.

3.4 Discussion:

In this study, we addressed three questions. One was to ask if we could detect "invisible" pathology not recognized by standard clinical MRI (based on "weighted" MRI contrasts) in the CNS of MS patients using a new imaging marker, $R2t^*$. The second related question was to ask whether there existed topographic signatures of MS pathology (visible and invisible) in CNS common to MS patients. The third question was whether our quantitative tissue damage measurements reflected neurological impairment in MS.

3.4.1 $R2t^*$ Reveals Tissue Damage not Readily Visible by Clinical MRI

Tissue integrity in the brain cortical NAGM and subcortical NAWM of MS patients was quantified using the gradient recalled echo MRI signal decay rate constant, $R2t^*$. This parameter ($R2t^*$) is a quantitative measure that has been shown to correlate with tissue cellular density in normal human brain[60] and was decreased in brain areas in concert with the loss of tissue cellular integrity in Alzheimer's disease[93]. Since previous studies demonstrated reduced $R2$ values in areas of demyelination in the spinal cord[84] and brain[19, 85], and reduced total $R2^*$ has been noted in areas of WM[92] and cortical demyelination[86, 94], we expected that a more tissue-specific parameter $R2t^*$ would be reduced by demyelination as well. Indeed, in our cohort, MS patients had lower $R2t^*$ values in both WM and GM as compared with HC participants. We were able to identify regions of "invisible" tissue damage based on comparison of quantitative $R2t^*$ measurements in MS and HC participants. The "visible" part of brain tissue damage was also quantitatively assessed in our study by measuring cortical thickness and a quantitative composite measure of WM damage characterizing both WM lesion volume and tissue damage within the lesions - MS lesion Tissue Damage Load (TDL). The cervical spinal cord was assessed by measuring upper cervical cord CSA, reductions which predominantly reflect axon loss.

Since age affects *R2t** and reduces cortical thickness, baseline correction was used to account for age effects. For spinal cord, no significant correlation was found between spinal cord CSA and age, height, gender, brain size and disease duration in our data.

For the first question, tissue damage of various degree not apparent on standard MRI was present in most MS patients in most parts of CNS we examined. Significant atrophy was present in the cervical spinal cord and cortical GM with the motor cortex and temporal cortex showing the most significant volume reductions in the brain. Although most cortical regions were affected in at least some patients, the motor cortex and postcentral cortex demonstrated the greatest decreased of *R2t** compared to HC. Brain subcortical WM demonstrated a similar pattern, in accord with the strong correlation between *R2t** in GM and subcortical WM. No significant correlation between *R2t** of cortical NAGM and cortical thickness was found, which means that *R2t** and thickness are two complementary measurements – the latter showing reduction in tissue volume while the former showing loss of remaining tissue integrity. We had hypothesized that tissue quality changes (measured by *R2t**) should be evident before atrophy. The difference between cortical thickness of healthy controls and MS patients were not statistically significant, possibly due to the relatively small cohort size. Nevertheless, a decreasing trend of cortical thickness was observed in this study, which is consistent with a recent report showing group differences measured by normalized gray matter volume in a larger cohort of 206 MS patients[95]. Normalized gray matter volume was also measured in our study and similar trend as in[95] were found (Supporting Information: Figure 3.8). Compared with cortical thickness, *R2t** measurement readily differentiated MS patients from healthy controls even within our small cohort size. Since more patients showed significant decrease in *R2t** of the NAGM but not in cortical thickness, we suggest that *R2t** is more sensitive

to tissue injury than cortical atrophy, and has a potential to be used as a sensitive biomarker for MS related clinical trials.

3.4.2 Topographic Signatures of MS Pathology Have Been Identified

To answer the second question, correlations between tissue damage in different parts of CNS were examined. Tissue damage in the cervical spinal cord (assessed by cord atrophy) significantly correlated with tissue damage in the brain cortical NAGM (assessed by cortical atrophy and reduced *R2t**), subcortical NAWM (assessed by reduced *R2t**) and WM MS lesions (assessed by *R2t**-based Tissue Damage Load). Whereas correlations existed between tissue damage in several different parts of the brain and CSA of cervical cord, the strongest and the most significant correlation was found between atrophy of the spinal cord and the thickness of brain motor cortex. This was not surprising since these two structures are physically and functionally linked, with axons from motor cortical neurons extending through the cervical cord; when a motor neuron dies, its axon degenerate.

Another interrelationship (cortical GM – subcortical WM) was identified by strong correlations between tissue damage in the adjacent regions of cortical GM and subcortical WM. Table 2 shows that decreases of *R2t** in cortical NAGM and subcortical NAWM were highly correlated. We further examined the relative severity of tissue damage between NAGM and NAWM. Our measurements show that *R2t** changes in GM were relatively bigger in most ROIs than in adjacent WM ROIs, which may suggest that tissue damage is relatively more severe in cortical NAGM compared with subcortical NAWM. This interpretation would be in accord with a previous study which found the percentage of demyelinated area was significantly higher in cerebral cortex than in WM of MS patients[96].

It was also notable that the reduced CSA of the cervical spinal cord significantly correlated with "invisible" tissue damage (assessed by *R2t**) in the primary motor cortex, and temporal and inferior parietal cortices. Interestingly, correlations with cord CSA were noted even for regions of cortex, such as occipital, that do not directly link to the spinal cord. Although the biological meaning of these correlations is not obvious, they did not exist in HC indicating that they are pathology-related. The significant associations between visible and invisible tissue damage in all parts of CNS further support the concept of MS as a global disease of the CNS.

Certain regions of the CNS are known to be more frequently affected by MS. In particular, these are periventricular areas, juxtacortical white matter, corpus callosum, cortical gray matter, optic nerves, medial longitudinal fasciculus, cerebellar tracts, and the cervical spinal cord[97]. Although the current study did not examine the tissue damage in every region of CNS, our data still showed tissue damage patterns in the CNS of the 44 MS patients in our cohort. Whether these patterns are generally common to MS patients will need confirmation in larger and different MS patient cohorts. These data are also consistent with recent reports of correlations between spinal cord MRI measurement and retinal layers in multiple sclerosis[98], and associations between deep gray matter tissue damage and degeneration in cortex and spinal cord[99].

3.4.3 *R2t** correlates with MS patients' Neurological Impairments

To address the third question, we examined relationships of tissue damage assessed by *R2t** and cortical thickness in different parts of the CNS and C1 CSA with neurological function. A composite measure for tissue damage load (TDL) based on *ΔR2t** values in the WM lesions correlated with EDSS, but to a lesser degree than cervical CSA. Of all our imaging measures, the cervical cord CSA correlated best with physical impairment defined by EDSS and 25FTW tests, in accord with several previous studies[100].

Not surprising, no correlation was found in this study between cognitive tests (SDMT and PASAT) and spinal cord cross-sectional size. On the other hand, $\Delta R2t^*$ values of the entire cortical GM and several specific cortical regions correlated significantly with SDMT and PASAT scores. These correlations with cognitive test results were more widespread and greater than for cortical thickness, indicating that $\Delta R2t^*$ is more sensitive to tissue damage. The region-wise analysis showed the correlation between GM, subcortical WM $R2t^*$ and 9HPT (Dominant and nondominant) were similar. However, subcortical WM R2t* showed stronger correlation with cognitive tests compared with GM $R2t^*$.

Based on these findings we can hypothesize that $R2t^*$ alterations might be an early indicator of MS pathology, detectable at a time when atrophy is not apparent. In the future, we plan to create a model incorporating $R2t^*$ and other imaging parameters, to explain concurrent physical impairment status with the ultimate goal of predicting future MS course.

In this study, we have not reported tissue-specific $R2t^*$ measurements in the upper cervical spinal cord due to technical issues related to low signal-to-noise ratio in our data in the spinal cord. RF coils covering both brain and spinal cord would allow simultaneous $R2t^*$ mapping in the brain and spinal cord without increased scanning time. Improvement in RF coil design could potentially allow $R2t^*$ mapping of small CNS structures (e.g. optical nerve) that was not visible with our current design. Generating $R2t^*$ maps on the scanner requires computer power that is currently not available from manufacturers and therefore we analyzed data off-line. While timing is crucial for diagnostic acute medical conditions (e.g. stroke, heart attack, etc.), delays with generating diagnostic images based on $R2t^*$ metric can be tolerated for chronic conditions like MS. Future improvement of the time to generate usable results will likely be resolved with the development of more powerful computers and using cloud computing.

3.5 Conclusion

In conclusion, we report the novel finding that a quantitative measure of MS tissue damage based on the tissue cellular specific transverse relaxation rate constant, *R2t**, can sensitively detect MS-related pathology in cortical NAGM, subcortical NAWM and WM lesions. The method demonstrated tissue damage patterns in the CNS of the MS cohort. Our data shed light on the interrelationships of damage throughout the brain and cervical spinal cord, while supporting the idea of MS as a global CNS disease. Our results showed that while spinal cord CSA is a reliable marker for changes in motor functions, the reduction in the *R2t** of GM and WM is a reliable indicator of cognitive dysfunction.

3.6 Supporting Information:
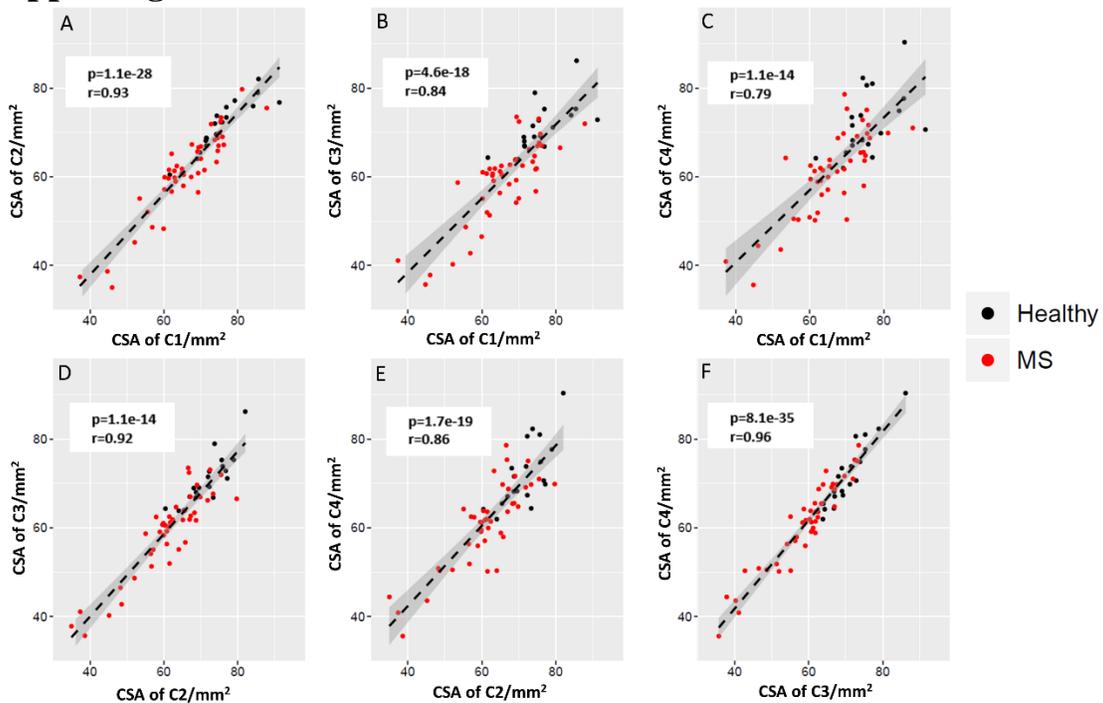
Figure 3.7. Correlations between cross-sectional areas in C1, C2, C3 and C4. First row: correlation between C1 and (A) C2, (B) C3, (C) C4. Second row: correlation between C2 and (D) C3, (E) C4, correlation between C3 and C4 is shown in (F). Data from healthy controls (black dots) and MS patients (red dots) are included. Each point represents a single subject.
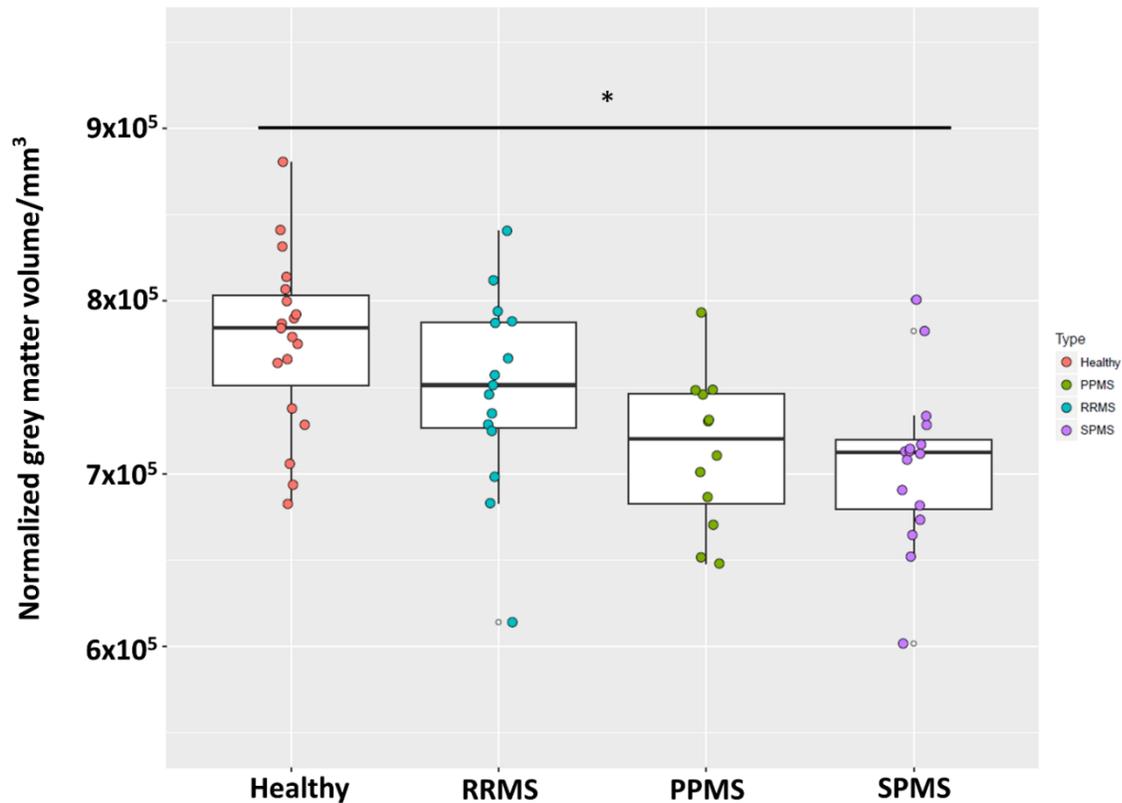
Figure 3.8. Group comparisons based on the normalized cortical grey matter volume. SPMS group showed statistically significant decrease of normalized grey matter compared with healthy controls. RRMS and PPMS also showed decreasing trend of normalized grey matter compared with healthy controls, even though they were not statistically significant. Progressive MS groups (PPMS and SPMS) also demonstrated decreasing trend compared with RRMS group. Boxes represent the interquartile ranges; the horizontal lines within the boxes indicate median values, points are median values of individual patients. $p<0.001$ ***, $p<0.01$ **, $p<0.05$ *. All p values were determined after adjusting for multiple comparisons using false discovery rate.
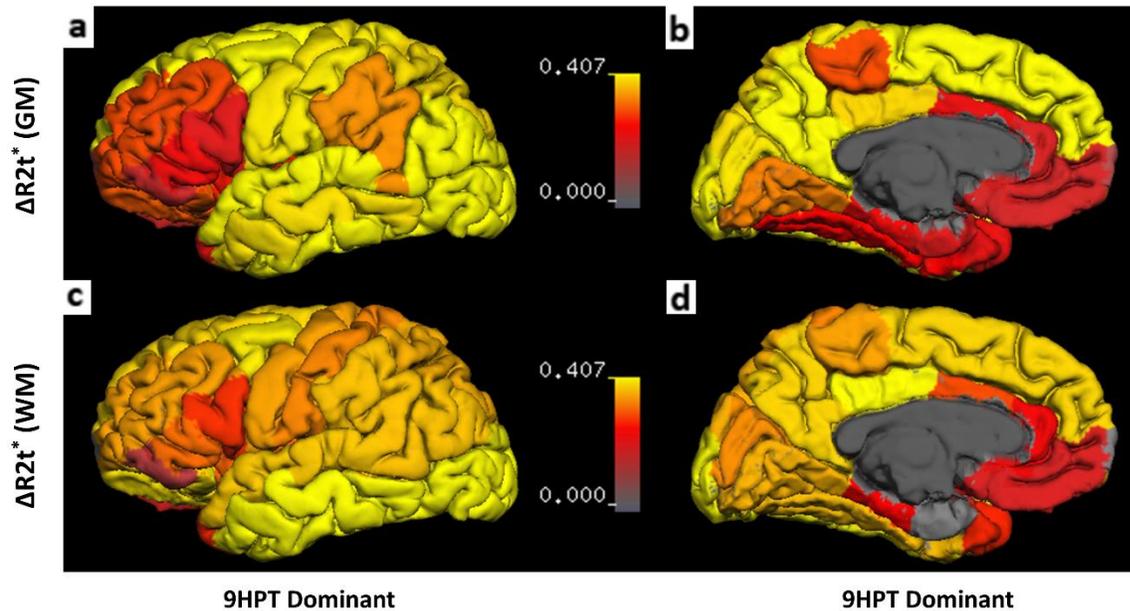
Figure 3.9 Results of the correlation analyses between the regional tissue damage in the brain and 9HPT (dominant hand) based on all 44 MS patients. All images show the r values of the Pearson's correlation coefficient mapped on the cortical surface. (a,b): correlation between 9HPT (dominant hand) and $\Delta R2t^*$ of cortical GM. The somatosensory cortex and occipital cortex showed moderate correlations with 9HPT. (c,d): correlation between 9HPT (dominant hand) and $\Delta R2t^*$ in subcortical WM regions. The middle temporal subcortical WM demonstrated the highest correlations with 9HPT. The surface of the cortex was generated by FreeSurfer. Deep GM structures, WM and ventricles were excluded. Color bars represent r values
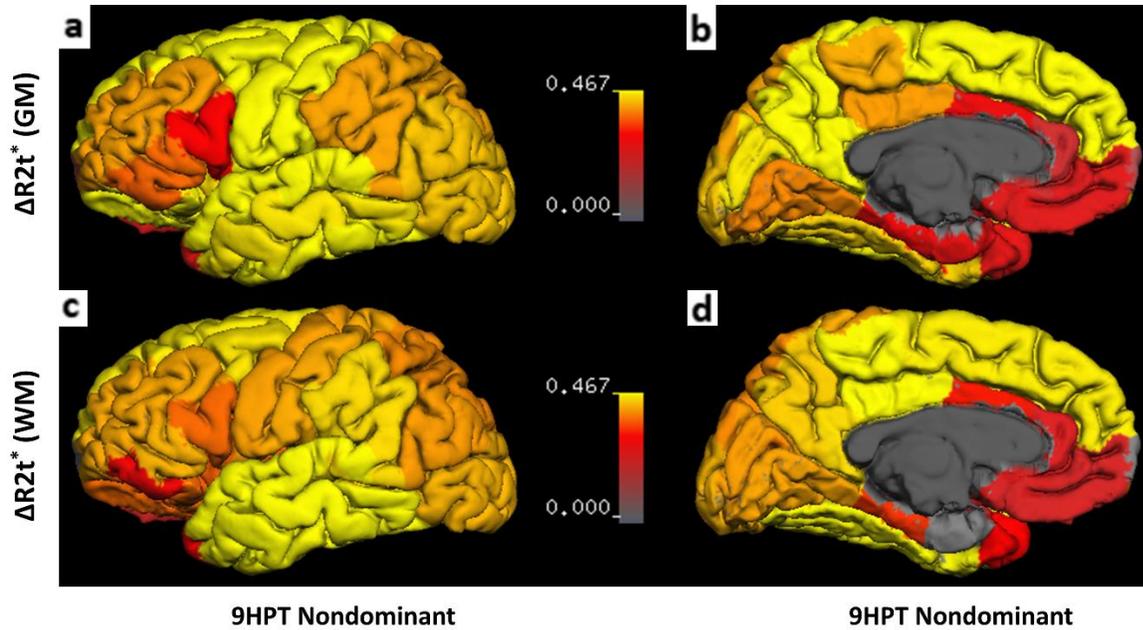
Figure 3.10 Results of the correlation analyses between regional tissue damage in the brain and 9HPT (nondominant hand) based on all 44 MS patients. All images show the r values of the Pearson's correlation coefficient mapped on the cortical surface. (a,b): correlation between 9HPT (nondominant hand) and *ΔR2t** of cortical GM. The primary motor cortex and the somatosensory cortex showed moderate to strong correlations with 9HPT. (c,d): correlation between 9HPT (nondominant hand) and *ΔR2t** in subcortical WM regions. The temporal subcortical WM demonstrated the highest correlations with 9HPT. The surface of the cortex was generated by FreeSurfer. Deep GM structures, WM and ventricles were excluded. Color bars represent r values
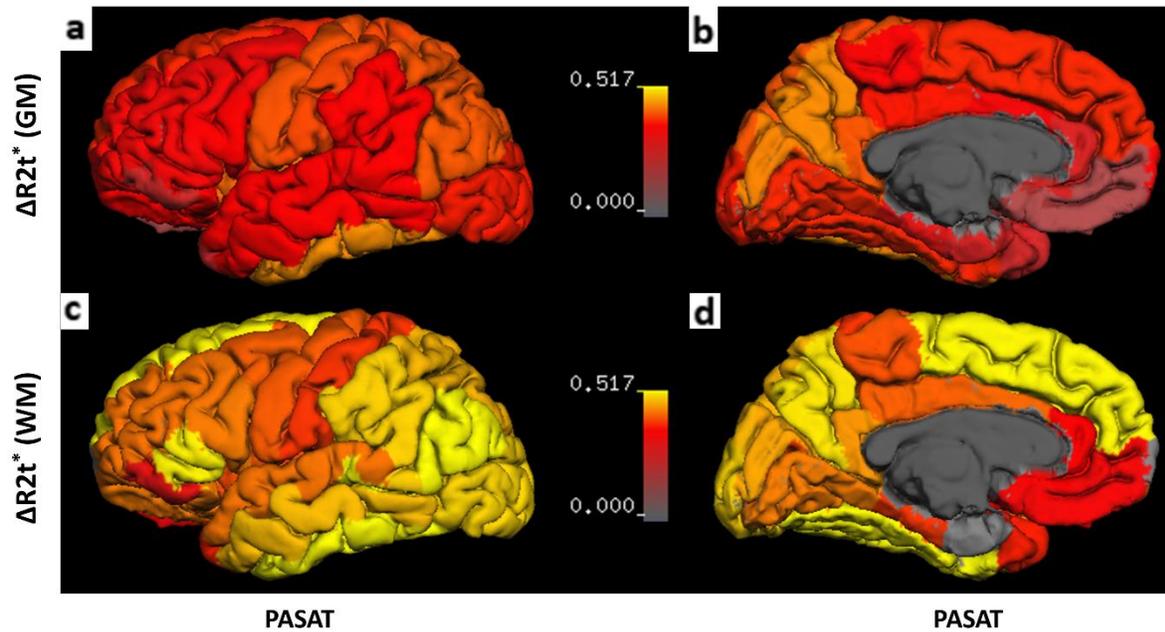
Figure 3.11 Results of the correlation analyses between regional tissue damage in the brain and PASAT based on all 44 MS patients. All images show the r values of the Pearson's correlation coefficient mapped on the cortical surface. (a,b): correlation between PASAT and *ΔR2t** of cortical GM. (c,d): correlation between PASAT and *ΔR2t** in subcortical WM regions. Subcortical WM *R2t** showed stronger correlation with PASAT than cortical *R2t**. The surface of the cortex was generated by FreeSurfer. Deep GM structures, WM and ventricles were excluded. Color bars represent r values
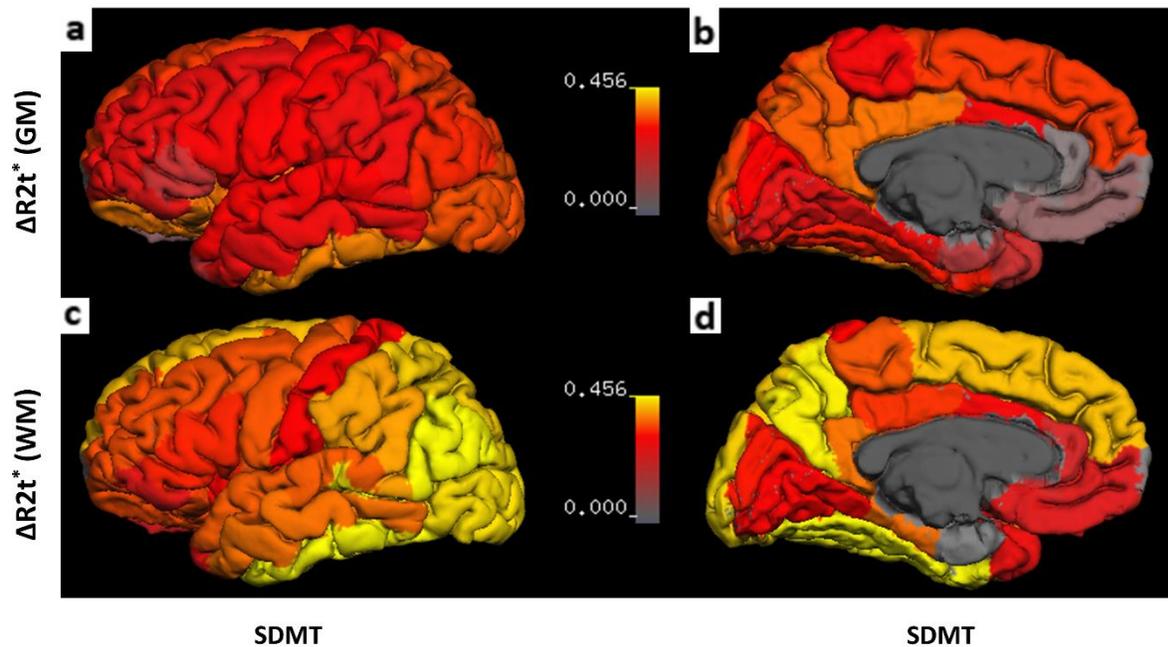
Figure 3.12 Results of the correlation analyses between regional tissue damage in the brain and SDMT based on all 44 MS patients. All images show the r values of the Pearson's correlation coefficient mapped on the cortical surface. (a,b): correlation between SDMT and $\Delta R2t^*$ of cortical GM. (c,d): correlation between SDMT and $\Delta R2t^*$ in subcortical WM regions. Subcortical WM $R2t^*$ showed stronger correlation with SDMT than cortical $R2t^*$. The surface of the cortex was generated by FreeSurfer. Deep GM structures, WM and ventricles were excluded. Color bars represent r values
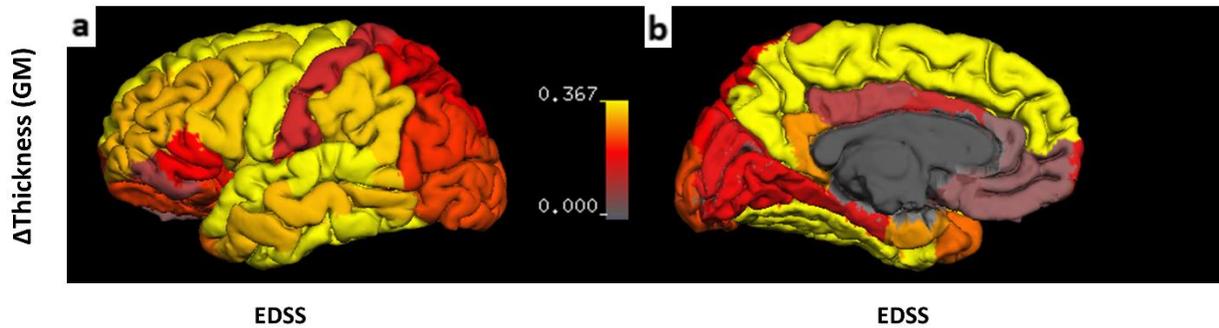
Figure 3.13 Results of the correlation analyses between brain regional cortical thickness and EDSS based on all 44 MS patients. All images show the r values of the Pearson's correlation coefficient mapped on the cortical surface. The thickness of primary motor cortex showed the strongest correlation with EDSS. The surface of the cortex was generated by FreeSurfer. Deep GM structures, WM and ventricles were excluded. Color bars represent r values.
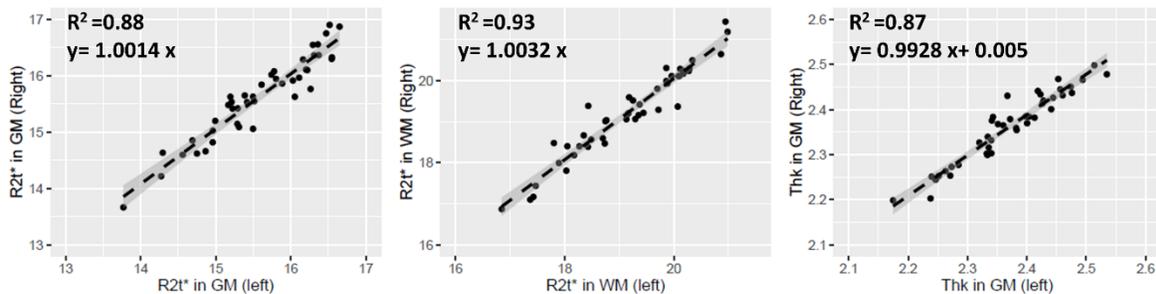
Figure 3.14 Correlation analysis between $R2t*$ in GM, $R2t*$ in WM and cortical thickness values in left and right hemispheres. Our result showed that the left hemisphere and right hemisphere $R2t*$ and thickness measurements were highly correlated.

Table 3.4: Summary of intercept values A_n resulted from the fitting results for $R2t*$ and thickness. The p values for all A_n are smaller than 0.00001 after multiple comparison.

ROI	Cortical GM	Subcortical WM	Cortical Thickness

bankssts	15.42	19.36	2.91
caudal anterior cingulate	16.33	19.66	2.79
caudal middle frontal	14.71	19.01	2.66
cuneus	17.01	19.22	1.92
entorhinal	12.41	13.93	3.56
frontalpole	12.68	17.02	2.98
fusiform	15.12	18.74	2.73
inferiorparietal	15.34	18.82	3.13
inferiortemporal	14.91	18.52	2.70
insula	12.42	18.21	2.42
isthmuscingulate	16.24	20.88	2.66
lateraloccipital	16.39	18.94	2.22
lateralorbitofrontal	12.29	17.63	2.49
lingual	16.91	18.80	3.22
medialorbitofrontal	12.72	18.23	3.23
middle temporal	14.55	18.66	2.39
parahippocampal	14.67	16.65	2.72

paracentral	15.62	18.71	2.79
parsopercularis	13.44	19.01	2.50
parsorbitalis	14.39	18.08	1.62
parstriangularis	14.75	19.39	2.26
pericalcarine	16.99	18.59	2.66
postcentral	15.84	18.40	2.75
posteriorcingulate	14.86	19.38	2.63
precentral	15.03	18.87	3.02
precuneus	15.49	19.04	2.38
rostralanteriorcingulate	12.76	20.51	2.83
rostral middle frontal	14.51	19.35	2.42
superior frontal	13.89	18.39	3.18
superior parietal	15.42	18.75	2.87
superior temporal	14.28	18.19	2.92
supramarginal	14.93	19.12	3.78
temporalpole	12.25	13.60	2.65
transverse temporal	13.95	17.43	3.33

Table 3.5: Summary of r values presented in figure 3.9, 3.10, 3.11, 3.12, 3.13.

ROI	9HPT (Dominant)		9HPT (Nondominant)		PASAT		SDMT		EDSS
	GM	WM	GM	WM	GM	WM	GM	WM	Thk
bankssts	0.44	0.37	0.47	0.45	0.29	0.52	0.29	0.45	-0.40
caudal anterior cingulate	0.16	0.29	0.21	0.31	0.29	0.42	0.24	0.23	0.08
caudal middle frontal	0.55	0.40	0.56	0.45	0.27	0.41	0.20	0.35	-0.35
cuneus	0.39	0.33	0.46	0.40	0.44	0.46	0.28	0.31	-0.12
fusiform	0.23	0.36	0.44	0.53	0.37	0.53	0.31	0.49	-0.42
inferiorparietal	0.41	0.37	0.43	0.40	0.41	0.53	0.32	0.47	-0.23
inferiortemporal	0.45	0.47	0.54	0.50	0.44	0.58	0.38	0.46	-0.38
insula	0.25	0.30	0.45	0.36	0.42	0.40	0.37	0.30	-0.21
isthmuscingulate	0.41	0.38	0.48	0.45	0.41	0.45	0.37	0.37	-0.30
lateraloccipital	0.45	0.44	0.43	0.42	0.37	0.49	0.35	0.44	-0.25
lateralorbitofrontal	0.30	0.39	0.49	0.37	0.33	0.43	0.38	0.34	-0.24
lingual	0.33	0.36	0.39	0.41	0.37	0.43	0.19	0.27	-0.14
medialorbitofrontal	0.11	0.12	0.17	0.14	0.08	0.28	-0.03	0.16	0.02
middle temporal	0.39	0.48	0.45	0.54	0.33	0.47	0.21	0.37	-0.32
parahippocampal	0.18	0.23	0.22	0.33	0.22	0.38	0.22	0.37	-0.12
paracentral	0.29	0.35	0.41	0.47	0.30	0.40	0.23	0.35	-0.44
parsopercularis	0.13	0.27	0.29	0.37	0.32	0.43	0.24	0.32	-0.34
parsorbitalis	0.11	0.07	0.36	0.24	0.16	0.22	0.18	0.18	-0.05

parstriangularis	0.17	0.31	0.37	0.42	0.28	0.51	0.12	0.32	-0.20
pericalcarine	0.41	0.34	0.49	0.38	0.39	0.39	0.29	0.28	-0.03
postcentral	0.40	0.33	0.48	0.41	0.40	0.38	0.25	0.30	-0.09
posteriorcingulate	0.38	0.45	0.40	0.48	0.36	0.41	0.37	0.33	-0.05
precentral	0.39	0.35	0.47	0.41	0.40	0.41	0.27	0.35	-0.44
precuneus	0.48	0.38	0.51	0.43	0.44	0.50	0.36	0.45	-0.38
rostralanteriorcingulate	0.12	0.19	0.12	0.16	0.18	0.33	-0.01	0.14	-0.02
rostral middle frontal	0.29	0.35	0.41	0.41	0.28	0.42	0.21	0.35	-0.32
Superior frontal	0.43	0.38	0.47	0.46	0.37	0.51	0.33	0.42	-0.45
superior parietal	0.39	0.36	0.41	0.39	0.41	0.47	0.34	0.43	-0.18
superior temporal	0.45	0.37	0.49	0.47	0.34	0.43	0.27	0.36	-0.48
supramarginal	0.34	0.37	0.41	0.44	0.32	0.49	0.20	0.40	-0.33
temporalpole	0.16	0.26	0.18	0.30	0.16	0.37	-0.12	0.20	-0.27
transverse temporal	0.39	0.29	0.50	0.36	0.40	0.39	0.24	0.20	-0.28
Mean	0.32	0.33	0.40	0.40	0.33	0.43	0.25	0.34	-0.24
Standard Deviation	0.13	0.09	0.11	0.09	0.09	0.07	0.12	0.09	0.15

Table 3.6 List of ROIs in this study

	ROI in cortical gray matter	ROI in subcortical white matter

1	cortex-bankssts	wm-bankssts
2	cortex-caudal anterior cingulate	wm-caudal anterior cingulate
3	cortex-caudal middle frontal	wm-caudal middle frontal
4	cortex-cuneus	wm-cuneus
5	cortex-entorhinal	wm-entorhinal
6	cortex-frontalpole	wm-frontalpole
7	cortex-fusiform	wm-fusiform
8	cortex-inferior parietal	wm-inferior parietal
9	cortex-inferior temporal	wm-inferior temporal
10	cortex-insula	wm-insula
11	cortex-isthmus of the cingulate	wm-isthmus of cingulate
12	cortex-lateral occipital	wm-lateral occipital
13	cortex-lateral orbitofrontal	wm-lateral orbitofrontal
14	cortex-lingual	wm-lingual
15	cortex-medial orbitofrontal	wm-medial orbitofrontal
16	cortex-middle temporal	wm-middle temporal
17	cortex-parahippocampal	wm-parahippocampal
18	cortex-paracentral	wm-paracentral
19	cortex-parsopercularis	wm-parsopercularis
20	cortex-parsorbitalis	wm-parsorbitalis
21	cortex-parstriangularis	wm-parstriangularis
22	cortex-pericalcarine	wm-pericalcarine
23	cortex-postcentral	wm-postcentral

24	cortex-posterior cingulate	wm-posterior cingulate
25	cortex-precentral	wm-precentral
26	cortex-precuneus	wm-precuneus
27	cortex-rostral anterior cingulate	wm-rostral anterior cingulate
28	cortex-rostral middle frontal	wm-rostral middle frontal
29	cortex-superior frontal	wm-superior frontal
30	cortex-superior parietal	wm-superior parietal
31	cortex-superior temporal	wm-superior temporal
32	cortex-supramarginal	wm-supramarginal
33	cortex-temporalpole	wm-temporalpole
34	cortex-transverse temporal	wm-transverse temporal

Tissue Damage in MS Lesions based on *R2t**

R2t* values of each imaging voxel in the MS lesions were used to calculate a tissue damage score (TDS):

$$TDS = \frac{R2t_c^* - R2t^*}{R2t_c^*} \tag{3.5}$$

where *R2t** represents the actual value in a given voxel and *R2t_c** is a reference value calculated based on the distribution of *R2t** values in the NAWM of that individual. To calculate this reference value, Gaussian function was used to fit the upper half of the *R2t** histogram to avoid any influence from the "tails" in the histogram. "Normal reference" *R2t_c** value was defined as the center of the Gaussian function after fitting and was different for each subject. Total WM damage in the cerebral WM lesions of an individual patient was characterized by the tissue damage load

(TDL) calculated by summing individual TDS over all voxels (i) in cerebral MS lesions and multiplying by voxel volume *V*:

$$TDL = V \cdot \sum_{i=1:N} TDS_i \qquad (3.6)$$

Chapter 4: Evaluation of Myelin Damage in Multiple Sclerosis with SMART MRI

4.1. Introduction:

Magnetic resonance imaging (MRI) detects focal WM lesion with high accuracy and has been used extensively in MS diagnosis and disease monitoring [12, 13]. However, standard clinical MRI lacks specificity to MS pathology and correlates only modestly with MS disability [15, 16]. Many studies have been devoted to the development and experimental validation of quantitative methods sensitive to myelin damage, primarily by means of multiexponential $T2$ imaging of water trapped between myelin layers, magnetization transfer (MT) and diffusion tensor imaging [reviewed in Laule et al [101]].

One of these approaches, MT imaging, has been used to estimate myelin damage [28, 29]. In MT studies, a model of two cross-exchanging pools has been commonly used: a free (or liquid) pool, consisting of highly mobile protons associated with intracellular and extracellular water with long $T2$ (in the range 10 - 100 ms), and a bound pool, consisting of less mobile protons with an ultrashort $T2$ (less than 1ms) associated with macromolecules and membranes in biological tissues. Given its ultrashort $T2$, measuring signals from the bound pool is challenging. However, the exchange between the free pool and the bound pool allows indirect measurement of the bound pool using MT effects. Loss of myelin leads to decreased concentration of macromolecules and a consequent decrease of the bound pool.

Many MT studies in MS have used the MT ratio (MTR) which measures the relative MRI signal intensity decrease in the presence of an off-resonance radiofrequency pulse causing saturation of

the longitudinal magnetization of protons bound to macromolecules and consecutive transfer of this reduced magnetization to the free water. MTR depends on MRI pulse sequence parameters and is not quantitative. Unlike MTR, quantitative MT (qMT) experiments measure the fraction of bound protons versus total protons in both free and bound pools. This fraction has been called the Macromolecule Proton Fraction (MPF) [30-33]. Although only protons that can dynamically exchange with protons in free water can participate in the MT process, qMT offers improved specificity for myelin content and several studies have shown that qMT-defined MPF correlates with myelin concentration [34, 35]. However, qMT is limited by long acquisition times, low resolution, and high RF energy deposition (especially at magnetic fields 3T and higher).

Recently, we developed a novel technique, Simultaneous Multi-Angular Relaxometry of Tissue (SMART) MRI [62], that addresses these limitations. The SMART method is based on a gradient recalled echo (GRE) MRI and a model of GRE signal that accounts for cross-relaxation effects between "free" and "bound" water proton pools. Importantly, no MT pulses are used in SMART approach, thus overcoming high RF energy deposition associated with existing qMT approaches for evaluation of tissue macromolecular content. From a single protocol this technique can generate quantitative MPF images along with naturally co-registered quantitative images of longitudinal ($R1=1/T1$) and transverse ($R2^*=1/T2^*$) signal relaxation rate constants, and spin density. The SMART technique allows quantitative assessments of central nervous system (CNS) simultaneously using several tissue contrasts.

In the studies reported here, we demonstrate that SMART metrics in brain normal-appearing GM and WM detect damage that correlates with neurological impairment, with MS relapsing versus progressive clinical subtypes. The strongest correlations with clinical tests are with the MPF metric, which reflects tissue myelin content.

4.2. Materials and methods:

4.2.1 Subjects

Thirty-three people with MS (pwMS) with relapsing remitting (RRMS, n=11), and progressive (n=22) MS clinical courses were enrolled, after providing informed consent. Progressive subjects were selected to be progressing in absence of inflammatory disease activity. SPMS patients with superimposed relapses or gadolinium-enhancing lesions within 24 months of entry were excluded. All studies were approved by the Washington University Institutional Review Board.

4.2.2 Clinical testing

The Expanded Disability Status Scale (EDSS) and the MS Functional Composite (MSFC) along with its component 25-foot timed walk (25FTW) assessment of gait, nine-hole peg test (9HPT) assessment of upper extremity function, and paced auditory serial addition test (PASAT) assessment of cognitive function were performed on the day of the MRI by examiners blinded to imaging results. Symbol digit modalities test (SDMT) was also performed. For analyses, the 25FTW and 9HPT were converted to Z scores according to the following equations (3.1) and (3.2) from the MSFC Manual [8]:

4.2.3 Image Acquisition

MRI data were collected using a 3T Trio MRI scanner (Siemens, Erlangen, Germany) equipped with a 32-channel phased-array head coil. SMART data of voxel size 1x1x1 mm^3 were acquired using three dimensional multi-gradient-echo sequences with five flip angles α (5°, 10°, 20°, 40°, 60°) and three gradient echoes (echo times 2.3, 6.2, 10.1ms) for each α. GRAPPA algorithm [102] with an acceleration factor of two and 24 auto-calibrating lines in each phase encoding direction was used. The scan time for SMART data was 13 minutes 40 seconds (2 minutes 44 seconds per flip angle). A phase-based B1 mapping technique accounting for the effects of imperfect RF spoiling and magnetization relaxation was implemented [67]. The scan time for B1 mapping was

2 minutes. Standard clinical MPRAGE [87] images with voxel size: $1 \times 1 \times 1$ mm^3 were collected for segmentation purposes. FLAIR sequence with voxel size of $1 \times 1 \times 3$ mm^3 was used for outlining WM lesions.

4.2.4 Image processing and segmentation

The multi-channel MRI data were combined using a previously published algorithm [51]. The combined data were then analyzed voxel-by-voxel using the SMART model, which generalized the classical Ernst model by taking into account cross-relaxation effects between "free" and "bound" (attached to macromolecules) water pools. The SMART model was described in detail in chapter 2.

Brain GM and WM segmentation was performed on MPRAGE images using FreeSurfer 5.3.0 (Martinos Center for Biomedical Imaging, MGH/HST, US) with visual inspection of each segmented region of interest (ROI) for accuracy. Sixty-eight cortical GM and 68 corresponding subcortical WM ROIs (34 each per hemisphere) were generated (list of ROIs in Supplementary Table 4.3). Using FSL 5.0.0 software (Analysis Group, FMRIB, Oxford, UK), MPRAGE images were then co-registered with SMART images corresponding to flip angle 20° and TE=2.3 ms (that was also used for co-registration of SMART data with other flip angles). This procedure also co-registered ROIs generated by FreeSurfer to all SMART metrics maps. To minimize partial volume effects, CSF masks were generated using FSL based on the SMART images with flip angle 20° and TE=2.3 ms. Applying regional and CSF masks, SMART metrics for each ROI in NAGM and NAWM were calculated using the median value. Note that we define NAGM and NAWM as tissues outside of focal WM lesions. WM lesion masks were obtained using "lesion-TOADS" tool [90] in Medical Image Processing, Analysis and Visualization (MIPAV) software [91] using both MPRAGE and FLAIR images co-registered with FSL.

4.2.5 Statistical analysis

SMART metrics in cortical NAGM and subcortical NAWM were examined for correlations with EDSS, MSFC (also individually for 25FTW, 9HPT, and PASAT) and SDMT. One progressive MS subject was excluded from analysis due to severe image artifacts. Thus, 21 out of 22 progressive MS subjects were used for subsequent imaging analysis. Statistical program R was used for data analysis, with age and gender as covariates. Spearman rank test was used to compute rho values. False discovery rate was used to adjust for multiple comparisons.

4.3. Results:
4.3.1 Examples of IMAGES and Demographic Data of participants

Examples of axial SMART images corresponding to different SMART metrics, an axial FLAIR image and an axial MPRAGE image for a subject with progressive MS are shown in Figure 4.1. Red arrows indicate regions of reduced MPF in A, suggesting reduced myelin content. Reduction of myelin content is also consistent with reduced signal on $R1$, $R1f$, and MPRAGE images, (seen as hypointense signals of a focal lesion on $R1$, $R1_f$ and MPRAGE images), and hyperintense signals on proton density (S_0) and FLAIR images.
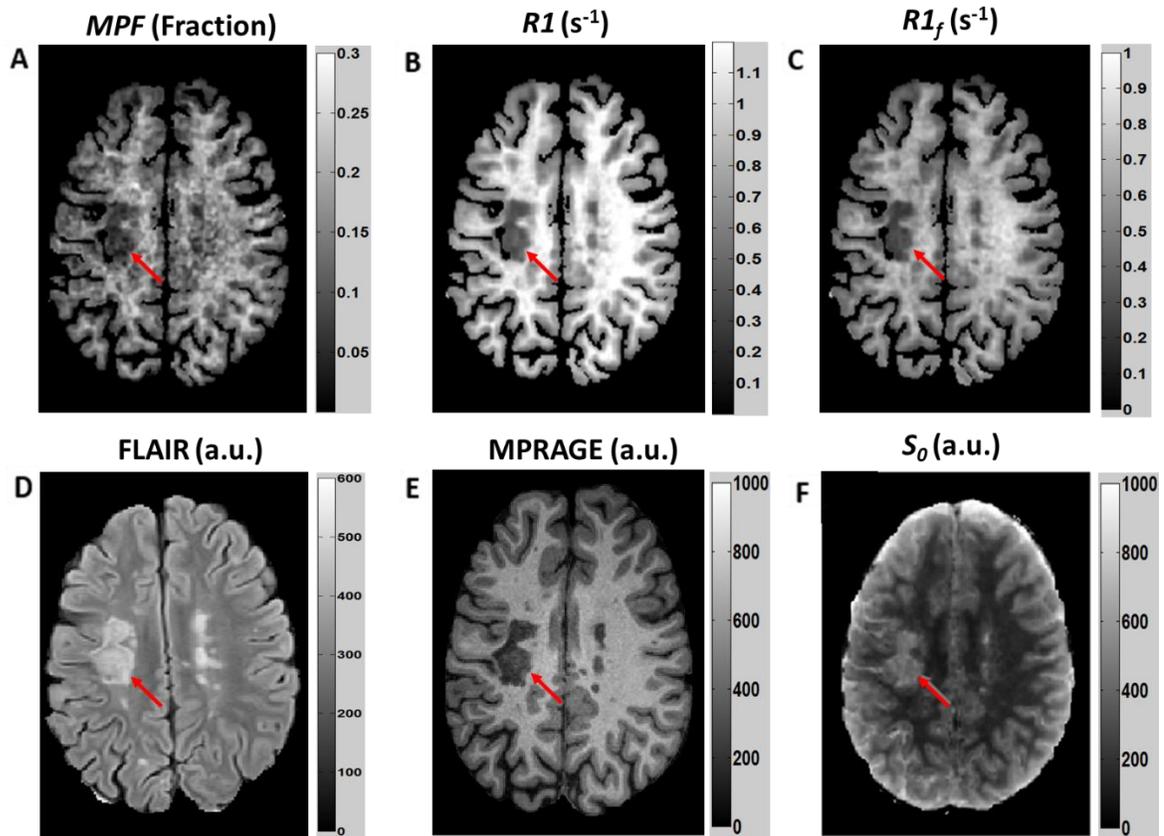
Figure 4.1 Examples of axial SMART metrics images and an axial FLAIR image. MPF [units range from 0 (no bound protons) to 1 (no free water)] (A), $R1$ (1/s) (B), $R1f$ (C), FLAIR (a.u.) (D), MPRAGE (a.u.) (1/s) (E) and S_0 (a.u.) (F) images were obtained from a thirty four year-old man with MS since age 16, now with non-relapsing secondary progressive MS (EDSS 7.5). All images demonstrated gray-white matter contrast. One of a focal lesion is pointed out by a red arrow. MPF images, as well as $R1$, $R1_f$, and MPRAGE images, showed hypointense (reduced) signals at sites of lesions. Proton density (S_0) and FLAIR showed hyperintense signals at sites of lesions. SMART images do not exactly match FLAIR due to different slice thicknesses (1 mm for SMART and 3 mm for FLAIR). a.u. = arbitrary units. Note that the major advantage of SMART is not in detecting

lesions but in quantitative assessment of tissue damage both in lesions and in normal appearing WM and GM.

The demographic and clinical information of subjects in the study revealed lower mean EDSS for the RRMS group than the progressive group, as expected (Table 4.1).

Table 4.1 Demographic and clinical information of pwMS in this study. One RRMS and two progressive MS subjects were left-handed. The rest were right-handed.

		RRMS	Progressive	Normative
Number		11	22	
mean Age ± SD (years)		58.1±6.9	55.3±7.7	
Female/Male		11/0	14/8	
EDSS mean ± SD		2.4±1.1	5.8±1.5	0
25FTW mean ± SD		4.5±0.6	48.5.0±67.6	≤ 5 [103]
9HPT	**Dominan**	22.9±7.7	101.2±219.2	≤ 22 [104]
mean ± SD	**Non-**	22.18±3.7	135.8±261.1	
SDMT mean ± SD		56.5±9.1	44.3±13.3	62.1±10.7[105
3 sec PASAT mean ±		46.8±10.9	43.6±12.6	49.7±9.8[105]

4.3.2 Correlation Between SMART Metrics and Clinical Assessments

SMART MPF measurements of NAGM and NAWM of both hemispheres correlated with most motor related clinical test scores (Table 4.2). MPF measurements in subcortical NAWM demonstrated stronger correlations with clinical test scores than cortical NAGM MPF. In both NAWM and NAGM, MPF metrics of the left hemisphere had stronger correlations with clinical assessments than metrics of the right hemisphere. This was true even for left hemisphere correlations with 9HPT of ipsilateral left hand (Table 4.2, Figure 4.2).

Quantitative *R1* metric showed significant correlation only with the PASAT in NAGM (r= 0.46, p=0.004) and in NAWM (r= 0.38, p=0.025) (Supplementary Table 4.4). $R1_f$ correlated only with 25FTW and 9HPT (r= 0.34, p=0.046; r=0.46, p=0.005, respectively) in the left hemisphere (Supplementary Table 4.5).

	MPF							
	NAGM(left hemisphere)		NAGM(right hemisphere)		NAWM(left hemisphere)		NAWM(right hemisphere)	
	rho	p	rho	p	rho	p	rho	p
EDSS	-0.360	0.009	-0.251	0.070	-0.491	<0.001	-0.314	0.022
25FTW	-0.334	0.015	-0.288	0.034	-0.404	0.003	-0.315	0.022
9HPT(Dom)	0.554	<0.001	0.499	<0.001	0.600	<0.001	0.461	0.001
9HPT(NonDom)	0.521	<0.001	0.439	0.002	0.650	<0.001	0.462	0.001
PASAT(2S)	0.067	0.654	0.086	0.570	0.256	0.068	0.223	0.103
PASAT(3S)	-0.029	0.820	0.033	0.820	0.149	0.309	0.106	0.473
SDMT	0.136	0.366	0.235	0.095	0.313	0.023	0.249	0.071
MSFC	0.398	0.003	0.359	0.009	0.525	<0.001	0.407	0.003

Table 4.2 MPF in the cortical NAGM and subcortical NAWM correlates with clinical assessments**.** MPF measurements in both NAGM and NAWM correlated most with assessments related to motor function, although NAWM MPF had stronger correlations with clinical tests than NAGM MPF. The MPF in left hemisphere demonstrated stronger correlation with clinical scores than did MPF in the right hemisphere. For 9HPT, the three left-handed pwMS were removed from analyses. Spearman rho and p values were computed in R, with age and gender as covariates. All listed p values are after multiple comparison correction using false discovery rate. Statistically significant correlations are highlighted in red.

Since global MPF measurement showed the strongest correlations with clinical tests, MPF was selected for region-wise analysis. Regional MPFs in the left hemisphere showed consistently stronger correlations than MPF in the right hemisphere with MSFC, 9HPT, 25FTW and EDSS (Figures 4.2 and 4.3). Additionally, in most of the ROIs, MPF in NAWM had stronger correlations with clinical test scores than in NAGM.
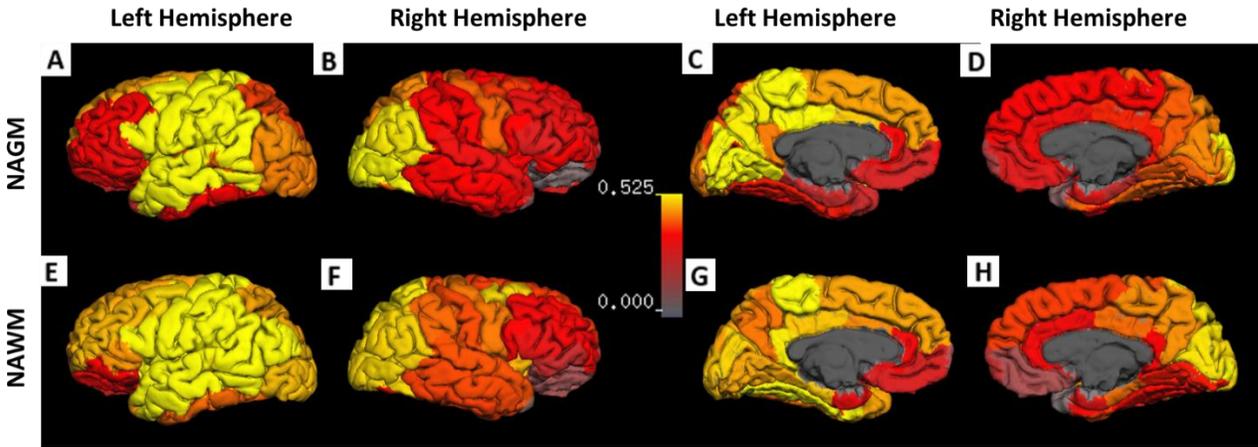
Figure 4.2 MPF correlations with 9-hole peg test. MPF in NAGM (top row) and subcortical NAWM (bottom row) of the dominant left hemisphere correlated better than the right hemisphere with 9-hole peg test results of the non-dominant left hand. Three left-handed subjects were removed from the correlation analysis to ensure all remaining subjects have the same dominant hemisphere. Interestingly, stronger correlations were noted between the left hand 9-HPT results and the ipsilateral MPF in the left hemisphere motor regions than for the same regions in the contralateral right hemisphere. More extensive and stronger correlations were noted for NAWM than NAGM. Color bar: scale of Spearman rho values.
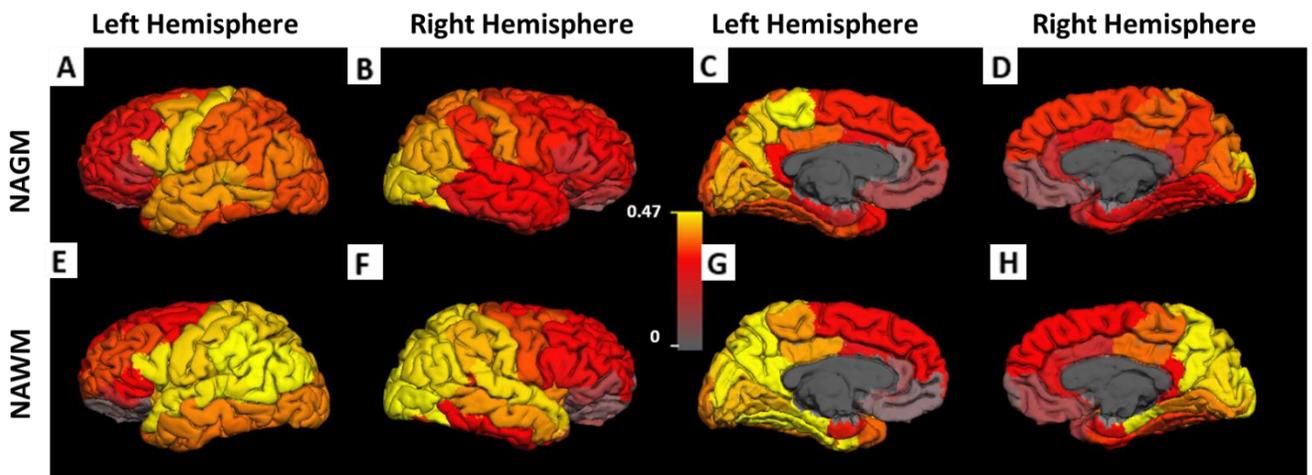
Figure 4.3 Correlations of MPF with MSFC scores. MPF in subcortical NAWM (bottom row) correlated better than subcortical NAGM (top row) with MSFC. All pwMS were included in this correlation analysis. No clear differences between hemispheres were noted. Color bar: scale of Spearman rho values.

MPF in both left and right hemispheres of NAGM and NAWM differentiated relapsing-remitting from non-relapsing progressive cohorts at the group level, although there was considerable overlap of individual subjects between the two clinical subgroups (Fig. 4.4). In particular, MPF of subcortical NAWM in left hemisphere showed the best ability to distinguish the two cohorts at the group level.

4.3.3 Distinguishing Progressive MS from RRMS by SMART Metrics
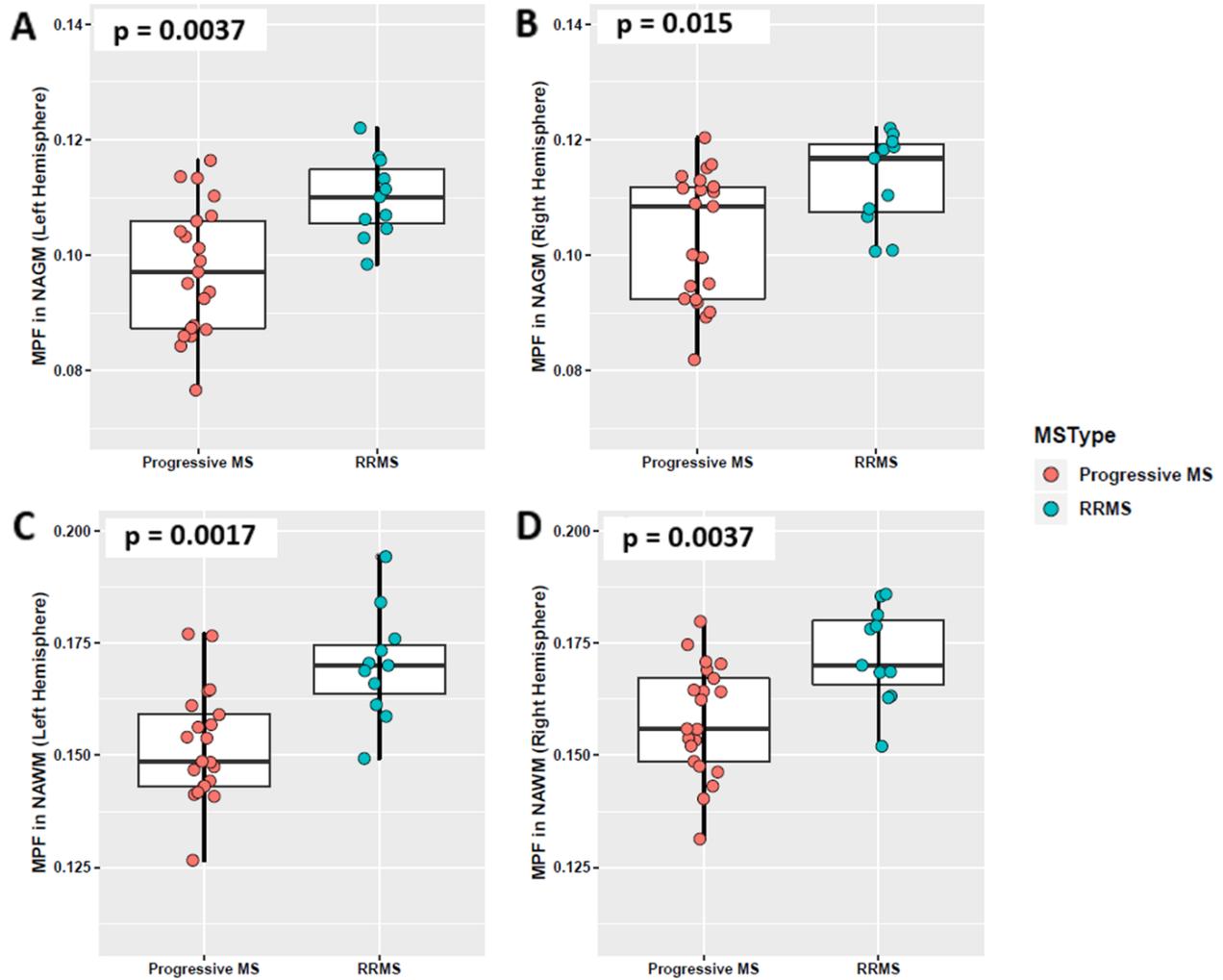
Figure 4.4 Group comparisons based on MPF measurement in cortical NAGM of left (A) and right (B) hemispheres, and left (C) and right (D) hemispheres of subcortical NAWM revealed higher MPF in the RRMS than progressive MS group. In both GM and WM, MPF measurements of the left hemisphere differentiated the two MS subtypes better than MPF of right hemisphere. Boxes represent the interquartile ranges; the horizontal lines within the boxes are median values, points are median values of individual subjects. p values were determined after adjusting for multiple comparisons using false discovery rate and adjusting for age.
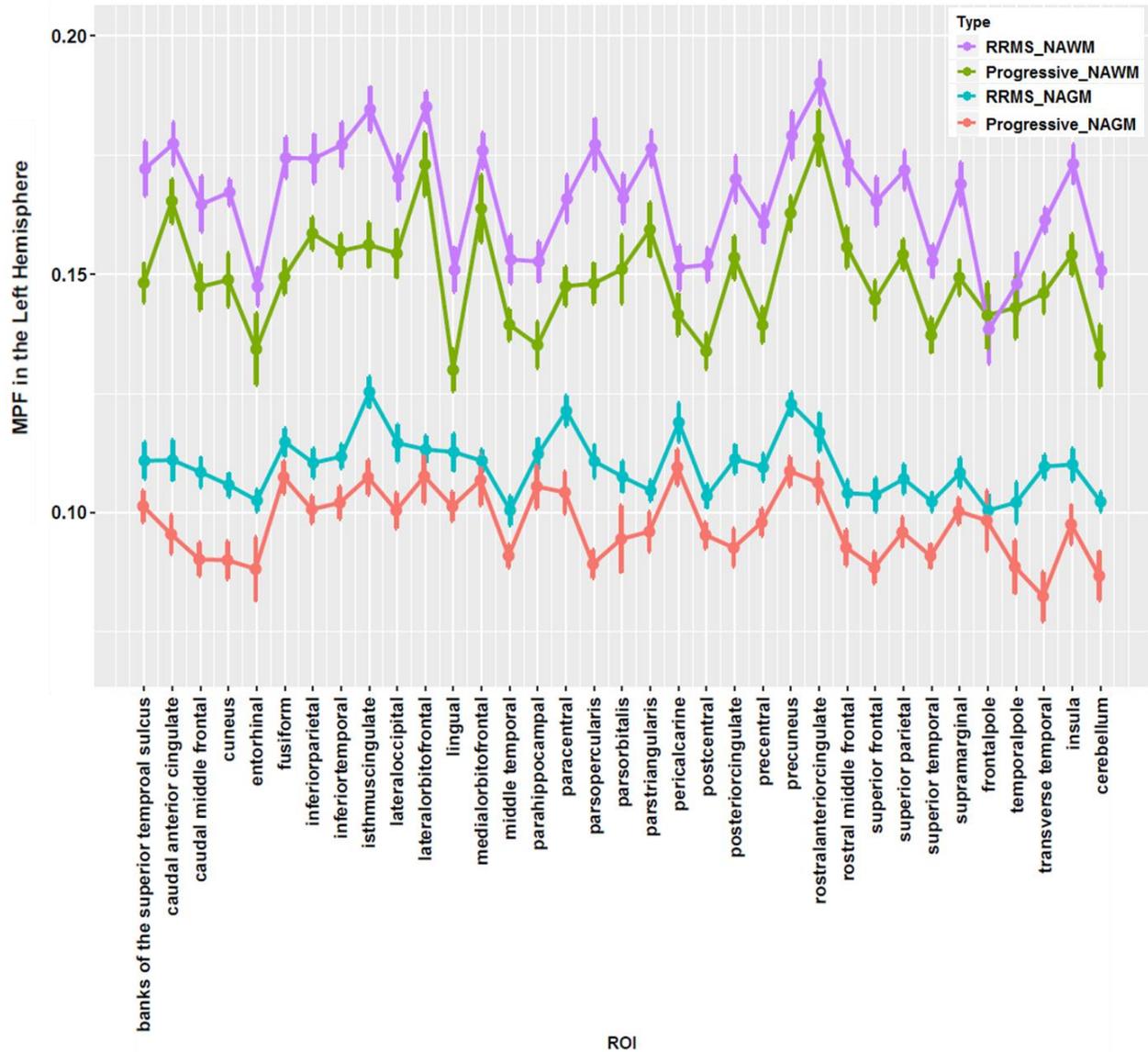
Figure 4.5 Regional MPF of the left hemisphere is higher in RRMS than progressive MS cohorts in cortical NAGM and subcortical NAWM. Median values of MPF measurement of each cortical/subcortical ROI in the left hemisphere for each clinical subtype are plotted. Error bars are the standard error of MPF measurement. MPF in NAWM ROIs were significantly higher than MPF in NAGM, consistent with the greater myelin content of WM.

In agreement with higher concentration of myelin in WM as compared to GM, region-wise analysis showed that MPF measurements in subcortical NAWM were universally higher than in cortical NAGM, as shown for the left hemisphere in Figure 4.5. Similar results were found in the right hemisphere. (Supplementary Figure 4.6). The RRMS cohort had higher MPF measurements than the progressive MS cohort, in both NAGM and NAWM, consistent with greater myelin loss in the progressive group.

4.4. Discussion:

Imaging biomarkers of tissue damage and repair are needed to facilitate the search for effective treatments for MS at different stages. Although quantitative MRI [MT, MR relaxometry (*T1, T2, T2**) and diffusion] have been widely used to assess CNS tissue damage in MS, they have not gained traction in clinical practice, prompting searches for novel, more pathologically specific and efficient approaches. In this study, we applied the newly developed SMART MRI technique for in vivo evaluation of myelin damage in brains of people with MS. The SMART technique generates naturally co-registered multi-contrast quantitative data for several MR parameters (SMART metrics). Importantly, SMART MRI metrics allow assessment of the exchange between "free" and "bound" water compartments by measuring MPF, thus allowing estimation of brain tissue macromolecular content similar to quantitative MT. Compared with standard *T1W* and *T2W* imaging and MTR, SMART MRI metrics provide quantitative information on brain tissue damage not only in MS lesions but also in normal-appearing WM and GM, which is not readily visible on standard clinical MRI. Notably, an advantage of the SMART technique is that it does not apply either MT or 180° radiofrequency pulses, which means it avoids high energy deposition on patients, making it safe at high field MRI.

The multi-contrast battery of naturally co-registered SMART images/metrics includes measurements of MPF, cross-relaxation-affected *T1* and spin density of free water. In this paper we presented results of high resolution (1x1x1 mm^3) SMART protocol that required about 16 minutes of MRI time. This time can be significantly reduced by selecting different image resolutions. For example, for 1x1x2 mm^3 image (often used in clinical settings) the protocol would require less than 9 minutes, still producing the whole battery of SMART images.

4.4.1 SMART Metrics Showed Strong Correlation with Patients' Clinical Scores

In this study we asked if the novel imaging method, SMART MRI, could detect and quantify brain tissue damage, in particular myelin damage, in pwMS and whether this might correlate with clinical test results or clinical subtypes (RRMS versus progressive). To address these questions, brain tissue was segmented into normal-appearing tissue (NAGM and subcortical NAWM) and focal lesions visible on standard clinical images and assessed by SMART MRI. The left and the right hemispheres were analyzed separately to explore differences in the two sides, yielding interesting stronger associations of the dominant hemisphere with both contralateral and ipsilateral motor functions.

MPF derived using SMART MRI of the brain showed significant correlations with motor-related clinical test scores at a global and regional level. MPF in NAWM was higher than in NAGM, consistent with the notion that protons bound to macromolecules are more abundant in highly myelinated regions. *R1* and *R1$_f$* showed modest but significant correlation with PASAT and motor-related tests, respectively. We found lower MPF and *R1 (1/T1)* signals in MS lesions than in normal appearing tissues, in agreement with previous reports of hypointense MPF [30, 106] and *T1* [107] signals in demyelinated and dysmyelinated CNS tissue. The values of MPF and *R1* we observed in this study were in general agreement with published studies [108, 109].

4.4.2 MPF Distinguishes Progressive MS from RRMS

In clinical practice, progressive MS subtypes (secondary progressive (SP) MS and primary progressive (PP) MS) present a major treatment challenge, compared with the RRMS subtype. Few disease-modifying therapies have been effective for progressive MS. The reason for this may be related to the less inflammatory pathophysiology of progressive MS [7, 110] that is not detected well using conventional imaging techniques. Suitable imaging surrogates of progression are lacking as outcome measures for trials and thus, a new noninvasive imaging technique that can sensitively and reproducibly measure CNS tissue changes due to progressive MS is very much needed [111]. In this study, progressive MS subjects were specifically selected to be progressing in absence of inflammatory disease activity (superimposed relapses or gadolinium-enhancing lesions) within the prior 2 or more years. This non-inflammatory progressive MS cohort was distinguishable from the RRMS group using SMART metrics.

Previous studies have shown MPF measurements to be highly correlated with myelin content [34, 35]. One clear finding from this our study was that MPF in NAGM was universally lower than in NAWM, which likely reflects the lower myelin content of GM than WM. MPF measurement differentiated the RRMS group from the progressive MS group, with RRMS consistently showing higher MPF values in almost all ROIs. For both global (entire cerebral cortical NAGM and subcortical NAWM) and regional-wise measurements, MPF in NAWM distinguished the RRMS from the progressive MS cohort best among the SMART metrics. This result is in agreement with published pathology studies showing greater myelin loss in progressive than RRMS patients [110, 112] and suggests that SMART MPF could be useful as an outcome measure in trials of remyelinating agents.

Improved and quantitative imaging biomarkers are greatly needed in the MS field [111]. Specifically needed are methods to readily assess cortical gray matter damage, to measure repair/remyelination in clinical trials of putative reparative treatments, and to detect progression unrelated to overt inflammation as an outcome measure in trials of disease-modifying therapies for progressive disease. Our results using the SMART MRI metrics suggest it to be a safe, rapid and accurate imaging technique that holds promise as a needed biomarker to detect unseen cortical (and WM) damage. Moreover, it holds promise to provide an estimation of myelin content that could be useful for trials of remyelinating therapies. SMART metrics distinguished RRMS from progressive patients at the group level, and longitudinal studies with larger cohorts are underway to evaluate whether the SMART metrics might serve as a surrogate of MS disease progression.

The battery of SMART images allows simultaneous assessment of tissue damage from different perspectives. In this paper we assessed tissue damage using SMART metrics independently, finding that some metrics correlate better than others with different clinical tests and MS subtypes. To take full advantage of the whole battery of SMART metrics, our future work will encompass building models that would include all SMART metrics for better and more specific assessment of tissue pathology.

4.5. Conclusions

SMART MPF showed significant correlations with clinical motor assessments in pwMS, and distinguished RRMS from progressive MS subtypes at a group level. In particular, SMART allows evaluation of tissue macromolecular content (MPF metric) with higher resolution and lower RF energy deposition compared to existing qMT approaches, thus offering an improved method of assessing myelin integrity in MS. These findings indicate the high potential of SMART MRI technique for MS diagnostics and clinical monitoring and as an outcome measure in clinical trials.

4.6 Supplementary Information:
Table 4.3. List of Regions of Interest (ROIs)

	ROI in cortical gray matter	ROI in subcortical white matter
1	cortex-banks of the superior temporal sulcus	WM-banks of the superior temporal sulcus
2	cortex-caudal anterior cingulate	WM-caudal anterior cingulate
3	cortex-caudal middle frontal	WM-caudal middle frontal
4	cortex-cuneus	WM-cuneus
5	cortex-entorhinal	WM-entorhinal
6	cortex-frontal pole	WM-frontal pole
7	cortex-fusiform	WM-fusiform
8	cortex-inferior parietal	WM-inferior parietal
9	cortex-inferior temporal	WM-inferior temporal
10	cortex-insula	WM-insula
11	cortex-isthmus of the cingulate	WM-isthmus of cingulate
12	cortex-lateral occipital	WM-lateral occipital
13	cortex-lateral orbitofrontal	WM-lateral orbitofrontal
14	cortex-lingual	WM-lingual
15	cortex-medial orbitofrontal	WM-medial orbitofrontal
16	cortex-middle temporal	WM-middle temporal
17	cortex-parahippocampal	WM-parahippocampal
18	cortex-paracentral	WM-paracentral

19	cortex-parsopercularis	WM-parsopercularis
20	cortex-parsorbitalis	WM-parsorbitalis
21	cortex-parstriangularis	WM-parstriangularis
22	cortex-pericalcarine	WM-pericalcarine
23	cortex-postcentral	WM-postcentral
24	cortex-posterior cingulate	WM-posterior cingulate
25	cortex-precentral	WM-precentral
26	cortex-precuneus	WM-precuneus
27	cortex-rostral anterior cingulate	WM-rostral anterior cingulate
28	cortex-rostral middle frontal	WM-rostral middle frontal
29	cortex-superior frontal	WM-superior frontal
30	cortex-superior parietal	WM-superior parietal
31	cortex-superior temporal	WM-superior temporal
32	cortex-supramarginal	WM-supramarginal
33	cortex-temporal pole	WM-temporal pole
34	cortex-transverse temporal	WM-transverse temporal
35	cortex-cerebellum	WM-cerebellum

Table 4.4 Global *R1* measurements in cortical GM and subcortical WM showed few correlations with clinical assessments. The only significant correlations for *R1* measurements were with the two second PASAT, a test of cognitive function test. For 9HPT, three left-handed subjects were removed to ensure all test subjects were right handed. Spearman rho and p values were computed in R, with age and gender as covariates. All listed p values are after multiple

comparison correction using false discovery rate. Statistically significant correlations are highlighted in red.

	R1							
	NAGM(left hemisphere)		NAGM(right hemisphere)		NAWM(left hemisphere)		NAWM(right hemisphere)	
	rho	p	rho	p	rho	p	rho	p
EDSS	-0.095	0.667	-0.146	0.475	-0.132	0.514	-0.089	0.673
25FTW	0.131	0.514	0.049	0.765	-0.044	0.765	-0.049	0.765
9HPT(Dom)	0.048	0.765	0.176	0.419	0.101	0.665	0.227	0.281
9HPT(NonDom	-0.027	0.844	0.043	0.765	0.044	0.765	0.087	0.681
PASAT(2S)	0.461	0.004	0.411	0.013	0.337	0.054	0.375	0.025
PASAT(3S)	0.267	0.157	0.210	0.281	0.276	0.144	0.327	0.054
SDMT	0.045	0.765	0.163	0.419	0.156	0.419	0.243	0.196
MSFC	0.113	0.601	0.214	0.281	0.158	0.419	0.190	0.354

Table 4.5. Global $R1_f$ measurements in cortical NAGM and subcortical NAWM of left and right hemispheres showed significant correlations of left hemisphere NAGM with 25FTW and 9HPT. NAWM of the left hemisphere correlated modestly with non-dominant hand 9HPT test results. For 9HPT, three left-handed subjects were removed to ensure all remaining subjects have the same dominant hemisphere. Spearman rho and p values were computed in R, with age and gender as covariates. All listed p values are after multiple comparison correction using false discovery rate. Statistically significant correlations are highlighted in red.

	$R1_f$							
	NAGM(left hemisphere)		NAGM(right hemisphere)		NAWM(left hemisphere)		NAWM(right hemisphere)	
	rho	p	rho	p	rho	p	rho	p
EDSS	0.265	0.122	0.176	0.246	0.179	0.246	0.104	0.476
25FTW	0.344	0.046	0.290	0.122	0.188	0.246	0.161	0.288
9HPT(Dom)	-0.462	0.005	-0.263	0.144	-0.293	0.122	-0.152	0.321
9HPT(NonDom)	-0.461	0.005	-0.287	0.122	-0.369	0.046	-0.217	0.211
PASAT(2S)	0.211	0.200	0.201	0.211	0.224	0.178	0.240	0.155
PASAT(3S)	0.179	0.246	0.176	0.246	0.222	0.178	0.261	0.122
SDMT	-0.048	0.735	0.065	0.627	0.060	0.643	0.127	0.377
MSFC	-0.265	0.122	-0.148	0.321	-0.155	0.304	-0.077	0.606
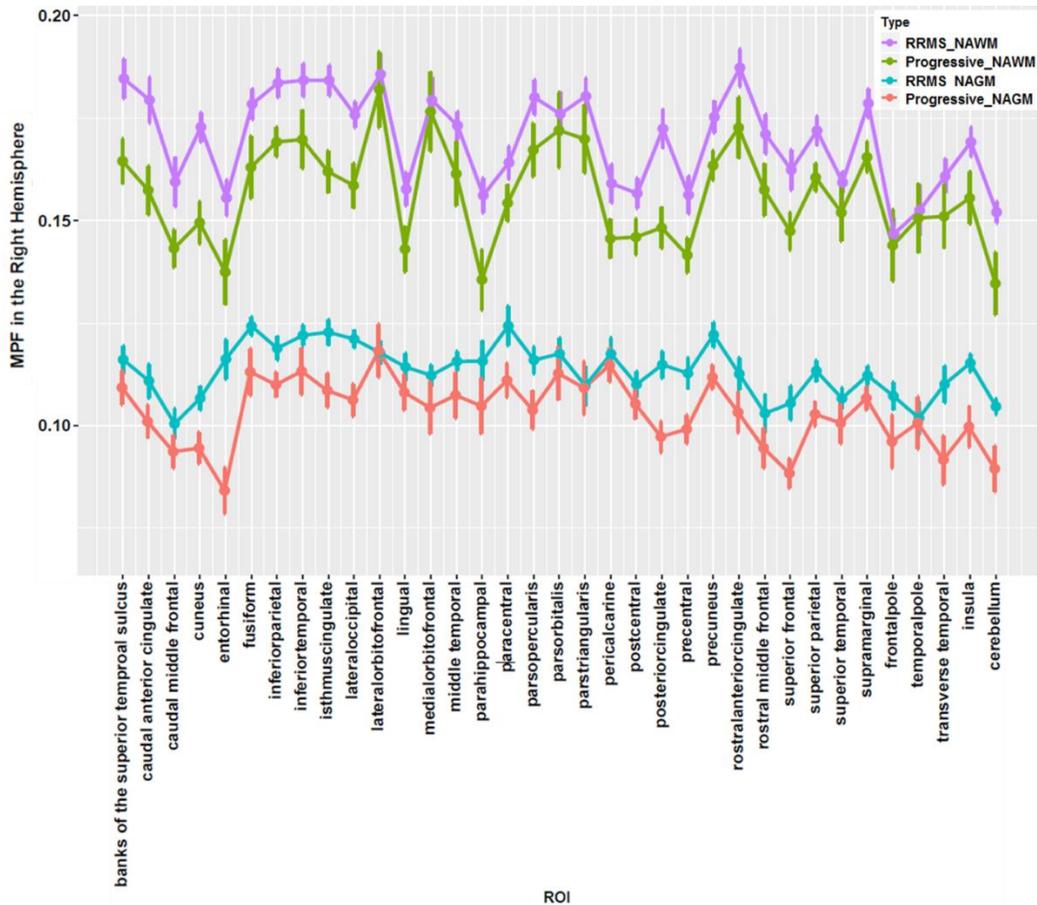
Figure 4.6. Regional MPF of the right hemisphere is higher in RRMS than progressive MS cohorts in cortical NAGM and subcortical NAWM. Median values of MPF measurement of each cortical/subcortical ROI in the right hemisphere for each clinical subtype are plotted. Error bars are the standard error of MPF measurement. MPF in NAWM ROIs were significantly higher than MPF in NAGM, consistent with the greater myelin content of WM.

Chapter 5: Future Plan

In this study, two novel GRE based MRI techniques, GEPCI and SMART, have been used to quantitatively study MS tissue damage. For the GEPCI technique, our results show moderate to strong correlations between cervical spinal cord size and GM $R2t^*$ values and thickness of several brain cortical regions. This finding supports the well-known idea that MS is a global CNS disease, affecting both spinal cord and brain. Cervical cord CSA correlated better with physical impairment status, compared with $R2t^*$ and thickness of brain cortex. Spinal cord size, thickness and $\Delta R2t^*$ values of the cortex all differentiated MS patients from healthy controls. Additionally, upper cervical cord size and GM thickness demonstrated significant differences between MS clinical subtypes.

For the SMART technique, our results showed that MPF can distinguish non-relapsing progressive MS from RRMS and to examine correlations with clinical assessments. Without applying either MT or 180° radiofrequency pulses, SMART MRI generates high resolution quantitative images with various contrasts, and is safe for high-field MRI, making it a useful outcome measure in clinical trials.

Of course, there are much more in the GEPCI and SMART techniques that one can carry on investigating.

1) In the future, the GEPCI and SMART techniques should be applied to a large cohort of MS patients at different disease stages. This will give us stronger statistical power to support our preliminary results.

2) As a CNS disease, MS can affect brain, cerebellum, brain stem, spinal cord. Currently, the GEPCI and SMART techniques focus on tissue damage in brain. Future work should include other regions of the CNS. To achieve this goal, the GEPCI and SMART pulse sequence would have to be modified to overcome technical issues such motion and magnetic field inhomogeneity.

3) In chapter 3, our results showed that the spinal cord size had significant correlation with MS patients' clinical assessments. Other volumetric measurements such as brain volume should be included in future data analysis.

3) In both GEPCI and SMART projects, the central vein sign in active MS lesions has not been explored. In recent years, many studies have showed that the presence of central vein could distinguish MS from other neurological diseases [113]. Future work will explore the possibility to detect central vein in MS lesions using our GEPCI and SMART images.

4) Myelin damage is the hallmark of MS pathology. The myelin structure can be divided into several compartments. Each of them has unique MR signal decay properties. Therefore, it is important to incorporate the multi-compartments structures into the GEPCI and SMART models.

5) In this study, the severity of tissue damage in MS lesions has been quantified using the GEPCI and SMART techniques. However, other factors such as the locations of lesions play an important role in explaining patients' clinical symptoms and signs. Future work should consider these important factors while evaluating tissue damage in MS lesions.

6) Histopathological studies should be performed in the future to further validate the candidacies of GEPCI and SMART as biomarkers for MS tissue damage.

References

1. Price, W.S., *Spin Dynamics: Basics of Nuclear Magnetic Resonance, 2nd edition.* Concepts in Magnetic Resonance Part A, 2009. **34A**(1): p. 60-61.
2. Bernstein, M.A., K.F. King, and Z.J. Zhou, *Handbook of MRI pulse sequences*. 2004, Amsterdam ; Boston: Academic Press. xxii,1017 p.
3. Browne, P., et al., *Atlas of Multiple Sclerosis 2013: A growing global problem with widespread inequity.* Neurology, 2014. **83**(11): p. 1022-4.
4. Wallin, M.T., et al., *The prevalence of MS in the United States: A population-based estimate using health claims data.* Neurology, 2019. **92**(10): p. e1029-e1040.
5. Minagar, A., et al., *Multiple sclerosis as a vascular disease.* Neurol Res, 2006. **28**(3): p. 230-235.
6. Compston, A. and A. Coles, *Multiple sclerosis.* The Lancet, 2008. **372**(9648): p. 1502-1517.
7. Lassmann, H., J. van Horssen, and D. Mahad, *Progressive multiple sclerosis: pathology and pathogenesis.* Nature Reviews Neurology, 2012. **8**: p. 647.
8. Fischer, J.S., et al., *The Multiple Sclerosis Functional Composite Measure (MSFC): an integrated approach to MS clinical outcome assessment. National MS Society Clinical Outcomes Assessment Task Force.* Mult Scler, 1999. **5**(4): p. 244-50.
9. Brownlee, W.J., *Misdiagnosis of multiple sclerosis: If you have a hammer, everything looks like a nail?* Neurology, 2019. **92**(1): p. 15-16.
10. Kaisey, M., et al., *Incidence of multiple sclerosis misdiagnosis in referrals to two academic centers.* Mult Scler Relat Disord, 2019. **30**: p. 51-56.
11. Solomon, A., et al., *The spectrum of multiple sclerosis misdiagnosis in the era of McDonald criteria: A multicenter study (PL01.003).* Neurology, 2016. **86**(16 Supplement): p. PL01.003.
12. McDonald, W.I., et al., *Recommended diagnostic criteria for multiple sclerosis: guidelines from the International Panel on the diagnosis of multiple sclerosis.* Ann Neurol, 2001. **50**(1): p. 121-7.
13. Dalton, C.M., et al., *New T2 lesions enable an earlier diagnosis of multiple sclerosis in clinically isolated syndromes.* Ann Neurol, 2003. **53**(5): p. 673-6.
14. Wayne Moore, G.R., *MRI-clinical correlations: more than inflammation alone-what can MRI contribute to improve the understanding of pathological processes in MS?* J Neurol Sci, 2003. **206**(2): p. 175-179.
15. Brex, P.A., et al., *A longitudinal study of abnormalities on MRI and disability from multiple sclerosis.* N Engl J Med, 2002. **346**(3): p. 158-64.
16. McFarland, H.F., et al., *The role of MRI as a surrogate outcome measure in multiple sclerosis.* Multiple Sclerosis Journal, 2002. **8**(1): p. 40-51.
17. Waldman, A., et al., *MRI of the brain with ultra-short echo-time pulse sequences.* Neuroradiology, 2003. **45**(12): p. 887-92.
18. Horch, R.A., J.C. Gore, and M.D. Does, *Origins of the ultrashort-T2 1H NMR signals in myelinated nerve: a direct measure of myelin content?* Magn Reson Med, 2011. **66**(1): p. 24-31.
19. MacKay, A., et al., *In vivo visualization of myelin water in brain by magnetic resonance.* Magn Reson Med, 1994. **31**(6): p. 673-7.
20. Laule, C., et al., *Myelin water imaging in multiple sclerosis: quantitative correlations with histopathology.* Mult Scler, 2006. **12**(6): p. 747-53.
21. Laule, C., et al., *Myelin water imaging of multiple sclerosis at 7 T: correlations with histopathology.* Neuroimage, 2008. **40**(4): p. 1575-80.
22. Alonso-Ortiz, E., I.R. Levesque, and G.B. Pike, *MRI-based myelin water imaging: A technical review.* Magn Reson Med, 2015. **73**(1): p. 70-81.

23. Prasloski, T., et al., *Rapid whole cerebrum myelin water imaging using a 3D GRASE sequence.* Neuroimage, 2012. **63**(1): p. 533-9.

24. Oh, J., et al., *Measurement of in vivo multi-component T2 relaxation times for brain tissue using multi-slice T2 prep at 1.5 and 3 T.* Magn Reson Imaging, 2006. **24**(1): p. 33-43.

25. Hwang, D., D.-H. Kim, and Y.P. Du, *In vivo multi-slice mapping of myelin water content using T2* decay.* Neuroimage, 2010. **52**(1): p. 198-204.

26. Deoni, S.C., et al., *Gleaning multicomponent T1 and T2 information from steady-state imaging data.* Magn Reson Med, 2008. **60**(6): p. 1372-87.

27. Vidarsson, L., et al., *Echo time optimization for linear combination myelin imaging.* Magn Reson Med, 2005. **53**(2): p. 398-407.

28. Horsfield, M.A., *Magnetization Transfer Imaging in Multiple Sclerosis.* Journal of Neuroimaging, 2005. **15**(s4): p. 58S-67S.

29. Filippi, M. and F. Agosta, *Magnetization transfer MRI in multiple sclerosis.* J Neuroimaging, 2007. **17 Suppl 1**: p. 22S-26S.

30. Yarnykh, V.L., et al., *Fast Whole-Brain Three-dimensional Macromolecular Proton Fraction Mapping in Multiple Sclerosis.* Radiology, 2015. **274**(1): p. 210-220.

31. Sled, J.G. and G.B. Pike, *Quantitative imaging of magnetization transfer exchange and relaxation properties in vivo using MRI.* Magn Reson Med, 2001. **46**(5): p. 923-31.

32. van Gelderen, P., X. Jiang, and J.H. Duyn, *Rapid measurement of brain macromolecular proton fraction with transient saturation transfer MRI.* Magn Reson Med, 2017. **77**(6): p. 2174-2185.

33. Stanisz, G.J., et al., *T1, T2 relaxation and magnetization transfer in tissue at 3T.* Magnetic Resonance in Medicine, 2005. **54**(3): p. 507-512.

34. Schmierer, K., et al., *Quantitative magnetization transfer imaging in postmortem multiple sclerosis brain.* J Magn Reson Imaging, 2007. **26**(1): p. 41-51.

35. Underhill, H.R., et al., *Fast bound pool fraction imaging of the in vivo rat brain: association with myelin content and validation in the C6 glioma model.* Neuroimage, 2011. **54**(3): p. 2052-65.

36. Le Bihan, D., et al., *Diffusion tensor imaging: concepts and applications.* J Magn Reson Imaging, 2001. **13**(4): p. 534-46.

37. Aung, W.Y., S. Mar, and T.L. Benzinger, *Diffusion tensor MRI as a biomarker in axonal and myelin damage.* Imaging in medicine, 2013. **5**(5): p. 427-440.

38. Sun, S.W., et al., *Differential sensitivity of in vivo and ex vivo diffusion tensor imaging to evolving optic nerve injury in mice with retinal ischemia.* Neuroimage, 2006. **32**(3): p. 1195-204.

39. Schmierer, K., et al., *Quantitative magnetic resonance of postmortem multiple sclerosis brain before and after fixation.* Magnetic Resonance in Medicine, 2008. **59**(2): p. 268-277.

40. Klawiter, E.C., et al., *Radial diffusivity predicts demyelination in ex vivo multiple sclerosis spinal cords.* Neuroimage, 2011. **55**(4): p. 1454-60.

41. Kern, K.C., et al., *Corpus callosal diffusivity predicts motor impairment in relapsing-remitting multiple sclerosis: a TBSS and tractography study.* Neuroimage, 2011. **55**(3): p. 1169-77.

42. Kucharczyk, W., et al., *Relaxivity and magnetization transfer of white matter lipids at MR imaging: importance of cerebrosides and pH.* Radiology, 1994. **192**(2): p. 521-529.

43. O'Brien, J.S. and E.L. Sampson, *Lipid composition of the normal human brain: gray matter, white matter, and myelin.* Journal of Lipid Research, 1965. **6**(4): p. 537-544.

44. Hills, B.P., S.F. Takacs, and P.S. Belton, *The effects of proteins on the proton N.M.R. transverse relaxation time of water.* Molecular Physics, 1989. **67**(4): p. 919-937.

45. Hills, B.P., K.M. Wright, and P.S. Belton, *Proton N.M.R. studies of chemical and diffusive exchange in carbohydrate systems.* Molecular Physics, 1989. **67**(6): p. 1309-1326.

46. Yablonskiy, D.A., *Quntitative T2 contrast with Gradient Echoes*, in *8th Annual Meeting of the International Society for Magnetic Resonance in Medicine*. 2000: Denver, Colorado.

47.   Luo, J., et al., *Gradient Echo Plural Contrast Imaging - Signal model and derived contrasts: T2*, T1, Phase, SWI, T1f, FST2*and T2*-SWI.* Neuroimage, 2012. **60**(2): p. 1073-82.

48.   Yablonskiy, D.A., et al., *Voxel spread function method for correction of magnetic field inhomogeneity effects in quantitative gradient-echo-based MRI.* Magn Reson Med, 2013. **70**(5): p. 1283-92.

49.   Wen, J., A.H. Cross, and D.A. Yablonskiy, *On the role of physiological fluctuations in quantitative gradient echo MRI: implications for GEPCI, QSM, and SWI.* Magn Reson Med, 2014.

50.   Ulrich, X. and D.A. Yablonskiy, *Separation of cellular and BOLD contributions to T2* signal relaxation.* Magn Reson Med, 2015.

51.   Luo, J., et al., *Gradient echo plural contrast imaging--signal model and derived contrasts: T2*, T1, phase, SWI, T1f, FST2*and T2*-SWI.* Neuroimage, 2012. **60**(2): p. 1073-82.

52.   Quirk, J.D., et al., *Optimal decay rate constant estimates from phased array data utilizing joint Bayesian analysis.* J Magn Reson, 2009. **198**(1): p. 49-56.

53.   Ogawa, S., et al., *Brain magnetic resonance imaging with contrast dependent on blood oxygenation.* Proc Natl Acad Sci U S A, 1990. **87**(24): p. 9868-72.

54.   Yablonskiy, D.A. and E.M. Haacke, *Theory of NMR signal behavior in magnetically inhomogeneous tissues: the static dephasing regime.* Magn Reson Med, 1994. **32**(6): p. 749-63.

55.   Yablonskiy, D.A., *Quantitation of intrinsic magnetic susceptibility-related effects in a tissue matrix. Phantom study.* Magnetic Resonance in Medicine, 1998. **39**(3): p. 417-428.

56.   Spees, W.M., et al., *Water proton MR properties of human blood at 1.5 Tesla: magnetic susceptibility, T(1), T(2), T*(2), and non-Lorentzian signal behavior.* Magn Reson Med, 2001. **45**(4): p. 533-42.

57.   He, X., M. Zhu, and D.A. Yablonskiy, *Validation of oxygen extraction fraction measurement by qBOLD technique.* Magn Reson Med, 2008. **60**(4): p. 882-8.

58.   Dickson, J.D., et al., *Quantitative phenomenological model of the BOLD contrast mechanism.* J Magn Reson, 2011. **212**(1): p. 17-25.

59.   Wang, X., A.L. Sukstanskii, and D.A. Yablonskiy, *Optimization strategies for evaluation of brain hemodynamic parameters with qBOLD technique.* Magn Reson Med, 2013. **69**(4): p. 1034-43.

60.   Zhao, Y., et al., *On the relationship between cellular and hemodynamic properties of the human brain cortex throughout adult lifespan.* Neuroimage, 2016. **133**: p. 417-29.

61.   Yablonskiy, D.A., A.L. Sukstanskii, and X. He, *Blood oxygenation level-dependent (BOLD)-based techniques for the quantification of brain hemodynamic and metabolic properties - theoretical models and experimental approaches.* NMR Biomed, 2013. **26**(8): p. 963-86.

62.   Sukstanskii, A.L., et al., *Simultaneous multi-angular relaxometry of tissue with MRI (SMART MRI): Theoretical background and proof of concept.* Magn Reson Med, 2016.

63.   Yarnykh, V.L., *Actual flip-angle imaging in the pulsed steady state: A method for rapid three-dimensional mapping of the transmitted radiofrequency field.* Magnetic Resonance in Medicine, 2007. **57**(1): p. 192-200.

64.   Insko, E.K. and L. Bolinger, *Mapping of the Radiofrequency Field.* Journal of Magnetic Resonance, Series A, 1993. **103**(1): p. 82-85.

65.   Chang, Y.V., *Rapid B1 mapping using orthogonal, equal-amplitude radio-frequency pulses.* Magnetic Resonance in Medicine, 2012. **67**(3): p. 718-723.

66.   Oh, C.H., et al., *Radio frequency field intensity mapping using a composite spin-echo sequence.* Magn Reson Imaging, 1990. **8**(1): p. 21-25.

67.   Wen, J., A.L. Sukstanskii, and D.A. Yablonskiy, *Phase-sensitive B1 mapping: Effects of relaxation and RF spoiling.* Magn Reson Med, 2018. **80**(1): p. 101-111.

68.   van Gelderen, P. and J.H. Duyn, *White matter intercompartmental water exchange rates determined from detailed modeling of the myelin sheath.* Magn Reson Med, 2018.

69.   Traboulsee, A.L. and D.K. Li, *The role of MRI in the diagnosis of multiple sclerosis.* Adv Neurol, 2006. **98**: p. 125-46.

70.   Sormani, M.P., et al., *MRI metrics as surrogate endpoints for EDSS progression in SPMS patients treated with IFN beta-1b.* Neurology, 2003. **60**(9): p. 1462-6.

71.   Bermel, R.A., et al., *Predictors of long-term outcome in multiple sclerosis patients treated with interferon beta.* Ann Neurol, 2013. **73**(1): p. 95-103.

72.   Naismith, R.T. and A.H. Cross, *Multiple sclerosis and black holes: connecting the pixels.* Arch Neurol, 2005. **62**(11): p. 1666-8.

73.   Harel, A., et al., *Phase-Sensitive Inversion-Recovery MRI Improves Longitudinal Cortical Lesion Detection in Progressive MS.* PLoS One, 2016. **11**(3): p. e0152180.

74.   Fisher, E., et al., *Imaging correlates of axonal swelling in chronic multiple sclerosis brains.* Ann Neurol, 2007. **62**(3): p. 219-28.

75.   Bot, J.C., et al., *Spinal cord abnormalities in recently diagnosed MS patients: added value of spinal MRI examination.* Neurology, 2004. **62**(2): p. 226-33.

76.   Lukas, C., et al., *Relevance of spinal cord abnormalities to clinical disability in multiple sclerosis: MR imaging findings in a large cohort of patients.* Radiology, 2013. **269**(2): p. 542-52.

77.   Derakhshan, M., et al., *Surface-based analysis reveals regions of reduced cortical magnetization transfer ratio in patients with multiple sclerosis: a proposed method for imaging subpial demyelination.* Hum Brain Mapp, 2014. **35**(7): p. 3402-13.

78.   Hulst, H.E., et al., *Cognitive impairment in MS: impact of white matter integrity, gray matter volume, and lesions.* Neurology, 2013. **80**(11): p. 1025-32.

79.   Kolind, S.H. and S.C. Deoni, *Rapid three-dimensional multicomponent relaxation imaging of the cervical spinal cord.* Magnetic Resonance in Medicine, 2010: p. n/a-n/a.

80.   Mainero, C., et al., *A gradient in cortical pathology in multiple sclerosis by in vivo quantitative 7 T imaging.* Brain, 2015. **138**(Pt 4): p. 932-45.

81.   Ge, Y., *Multiple sclerosis: the role of MR imaging.* AJNR Am J Neuroradiol, 2006. **27**(6): p. 1165-76.

82.   Ulrich, X. and D.A. Yablonskiy, *Separation of cellular and BOLD contributions to T2* signal relaxation.* Magn Reson Med, 2016. **75**(2): p. 606-15.

83.   Wen, J., A.H. Cross, and D.A. Yablonskiy, *On the role of physiological fluctuations in quantitative gradient echo MRI: implications for GEPCI, QSM, and SWI.* Magn Reson Med, 2015. **73**(1): p. 195-203.

84.   Bot, J.C., et al., *The spinal cord in multiple sclerosis: relationship of high-spatial-resolution quantitative MR imaging findings to histopathologic results.* Radiology, 2004. **233**(2): p. 531-40.

85.   Seewann, A., et al., *Diffusely abnormal white matter in chronic multiple sclerosis: imaging and histopathologic analysis.* Arch Neurol, 2009. **66**(5): p. 601-9.

86.   Patel, K.R., et al., *Detection of cortical lesions in multiple sclerosis: A new imaging approach.* Mult Scler J Exp Transl Clin, 2015. **1**: p. 2055217315606465.

87.   Mugler, J.P., 3rd and J.R. Brookeman, *Three-dimensional magnetization-prepared rapid gradient-echo imaging (3D MP RAGE).* Magn Reson Med, 1990. **15**(1): p. 152-7.

88.   Yablonskiy, D.A., *Quantitation of intrinsic magnetic susceptibility-related effects in a tissue matrix. Phantom study.* Magn Reson Med, 1998. **39**(3): p. 417-28.

89.   De Leener, B., et al., *SCT: Spinal Cord Toolbox, an open-source software for processing spinal cord MRI data.* Neuroimage, 2017. **145**(Pt A): p. 24-43.

90.   Shiee, N., et al., *A topology-preserving approach to the segmentation of brain images with multiple sclerosis lesions.* Neuroimage, 2010. **49**(2): p. 1524-35.

91.   McAuliffe, M.J., et al. *Medical Image Processing, Analysis and Visualization in clinical research*. in *Computer-Based Medical Systems, 2001. CBMS 2001. Proceedings. 14th IEEE Symposium on*. 2001.

92.   Sati, P., et al., *In vivo quantitative evaluation of brain tissue damage in multiple sclerosis using gradient echo plural contrast imaging technique.* Neuroimage, 2010. **51**(3): p. 1089-97.

93.   Zhao, Y., et al., *In vivo detection of microstructural correlates of brain pathology in preclinical and early Alzheimer Disease with magnetic resonance imaging.* Neuroimage, 2017. **148**: p. 296-304.

94.   Wen, J., et al., *Detection and quantification of regional cortical gray matter damage in multiple sclerosis utilizing gradient echo MRI.* Neuroimage Clin, 2015. **9**: p. 164-75.

95.   Steenwijk, M.D., et al., *Cortical atrophy patterns in multiple sclerosis are non-random and clinically relevant.* Brain, 2016. **139**(Pt 1): p. 115-26.

96.   Bo, L., et al., *Subpial demyelination in the cerebral cortex of multiple sclerosis patients.* J Neuropathol Exp Neurol, 2003. **62**(7): p. 723-32.

97.   Guo, Y. and C. F. Lucchinetti, *Taking a Microscopic Look at Multiple Sclerosis*. 2016. 65-88.

98.   Oh, J., et al., *Relationships between quantitative spinal cord MRI and retinal layers in multiple sclerosis.* Neurology, 2015. **84**(7): p. 720-728.

99.   Ruggieri, S., et al., *Association of Deep Gray Matter Damage With Cortical and Spinal Cord Degeneration in Primary Progressive Multiple Sclerosis.* JAMA Neurol, 2015. **72**(12): p. 1466-74.

100.   Losseff, N.A., et al., *Spinal cord atrophy and disability in multiple sclerosis. A new reproducible and sensitive MRI method with potential to monitor disease progression.* Brain, 1996. **119 (Pt 3)**: p. 701-8.

101.   Laule, C., et al., *Magnetic resonance imaging of myelin.* Neurotherapeutics, 2007. **4**(3): p. 460-84.

102.   Griswold, M.A., et al., *Generalized autocalibrating partially parallel acquisitions (GRAPPA).* Magn Reson Med, 2002. **47**(6): p. 1202-10.

103.   Kaufman, M., D. Moyer, and J. Norton, *The significant change for the Timed 25-foot Walk in the multiple sclerosis functional composite.* Mult Scler, 2000. **6**(4): p. 286-90.

104.   Oxford Grice, K., et al., *Adult norms for a commercially available Nine Hole Peg Test for finger dexterity.* Am J Occup Ther, 2003. **57**(5): p. 570-3.

105.   Strober, L., et al., *Sensitivity of conventional memory tests in multiple sclerosis: comparing the Rao Brief Repeatable Neuropsychological Battery and the Minimal Assessment of Cognitive Function in MS.* Mult Scler, 2009. **15**(9): p. 1077-84.

106.   Levesque, I.R., et al., *Quantitative magnetization transfer and myelin water imaging of the evolution of acute multiple sclerosis lesions.* Magn Reson Med, 2010. **63**(3): p. 633-40.

107.   Simon, J.H., L. Jacobs, and N. Simonian, *T1-Hypointense Lesions (T1 Black Holes) in Mild-to-Moderate Disability Relapsing Multiple Sclerosis*, in *Early Indicators Early Treatments Neuroprotection in Multiple Sclerosis*, O.R. Hommes and G. Comi, Editors. 2004, Springer Milan: Milano. p. 135-139.

108.   Vrenken, H., et al., *Whole-brain T1 mapping in multiple sclerosis: global changes of normal-appearing gray and white matter.* Radiology, 2006. **240**(3): p. 811-20.

109.   West, K.L., et al., *Myelin volume fraction imaging with MRI.* Neuroimage, 2016.

110.   Dutta, R. and B.D. Trapp, *Relapsing and progressive forms of multiple sclerosis: insights from pathology.* Curr Opin Neurol, 2014. **27**(3): p. 271-8.

111.   Oh, J., et al., *Imaging outcome measures of neuroprotection and repair in MS.* A consensus statement from NAIMS, 2019. **92**(11): p. 519-533.

112.   Kutzelnigg, A., et al., *Cortical demyelination and diffuse white matter injury in multiple sclerosis.* Brain, 2005. **128**(Pt 11): p. 2705-12.

113.   Sati, P., et al., *The central vein sign and its clinical evaluation for the diagnosis of multiple sclerosis: a consensus statement from the North American Imaging in Multiple Sclerosis Cooperative.* Nature Reviews Neurology, 2016. **12**: p. 714.